

MODELING AND REDUCTION OF REVERBERATION NOISE IN  
MEDICAL ULTRASOUND IMAGES

A DISSERTATION SUBMITTED TO  
THE DEPARTMENT OF ENGINEERING CYBERNETICS  
AT THE NORWEGIAN UNIVERSITY OF SCIENCE AND TECHNOLOGY  
IN PARTIAL FULFILLMENT OF THE REQUIREMENTS  
FOR THE DEGREE OF  
DOKTOR INGENIØR

By  
Michael Nickel  
February, 1997



# Abstract

Reverberations, also called multiple echoes, affect in certain cases significantly the quality of medical ultrasound images. The purpose of this thesis was hence to describe this acoustic noise effect and develop noise reduction schemes that enhance the diagnostic value of ultrasound images.

In a first step a rigorous model was derived for first order echoes and transducer reverberations i.e. those echoes hitting the transducer after having traveled from the transducer to a first target, back to the transducer and once more forth to a second target and back to the transducer. The main new development in this model was the description of the transducer reflection factor, which was decomposed into an acoustic and an electric contribution. The acoustic contribution follows the same physical laws as a reflection from non-piezoelectric materials. The electric component is specific for piezoelectric materials covered by electrodes. When a pulse wave hits the transducer locally, a voltage is generated at that point, which however spreads quasi-simultaneously all over the electrode and thus drives the whole transducer resulting in a reradiation of ultrasound. It was further found that these reflection factor components are accompanied by their specific pulse propagation patterns. A numerical implementation of the model proved to be accurate, deviating less than 1dB in terms of RMS-values from the corresponding experimentally measured RF-pulses. Based on the model several reverberation reduction schemes were suggested and investigated.

In the first proposed reduction scheme, a cardiac ultrasound image sequence was filtered from frame to frame through a highpass filter. With this, stationary reverberations overlaying on the apex region of the heart were reduced significantly. The processing had to be done directly on the RF-data or their equivalent analytical signal representation. Working on amplitude data or even grey-scale-compressed data proved to be insufficient. Because of cost-effectiveness a low filter order was mandatory. A fourth order FIR filter performed

best amongst the investigated LSI-filters.

The second reduction approach exploited the difference between reverberations and first order echoes in the propagation path. Displacing the transducer a distance of approximately a quarter wavelength along its axis without deforming the scatterer distribution led to a shift of  $\Delta T = \lambda/2c$  for the first order echoes and  $\Delta T = \lambda/c$  for transducer reverberations. Aligning two such signals thus their reverberation components match and consecutive subtraction led to a  $\approx 11$ dB reduction of the reverberation signal.

The third reduction algorithm played on the fact that the electrical component of the transducer reverberations was dependent on the electric receive impedance. Recording two images with different receive impedances enabled to extract the electric reverberation component. The acoustic component was gained through a mapping from the electric component. Simulations indicated that a reverberation noise reduction of  $\approx 10$ dB was possible for 1D phased arrays whereas 1.5D array yield about 15dB.

The fourth approach of reducing transducer reverberations was based on signal processing of first order signals. It turned out that when recording a defocused beam signal of the target distribution and convolving it with a focused beam signal of the same target distribution, a good estimate of reverberation echoes was attained. With optimal focus settings a noise reduction gain of about 13dB was obtained. With focus settings convenient for an implementation the reduction gain decreased to  $\approx 10$ dB. A problem was however that the delay of the reverberation estimates had to be slightly amended in dependence on the target range in order to yield these reduction gains. It was not possible to find out if this delay problem was due to numerical inaccuracies or a real acoustic phenomenon. Thus, an experimental verification should be performed before this scheme is developed further.

Conclusively, algorithms were devised having the potential to reduce reverberations by 6dB–11dB. Advanced processing of the received RF-signals or their analytical representation was necessary, in addition to adapting transducer probes and frontend hardware. This might not be cost-efficient today but in order to bring ultrasound image quality further, complex processing schemes seem mandatory.

*Betre byrði*

*du ber kje i bakken  
enn mannevit mykje.*

*D'er betre enn gull  
i framand gard;  
vit er vesalmanns trøyst.*

(from the Håvamål)



# Acknowledgments

First of all I would like to thank my advisor, Professor Bjørn A. J. Angelsen, for introducing me to the intriguing subject of ultrasound imaging, for his support, numerous useful suggestions and enthusiastic discussions. His never failing optimism and encouragement has helped me through the difficult periods of my work.

Further, I appreciate the fruitful discussions with Åge Grønningsæter and thank him for the collaboration on the topic of Chapter 4.

I am also indebted to Torgrim Lie for his help with trouble-shooting the experiment system.

Furthermore, I want to thank the rest of staff at the Department of Physiology and Biomedical Engineering for helpful suggestions and interesting discussions on ultrasound and other topics.

Nancy Eik-Nes is thanked for her comments concerning the English language in this thesis.

This thesis was financially supported by a scholarship of the Norwegian University of Science and Technology and initially by a scholarship from Deminex. This is greatly appreciated.

On the personal side I want to thank all my friends for sharing their time with me and making the past years so eventful and pleasant.

Last but not least I would like to give a special thank to my parents. They have taught me very early the importance of questioning and studying, and have encouraged me to learn foreign languages and meet people abroad. I want to thank them for their support and making my graduate studies possible, without which this thesis would not have come forth.



# Contents

<b>Abstract</b>	<b>iii</b>
<b>Acknowledgments</b>	<b>vii</b>
<b>Symbols and abbreviations</b>	<b>xiii</b>
<b>1 Introduction</b>	<b>1</b>
1.1 Medical imaging with ultrasound . . . . .	1
1.2 Why ultrasound? . . . . .	2
1.3 Image quality limits . . . . .	2
1.4 Motivation for our work . . . . .	3
1.5 Significance of reverberations . . . . .	4
1.6 Outline of the thesis . . . . .	6
<b>2 Basic concepts in ultrasound imaging</b>	<b>9</b>
2.1 Common system architecture . . . . .	9
2.1.1 Transducer types . . . . .	10
2.1.2 Analog-to-digital converter . . . . .	12
2.1.3 Beam former . . . . .	12
2.1.4 Demodulation, lowpass filter and spectrum shaping filters . . . . .	14
2.1.5 Time gain compensation . . . . .	14
2.1.6 Nonlinear compression . . . . .	15
2.1.7 Scan conversion and digital-to-video conversion . . . . .	15
<b>3 A signal model for ultrasound imaging</b>	<b>17</b>
3.1 Model decomposition . . . . .	18

3.2	Transducer model . . . . .	19
3.2.1	Transducer transfer functions . . . . .	19
3.2.2	Transducer characterization experiment . . . . .	21
3.3	A 3D acoustic model for pulse propagation . . . . .	27
3.3.1	Acoustic pulse propagation in homogeneous material . . . . .	28
3.3.2	Scattering from inhomogeneous material . . . . .	30
3.3.3	Spatial echo impulse response . . . . .	32
3.3.4	Simulation program . . . . .	34
3.3.5	Program validation . . . . .	39
3.4	Reverberations . . . . .	44
3.4.1	A model for the transducer reflection factor . . . . .	45
3.4.2	Verification experiment . . . . .	48
3.4.3	Reverberation beam pattern . . . . .	53
3.4.4	Reverberation simulation program . . . . .	56
3.4.5	Experimental validation . . . . .	57
3.4.6	Testing and remodeling . . . . .	59
3.5	1D signal model . . . . .	62
3.6	Summary and discussion . . . . .	65
<b>4</b>	<b>Reduction of stationary reverberations</b>	<b>67</b>
4.1	Filter design . . . . .	67
4.1.1	Filter specifications . . . . .	69
4.1.2	Error function, norm and side constraints . . . . .	72
4.2	Optimum filter and performance test . . . . .	75
4.3	Left right scan problem . . . . .	78
4.4	Other processing domains . . . . .	79
4.5	Summary and discussion . . . . .	80
<b>5</b>	<b>Reverberation reduction by transducer displacement</b>	<b>83</b>
5.1	Signal model . . . . .	84
5.2	The optimal choice of $\Delta r$ . . . . .	86
5.3	Residual reverberation signal . . . . .	90
5.4	Limits for improvement through up-sampling . . . . .	91
5.4.1	Limit from model accuracy . . . . .	92

5.4.2	Sampling limit from shift variance . . . . .	93
5.5	Filter scheme . . . . .	94
5.6	An alternative to transducer displacement . . . . .	95
5.7	Phantom experiments . . . . .	96
5.8	Summary and discussion . . . . .	101
<b>6</b>	<b>Reverberation reduction by impedance change</b>	<b>105</b>
6.1	The algorithm . . . . .	105
6.2	Determining the acoustic component . . . . .	107
6.2.1	Testing inverse filtering schemes . . . . .	108
6.2.2	Effect of the different beam patterns . . . . .	110
6.3	Simulations for various target distributions . . . . .	113
6.3.1	Plane and curved interfaces . . . . .	114
6.3.2	Tilted interfaces . . . . .	116
6.3.3	Influence of interface roughness . . . . .	123
6.3.4	Element size . . . . .	124
6.3.5	Steering the ultrasound beam at an angle $\Theta$ . . . . .	127
6.4	Summary and remarks . . . . .	127
<b>7</b>	<b>Reverberation reduction by signal processing of first order echoes</b>	<b>129</b>
7.1	Development of the signal processing scheme . . . . .	130
7.1.1	Decomposition of the acoustic component . . . . .	130
7.1.2	Electric reverberation component . . . . .	132
7.1.3	Realization of the defocused beam . . . . .	133
7.2	Evaluation through simulations . . . . .	137
7.2.1	Receive focus at $f_{r,b} = r_1 + r_3$ . . . . .	138
7.2.2	Convenient focus settings for $v_{1^{st}order,b}$ . . . . .	139
7.2.3	Defocusing settings . . . . .	140
7.3	Further steps . . . . .	141
7.4	Conclusion . . . . .	142
<b>8</b>	<b>Conclusions</b>	<b>143</b>
8.1	Contributions of this thesis . . . . .	143
8.2	Suggestions for possible future research . . . . .	144

<b>A Appendix to Chapter 3</b>	<b>146</b>
A.1 Derivation of equation 3.39 from equation 3.36 . . . . .	146
A.2 Further first order off-axis plots . . . . .	149
<b>B Appendix to Chapter 4</b>	<b>152</b>
B.1 FIR filter design . . . . .	152
B.2 IIR filter design . . . . .	153
B.3 Filtering results . . . . .	154
<b>C Appendix to Chapter 6</b>	<b>159</b>
<b>D Appendix to Chapter 7</b>	<b>161</b>
<b>Bibliography</b>	<b>163</b>

# Symbols and abbreviations

RF	-	radio frequency
A/D	-	analog to digital
TGC	-	time gain compensation
LSI	-	linear shift-invariant
LP	-	lowpass
BP	-	bandpass
ROC	-	radius of curvature
re	-	real part
im	-	imaginary part
1D	-	one-dimensional
3D	-	three-dimensional
RMS	-	root mean square
FFT	-	fast Fourier transform
$t$	-	time
$f$	-	frequency
$\Delta f$	-	bandwidth
$b$	-	relative bandwidth, $\Delta f/f$
$\lambda$	-	wavelength
$c$	-	velocity of sound, locally varying
$c_a$	-	average velocity of sound
$\rho$	-	mass density
$\kappa$	-	compressibility

$\vec{r}$	- position vector
$r$	- magnitude of $\vec{r}$ , range
$F$	- focus
$D$	- diameter of the aperture
$v(t)$	- RF-signal, output of the beamformer
$\hat{v}(t)$	- demodulated, analytical signal of $v(t)$
$v_{gr}(t)$	- greyscale compressed signal
$v_g(t)$	- electric excitation signal
$u(t)$	- RF-pulse
$u_e(t)$	- complex envelope of $u(t)$
$I$	- intensity
$u_v(t)$	- transducer surface vibration velocity
$\vec{v}(\vec{r}, t)$	- particle velocity
$p(t)$	- pressure
$P(t)$	- pressure force (not the Fourier transform of $p(t)$ )
$i_{sc}(t)$	- short-cut current
$Z_L$	- characteristic acoustic impedance of the load medium
$Z_{tr}$	- effective acoustic transducer impedance
$Z_i$	- electric inner transducer impedance
$Z_r$	- electric receive impedance
$h_{tt}(t)$	- transducer transmit transfer function
$h_{rt}(t)$	- transducer receive transfer function
$h_i(t)$	- transfer function of the receive impedance
$h_t(\vec{r}, t)$	- transmit beam profile
$h_r(\vec{r}, t)$	- receive beam profile
$h_{rev}(\vec{r}_1, \vec{r}_3, t)$	- reverberation kernel
$\tau(\vec{r}_0)$	- time delay function in dependence on the aperture point
$a(\vec{r}_0)$	- apodisation function
$r(t)$	- reflection factor
$r_{ac}(t), r_{el}(t)$	- its acoustic and electric component
$N$	- number of array elements
$N_S$	- number of simulation elements

$\mathcal{A}$	-	transducer surface
$\mathcal{A}_n$	-	array element surface
$\mathcal{A}_i$	-	simulation element surface
$\theta_{a/e}$	-	azimuth/elevation angle of a simulation element
$\vec{n}_A$	-	normal vector on the transducer surface
$\vec{e}_{10}$	-	unity vector for the direction from point 0 to point 1
$\vec{e}_x, \vec{e}_y, \vec{e}_z$	-	unity vectors of the Cartesian coordinate system
$\delta(t)$	-	Dirac pulse, discrete or continuous
$rect(t)$	-	rectangular function: $\begin{cases} 1 & \text{if }  t  < 0.5 \\ 0 & \text{otherwise} \end{cases}$
$si(t)$	-	$\frac{\sin(t)}{t}$
$g(t)$	-	Green's function
$\mathcal{F}\{.\}$	-	Fourier transform
*	-	temporal convolution



# Chapter 1

## Introduction

Ultrasound refers to sound waves in the non-audible range from 20kHz to as high as some 100GHz. Sending out short pulse bursts into biological tissue and recording the reflected echoes can be used to generate an image of the acoustic properties of the tissue and with this gain information about the tissue type and its morphological distribution.

### 1.1 Medical imaging with ultrasound

The growth of the use of ultrasound imaging in medicine has been nearly exponential in the last two decades. Areas of application are many and are still increasing.

Most known is perhaps abdominal imaging in obstetrics. Other traditional applications are diagnostic cardiac imaging to detect possible malfunctions or abnormalities in the anatomy of the heart[1], monitoring the recovering heart after infarction surgery or heart transplantation [2], measuring physiological parameters such as flow or blood velocity[3][4][5]; or imaging peripheral arteries to find possible stenoses, plaques, calcifications . . . . Another still emerging area is tissue characterization[6][7][8][9] to detect tumors in such organs as the liver, kidneys, brain, or in the breast, ovaries, cervix, prostate. An important future methodology will be to use ultrasound imaging to guide the surgeon under an ongoing laparoscopic operation [10], offering a view into tissue before cutting it. This will be an improvement over the present situation where the surgeon is restricted to looking only at tissue surfaces with the optical camera.

Furthermore, in the future three dimensional (3D) ultrasound[11] may ease the diagnosis for less experienced/trained sonographers or physicians, giving them a full spatial overview

of the scanned object.

## 1.2 Why ultrasound?

The reason for the wide spread use of ultrasound imaging in spite of the presence of other high quality medical imaging facilities e.g. magnetic resonance (MR), X-ray, positron emission tomography (PET) are its numerous advantages. The most important are: the non-ionizing nature of ultrasound, the possibility of real-time imaging, the mobility of the scanner system, and its comparatively low price. As with the imaging methodologies mentioned, apart from PET, the possibility to get information about parameters inside the body non-invasively means less stress to the patient; this is a major advantage.

However, in the case of ultrasound, there are also applications for low-invasive use. In intra-vascular ultrasound (IVUS) a catheter with a tiny ultrasound probe on its tip is inserted into the (human) vascular system providing the physician with high resolution images of the blood vessel walls and enabling him to inspect these for the occurrence of plaque, stenosis and control for example the installation of a stent[12].

## 1.3 Image quality limits

From the examples above, the reader may imagine the huge variety of ultrasound imaging applications. For all of them, it is of utmost importance to provide the physicians with high quality images. This applies especially in the case of the emerging field of 3D ultrasound imaging. Here reliable ultrasound images are crucial for further processing like regularisation, edge detection, image segmentation and stereo matching.

Indeed, the image quality of ultrasound imaging can still be greatly improved. There are several artifacts or noise sources that deteriorate ultrasound signals. Besides the electronic noise generated by the electronic devices in the ultrasound probe and scanner or induced by radiation, we observe a variety of acoustic noise types. The most significant of these are[13]:

- speckle
- multiple echoes or reverberations
- phase front aberrations

Speckle refers to the oscillating pattern which is observed in the image when the echo of two (or more) nearby targets superimpose. Reverberations can be defined as those echoes hitting the transducer that were reflected by more than one target. Phase front aberrations are due to pulse multi-path propagation where the pulses travel at different velocities for different paths.

An important feature of acoustic noise is that we cannot reduce its influence just by increasing the power of the emitted pulse. This would help in the case of electronic noise, as long as a certain emission power limit is not exceeded – for reasons of patient safety. Consequently, we have to find appropriate ways to reduce acoustic noise through transducer and system design and/or by processing the data before display.

In addition to electronic and acoustic noise, ultrasound image quality depends on the resolution. Radial resolution is given by the length of the sent pulse, which is inverse proportional to the bandwidth of the transducer. Lateral resolution is given by the beam width which again depends on the transducer aperture and the ultrasound frequency. For a circular transducer, it can be approximated by

$$\Delta r \approx \lambda \frac{F}{D} \quad (1.1)$$

where  $\lambda$  is the wavelength,  $D$  the diameter of the aperture, and  $F$  the distance to the object.

Due to the finite aperture, side-lobes will occur in the beam pattern. They will pick up some echoes from targets not lying on the main beam direction. These side-lobe signals are commonly regarded as noise, too.

## 1.4 Motivation for our work

The above mentioned noise problems have all been recognized for a long time and a lot of work has been dedicated toward solving these problems. Several speckle reduction algorithms have been suggested[14][15][16]. Phase aberrations have been studied thoroughly in the past few years (see [17] for a comprehensive literature review). However, it has not yet been possible to implement the proposed correction algorithms cost-effectively within today's scanner systems.

Reverberations, on the other hand, have not been in the focus of research at all. It is accepted as common knowledge that reducing the reflection factor of the transducer through quarter wavelength matching and electric impedance matching will lead to less reverberation.

However, we found no thorough treatment of this topic in the literature. Further, we found only one paper[18] published in recent years that dealt with the removal of reverberations in medical ultrasound images based on signal processing. The authors tried to remove reverberations between layered interfaces which could be described as specular scatterers, through split spectrum processing. However, they demonstrated the performance of the algorithm only on a plastic phantom that had perfectly plane, highly reflecting surfaces. It remains to be seen whether they can apply the scheme successfully on in vivo objects.

Hence, this thesis intends to study reverberations in more detail and answer some of the questions risen, as well as to come up with some reduction algorithms that will also work on in vivo data.

But, are our efforts worthwhile? Why should the contributions of our work lead further than others before? The answer is simple: Because technique has advanced. Analog to digital (A/D) converters operating at high sampling rates (10MHz – 100MHz) and with a sufficiently high dynamic range have become available. Hence, we can now get direct access to the received radio frequency (RF) signal instead of the amplitude detected data. Besides the additional phase information, it is the linearity of the received ultrasound signal that gives the potential for increased image quality. Having, in addition, time/shift-invariance<sup>1</sup>, linearity means that the relation between the object function, i.e. the scatterer distribution, and the received RF-signal can be described by a convolution. Thus the well-developed theory for LSI-systems applies. Linearity allows further the direct subtraction of the noise signals, presuming we have a good estimate for them.

## 1.5 Significance of reverberations

The justification for our work stands and falls with the assumption that reverberations, if not the main acoustic noise contribution, are at least a significant one. In[17], the author compares the strength of aberrations and reverberations in the ultrasound images of a bacon phantom. He concludes that either can be the dominant noise contribution.

We demonstrate the significance of reverberations showing an in vivo RF-M-mode of a heart in figure 1.1. It indeed gave much of the motivation to start this work. We see the recorded RF-signal along the ordinate which refers to depth versus its change along with time. Near to the probe (at the top) the ultrasound pulse is reflected by strong but

---

<sup>1</sup>Time invariance applies generally as a good approximation for the received ultrasound signal whereas shift-invariance has limited validity.

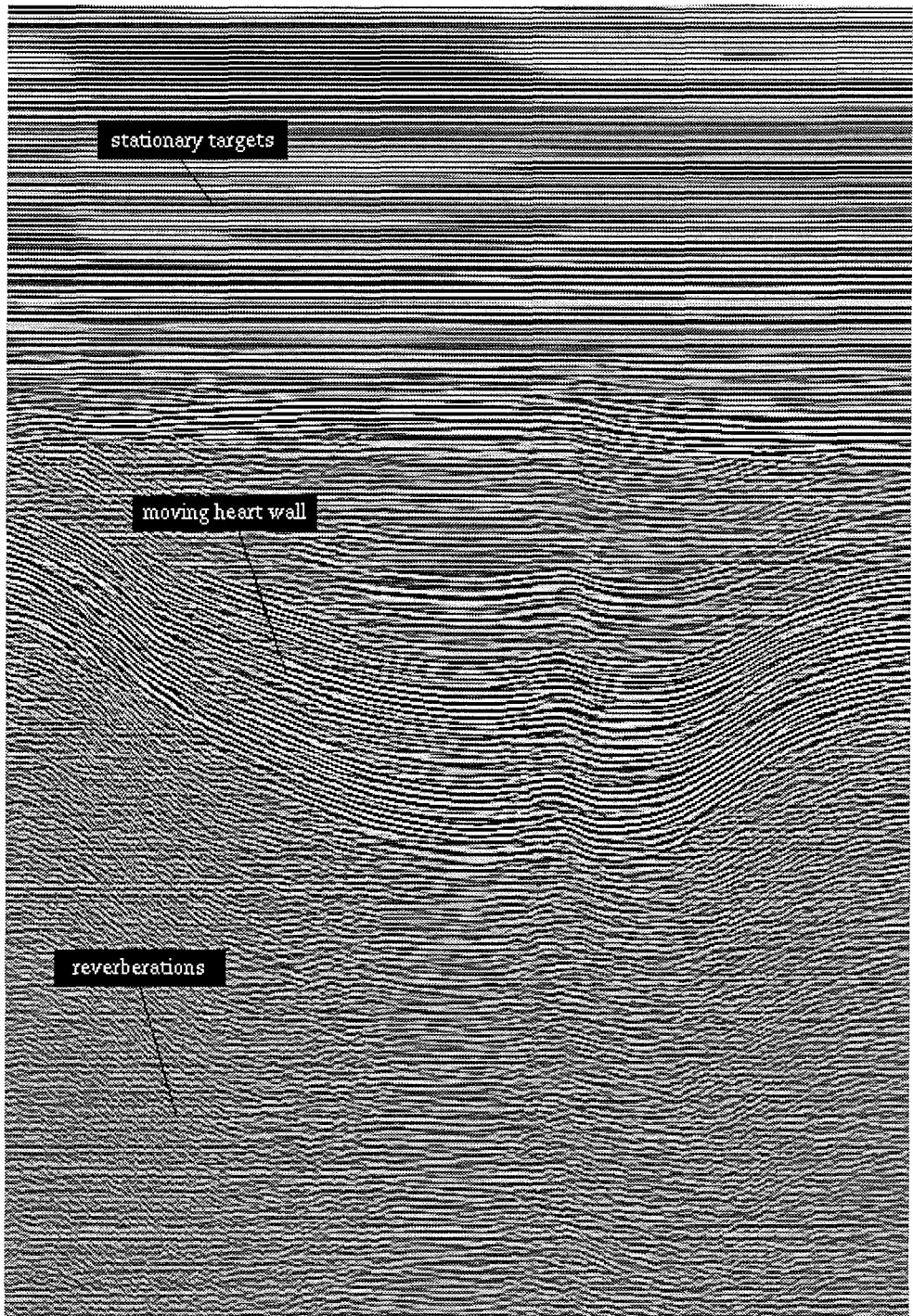


Figure 1.1: RF-data of an M-mode. The ordinate corresponds to the target range and the abscissa to time.

stationary targets and we clearly see the horizontal lines. At deeper ranges we get echoes from the moving heart wall. Because we know that all targets must be in motion at that location, we would not expect any horizontal lines. But inspecting the figure carefully, we see that there are signals from moving parts superimposed on horizontal lines; these signals must be reverberations from stationary near field targets. This M-mode thus supports the findings of others[13][18] that reverberations in some cases constitute a significant acoustic noise source in ultrasound imaging.

Next, we introduce different classes of reverberations, which we will refer to later in the thesis. We differentiate between

- transducer reverberations
- internal reverberations
- reverberations against lungs
- reverberations against ribs
- reverberations against skin

Transducer reverberations are defined as those pulse echoes that after emission hit a first target travel back to the transducer, are reflected at the transducer surface and propagate again into the examination medium hitting the same or another target before finally being received at the transducer. On the other hand, internal reverberations are those recorded signals that stem from an ultrasound pulse bouncing back and forth (up to several times) between two tissue interfaces before propagating back to the transducer. Finally, reverberations against lungs, ribs, or the skin, etc. incorporate a nearly total reflector as one of a minimum of two targets in the echo path.

## 1.6 Outline of the thesis

The outline of the thesis is as follows: First, we give a short description of a contemporary ultrasound imaging system. Then, we introduce a model which describes both first order and second order (i.e. reverberation) effects of the pulse propagation in an acoustic medium and the transformation of the acoustic pulse into an electric pulse by the transducer. In Chapter 4, we present a first reverberation reduction method that improves cardiac ultrasound imaging. The next three chapters are devoted to the reduction of transducer reverberations.

Three different methods are presented and their potential for an implementation is evaluated. The last chapter summarizes the results of the thesis, draws some conclusions and gives suggestions for further research.



## Chapter 2

# Basic concepts in ultrasound imaging

In this chapter, we present some basic concepts in ultrasound imaging, which we will refer to later in this thesis. Our intent here is to summarize present knowledge and to settle the nomenclature rather than to explain all the details of these concepts. Such an explanation would be beyond the scope of this thesis and we point to [19] for an excellent and comprehensive overview of technical aspects in medical ultrasound.

### 2.1 Common system architecture

First, we present a typical architecture of the tissue imaging part in an ultrasound scanner. A block diagram is shown in figure 2.1. The scanner consists of:

1. a probe housing the transducer
2. an analog to digital converter
3. a beam former
4. a demodulator
5. an LP filter
6. an operator calculating the magnitude of a complex signal
7. a linear spectra shaping filter

8. a time/depth gain compensation (TGC/DGC) unit
9. a nonlinear amplifier
10. a scan converter
11. a video signal converter

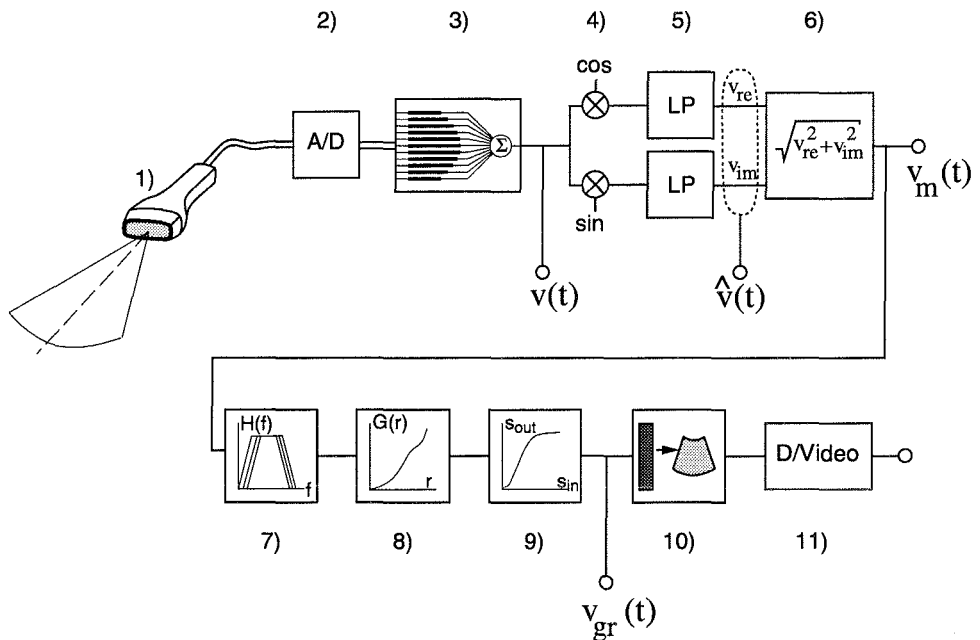


Figure 2.1: Block scheme of the tissue imaging part of an ultrasound scanner.

Whereas we will normally find all the listed components in a digital ultrasound scanner<sup>1</sup>, the order and technical design of the components differ for scanners of different generations or from different manufacturers.

### 2.1.1 Transducer types

Different transducer designs are common. Still most prevalent is an annular array with typically four or five elements which are mechanically focused to a certain radius of curvature

<sup>1</sup>An analog scanner would not have an analog-to-digital converter

(ROC). Adjusting the delay on the elements allows the movement of this focus along the transducer axis. In order to acquire a 2D image (B-mode), the ultrasound beam is scanned over a sector by rotating the transducer back and forth over a given angle (see figure 2.2).

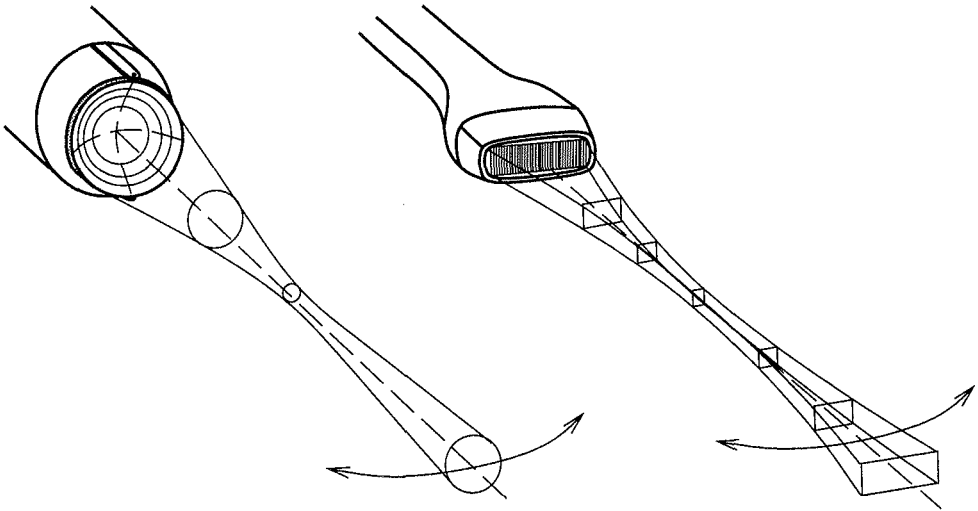


Figure 2.2: Scheme of an annular mechanically scanned transducer (left) and a phased array transducer (right).

In recent years, the use of phased array transducers has become more and more widespread. A transducer array consists of a plurality of elements (typically 128–256) in the azimuth direction and a single element in the elevation direction. Element sizes in the azimuth direction are approximately  $\lambda/2$ , generating a nearly uniform radiation diagram around the element axis in the azimuth plane. With this, it is possible to steer and focus the ultrasound beam in the azimuth direction by adjusting the delay of the individual elements. In the elevation direction, the array is focused either by shaping the elements or by setting an acoustic lens onto the array. Advantages of phased arrays are the very flexible focusing and steering possibilities and the absence of mechanical effects due to scanning, e.g. vibrations, positioning inaccuracy, wear and tear of cables. As a drawback in comparison to annular arrays one might mention the high number of necessary connections and coax-cables and the nonuniform imaging properties in the lateral directions.

It would be desirable to be able to steer and focus the ultrasound beam equally flexibly also in the elevation direction. However, this demands a high number of small elements also in the elevation direction, resulting in an enormous number of output channels of the array. This exceeds at the moment the technical capabilities. However, research groups are working on these problems, and with sparse array techniques [20] and higher integration, such two-dimensional (2D) array transducers will be available some time in the future.

A simplification of the 2D array transducer which may be available in the near future, is the so called 1.5D array. It has a few (3–7) elements in the elevation direction where pairs of elements lying symmetrically around the azimuth plane are connected with each other in order to reduce the number of necessary channels. This enables focusing, but not steering, in elevation direction.

### 2.1.2 Analog-to-digital converter

Analog to digital (A/D) converters in today's common systems operate at sampling frequencies of 10MHz–100MHz. The amplitude of the signals is discretized by 10–16bit.

### 2.1.3 Beam former

The beam former combines the signals of the transducer elements and generates a single RF-signal, which is denoted as  $v(t)$  throughout this thesis. In order to get the RF-signal, the individual element signals are delayed (both during sending and receiving) before they are summed, thus focusing and steering the ultrasound beam. Additionally, the element signals can be weighted differently. This is referred to as the apodization of the transducer.

When sending an RF-pulse from the transducer array, only one set of delays (and one apodization function) can be applied, thus a fixed focus and direction is chosen. On reception, however, one has more flexibility. It is possible to amend the delays in real-time in order to set the focus to that point where the pulse reflection is supposed to occur. This technique is called *dynamic focusing* and generates a very thin ultrasound beam. In modern systems the delays are changed continuously, whereas in older systems it was common to use focusing zones. In figure 2.3, we illustrate the effect of dynamic focusing, showing the monochrome beam-pattern of an array with 128 elements generated by a 2D simulation and comparing it to a fixed focus beam pattern.

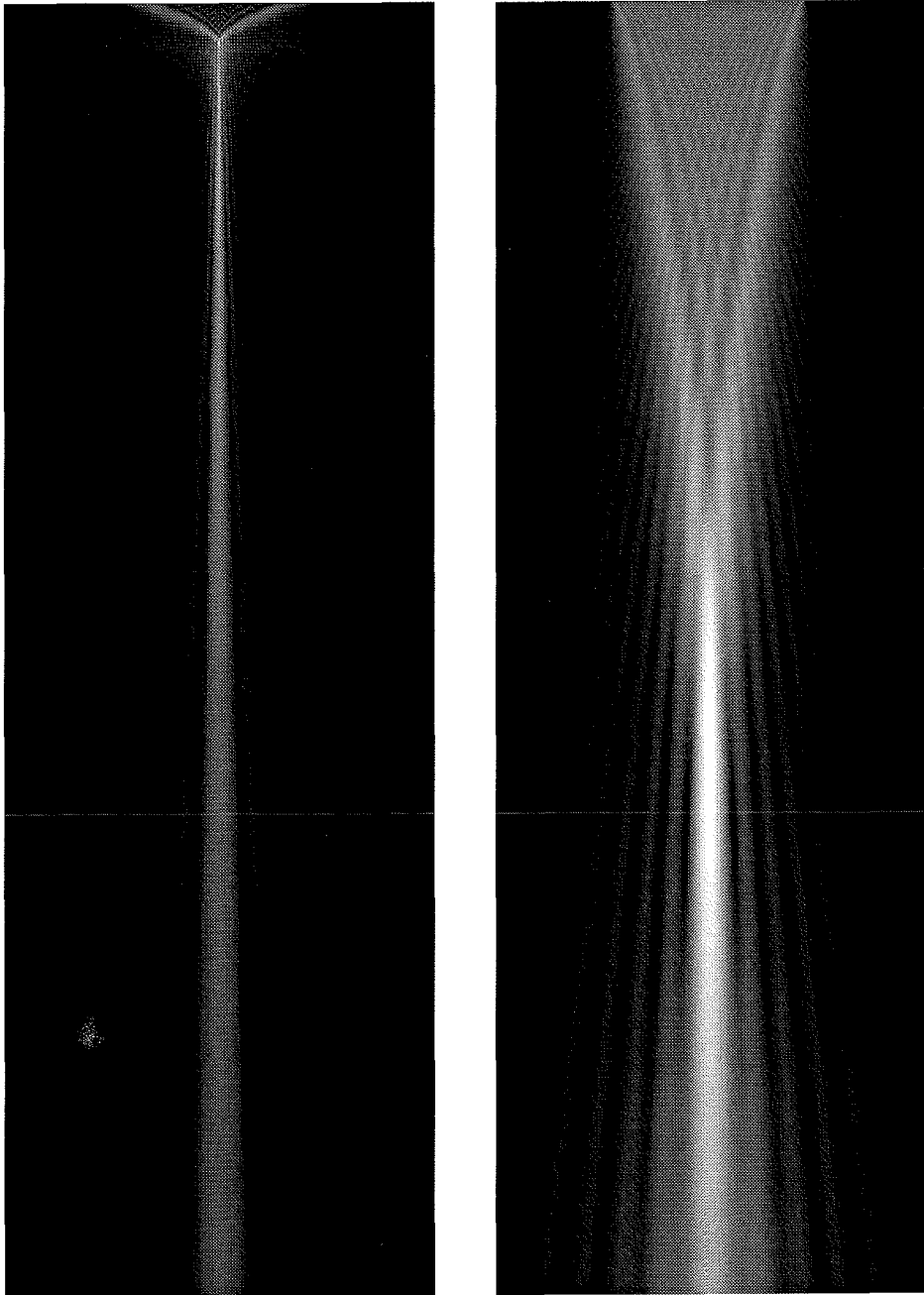


Figure 2.3: 2D simulation of the amplitude of a monochrome beam pattern. A dynamically focused ultrasound beam to the left. A fixed focused (at 80mm) ultrasound beam to the right. The transducer aperture size is 19mm. The beam is displayed up to a range of 120mm.

Another concept applied in the beam former is multiple line acquisition (MLA). Duplicating the beam former components (typically 2–4 times) makes it possible to generate several receive beam signals at the same time, which are steered and/or focused differently. For example, sending out a broad ultrasound beam, it is possible to receive two (or even three or four) neighboring thin ultrasound beams in parallel and cut the frame rate respectively.

#### 2.1.4 Demodulation, lowpass filter and spectrum shaping filters

In order to present smooth images, the received RF-signals are demodulated to the baseband in one of two ways:

1. the received signals are multiplied with a  $\cos(2\pi f_0 t)$  and a  $\sin(2\pi f_0 t)$  oscillation, where  $f_0$  denotes the transducer's center frequency, or
2. an approximative demodulation is done by taking the absolute value of the RF-signals.

After the demodulation, a lowpass filter has to be applied to suppress high frequency mirror signals, which are inherent to the process. The resulting signal is the analytical signal presentation of  $v(t)$  and is denoted by  $\hat{v}(t)$ . However, the phase component of the complex signal is commonly discarded and only the magnitude signal,  $v_m(t)$ , is used for further processing.

An ultrasound pulse is attenuated when it is propagating through biological tissue. This attenuation is frequency-dependent and increases with increasing frequency. Consequently, echoes coming from deeper targets will have a smaller bandwidth. Spectrum shaping filters may be applied on  $\hat{v}(t)$  or  $v_m(t)$  to optimize the signal-to-noise ratio.

#### 2.1.5 Time gain compensation

Deeper targets will have a lower echo signal strength due to attenuation, even though the reflectivity of the target might be the same as the one of a target lying nearer to the transducer. One is, however, interested in representing equal reflectivity with equal brightness on the screen, independent of the location of the target. Therefore, a time or depth gain compensation is applied; this means simply amplifying those signals passing regions with higher attenuation correspondingly more.

### 2.1.6 Nonlinear compression

Specular targets result in very strong signals compared to echoes from diffuse scatterers. Using a linear amplitude to grey-value mapping would only result in some bright spots from the specular echoes on a black background. Therefore, the amplitude range is compressed by some logarithmic function to get a better fit to the human perceptive range. The plot of the compression function we used on some of the data we acquired in our experiments is shown in figure 2.4. The resulting output signal is called the grey-scale signal  $v_{gr}(t)$ .

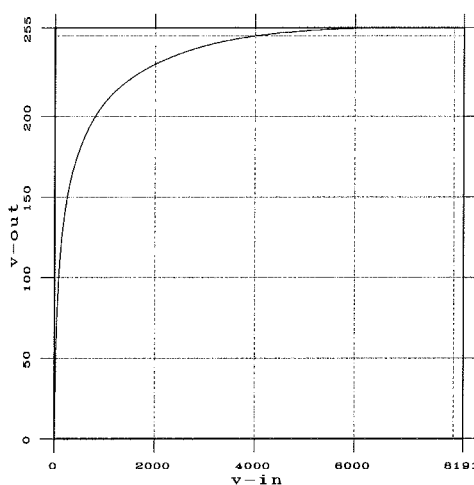


Figure 2.4: Nonlinear function used to compress the amplitude range of the signal  $v_m(t)$ .

### 2.1.7 Scan conversion and digital-to-video conversion

In a last step prior to display, the ultrasound image has to be transformed from polar coordinates into Cartesian coordinates (presuming that we are operating with a sector scan). The result may then be coded into a video signal for display, be stored digitally on some storage medium, or be transmitted over a network.



## Chapter 3

# A signal model for ultrasound imaging

In this chapter, we introduce the model that describes various signals from the pulse excitation at the electrical port of the transducer to the RF-signal that is the output of the beam former. The model will serve as a tool to explain phenomena observed in experiments and it will be used in the development of processing algorithms for reverberation reduction.

Ultrasound imaging can be viewed as a system identification problem. The system is excited by a short electric pulse and the response is recorded in order to gain information about the system. Yet, we have some *a priori* information and can divide the system into sub-blocks or subsystems. The impulse responses of most of these subsystems can be measured in special experiments with special reflecting objects or simulated numerically. It is assumed that these impulse responses stay the same<sup>1</sup> when we image a general object. With some further approximations, it is then possible to reduce the system identification problem to a parameter estimation problem. The parameters are a combination of acoustic properties of the scanned object, namely: the mass density, the velocity of sound and the attenuation. These parameters are commonly highly correlated with the geometric distribution of tissues under examination. It is this anatomic information, we are primarily interested in<sup>2</sup>.

In the following section, we will start with the definition of a first order model that neglects all noise effects, and introduce the mentioned sub-models. In the section 3.2, the

---

<sup>1</sup>This assumption is valid for the electric part of the system. However, there may be some deviations in the acoustic part, which we neglect or describe as additional noise.

<sup>2</sup>However, as indicated in Chapter 1 in tissue characterization quantitative values of these parameters are the main interest.

two-port model of the transducer is described both in sending and reception mode. Then, in section 3.3, the spatial echo impulse response as the main sub-model is derived and a simulation algorithm is given. In section 3.4, we take into account second order effects i.e. expand the first order model to include also transducer reverberations. Having derived the rather complex 3D model, we simplify it to get a 1D representation. Finally, we give a short summary and discussion of the findings of this chapter.

### 3.1 Model decomposition

With the assumption of small signal amplitudes, the first order model can be conveniently described as a linear system. In addition, we have time-invariance for a stationary point target. But, the impulse response will, in general, vary with the location of the point target.

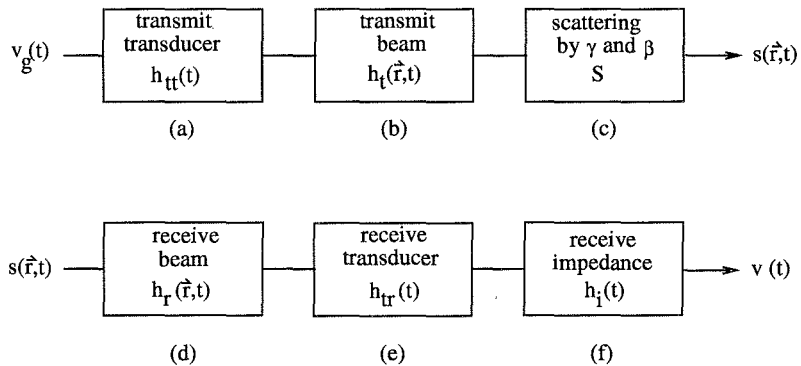


Figure 3.1: First order block model for ultrasound imaging.

The whole model can thus be described by convolution operations and (following the Huygens principle) a final integration over the scatterer distribution. To get an overview of the rather complex system, a block scheme is given in figure 3.1. We can separate the system into two parts:

1. the transducer model, blocks (a), (e) and (f).
2. the model for ultrasound pulse propagation in an acoustic medium, blocks (b)–(d).

Here, block (a) characterizes the electro acoustic transfer function of the transducer crystal,  $h_{tt}(t)$ . This function takes into account the resonance phenomena the piezoelectric crystal

exhibits when driven by an electric pulse. Block (b) represents the spatial/temporal beam pattern of the outgoing pulse, whereas block (c) stands for the scattering operator i.e. the mechanism for the way in which the reflected echoes are formed. The echoes travel back to the transducer and are weighted by the receive beam pattern, block (d). Block (e) represents the transducer transfer function from the pressure at the surface to the source current that is driven through the receive impedance. Finally, block (f) represents the transfer function from the source current to the received voltage.

In the next section, we will look further at the transducer model i.e. blocks (a), (e) and (f), and leave the acoustic propagation model for section 3.3.

## 3.2 Transducer model

In this section, we define the transfer functions describing the transducer characteristics in more detail and thereafter determine these functions for our experiment transducer.

### 3.2.1 Transducer transfer functions

In the frequency domain<sup>3</sup>, the transducer can be described as a two-port system<sup>4</sup> transforming a voltage pulse,  $V_g(f)$ , into a mechanical vibration velocity or “current”,

$$U_v(f) = H_{tt}(f) \cdot V_g(f) \quad , \quad (3.1)$$

which drives the load impedance  $Z_L \cdot A$ , (figure 3.2). Here,  $Z_L$  signifies the characteristic acoustic impedance of the load medium i.e. the biological tissue (or water in experiments), and  $A$  is the area of the plane transducer surface. Correspondingly, an incoming plane pressure wave,  $p_i$ , that hits the transducer surface perpendicularly will generate a pressure force,  $P_i = p_i \cdot A$ , which will be transformed into a current,  $I_{sc}(f) = H_{tr}(f) \cdot \mathcal{F}\{P_i\}$ . This current drives the inner impedance,  $Z_i$ , and the receive impedance,  $Z_r$ , in parallel. It can be directly measured by shorting the electrical port:  $Z_r = 0$ .

Though the transfer function,  $H_{tr}$ , is defined from the incoming pressure force,  $\mathcal{F}\{P_i\}$ , to the current,  $\mathcal{F}\{i_{sc}\}$ , it is actually the total pressure force,  $\mathcal{F}\{P_{tot}\}$ , that activates the

<sup>3</sup>Throughout this thesis, capital letters denote the Fourier transform of the time function, denoted by the respective small letter. Exceptions to this are  $P$  which is the pressure force in the time domain and  $I$  which also denotes the intensity of a signal.

<sup>4</sup>Actually, it is rather a three-port system[21], but the acoustic port towards the backing, onto which the transducer is mounted, is not a port of important signal flow and is therefore not considered here.

piezoelectric effect. The total pressure force,  $\mathcal{F}\{P_{tot}\}$ , is related to the incoming pressure force,  $\mathcal{F}\{P_i\}$ , by the transmission factor:

$$\mathcal{F}\{P_{tot}\} = t \cdot \mathcal{F}\{P_i\} = \frac{2Z_{tr}}{Z_{tr} + Z_L \cdot A} \mathcal{F}\{P_i\} \quad (3.2)$$

Here,  $Z_{tr}$  is the effective acoustic impedance of the transducer. We see that we can describe the incoming pressure force as a “voltage” source of  $\mathcal{F}\{2P_i\}$  that drives the series of the load and transducer impedance (figure 3.2).

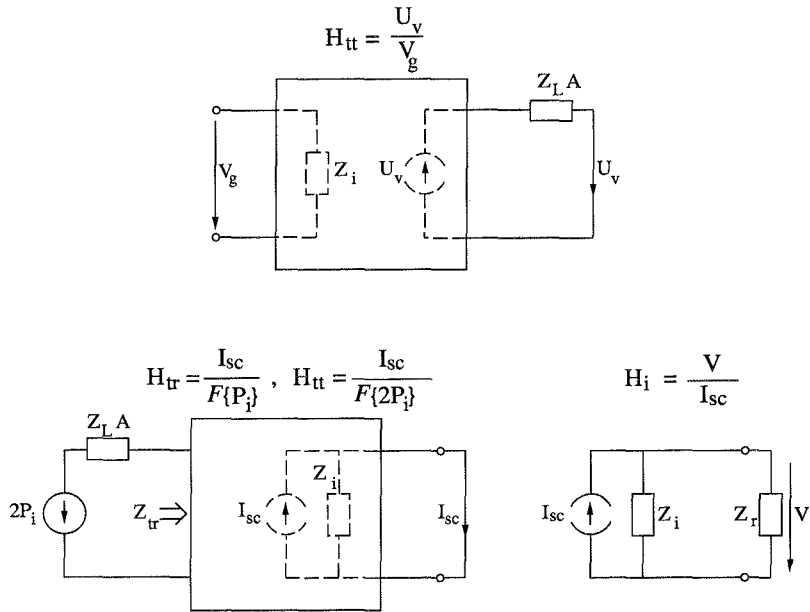


Figure 3.2: Two-port scheme describing the transducer in a one-dimensional model. Situation for sending (top) and for receiving (bottom).

The transducer consists of passive and causal material. Therefore, the reciprocity theorem applies and we find:

$$H_{tt}(f) = \frac{U_v(f)}{V_g(f)} = \frac{1}{2} H_{tr}(f) = \frac{I_{sc}(f)}{2\mathcal{F}\{P_i\}} \quad (3.3)$$

Further, because of time-invariance, we can reorder the transfer functions in the block scheme of figure 3.1 and combine all transducer transfer functions into one function. This function is defined as the insertion loss of a transducer:

$$\begin{aligned} H_{it} &= \frac{V}{\bar{V}_g} \\ &= H_{tt} \cdot H_{tr} \cdot H_i \cdot Z_L \cdot A \\ &= 2 \cdot H_{tt}^2 \cdot H_i \cdot Z_L \cdot A \quad , \end{aligned} \tag{3.4}$$

$$\tag{3.5}$$

and we get the round trip response:

$$\hat{u}(t) = \mathcal{F}^{-1}\{V_g(f) \cdot 2H_{tt}^2(f)H_i(f)\} \cdot Z_L A \quad . \tag{3.6}$$

### 3.2.2 Transducer characterization experiment

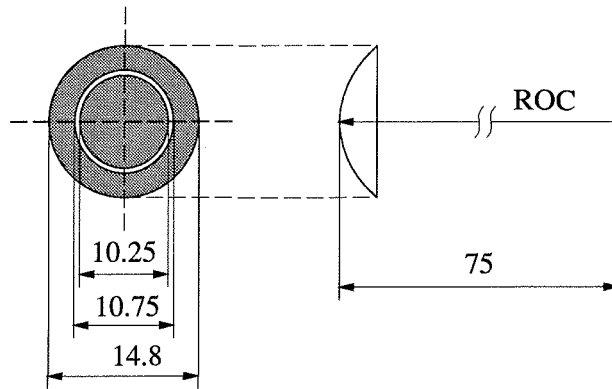


Figure 3.3: Sketch of the transducer used in the characterization experiment. All dimensions are given in mm.

We determined the above defined functions experimentally for a 3MHz, two element annular transducer. This transducer is used in almost all later experiments. The dimensions of the transducer surface are given in figure 3.3. In order to get the plane wave situation, which was presumed in the derivation above, we placed a brass cylinder with a diameter of 20mm at a range of 5mm in front of the transducer (see figure 3.4). The top surface of the cylinder

was turned into the shape of a sphere with a radius of curvature of 70mm. Hence, the center of the transducer surface and the center of the cylinder surface coincide and spherical wave fronts propagating from the transducer are reflected at the brass cylinder without phase distortions. Further, at the range of 5mm, we find extreme near field conditions; thus we can neglect diffraction of the beam. This was confirmed by recording the signal at the outer element of the transducer, while sending with the inner one. The received echo was about 48dB below that received at the inner element. Consequently, with a reflection factor of nearly  $R = 1$  at the water/brass interface, all acoustic energy is reflected back to the transducer surface, thus we can determine the insertion loss of the transducer by measuring the returning first order RF-signal,  $v(t) = \hat{u}(t)$ , and the excitation voltage,  $v_g(t)$ . The plots of these signals are given in figures 3.5–3.7.

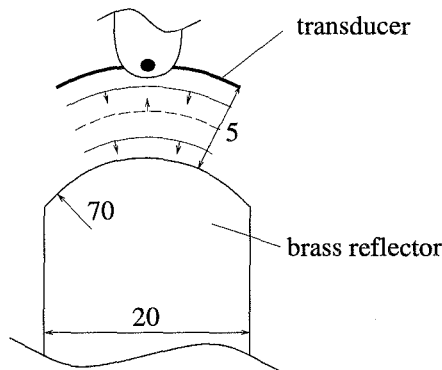


Figure 3.4: Sketch of the transducer sending spherical waves onto the surface of a brass bar. Dimensions are given in mm.

Further, we measured the inner impedance,  $Z_i(f)$ , as well as the function  $H_i(f)$  for each transducer element with a HP4194A impedance/gain phase analyzer (figure 3.8). We observe that the total impedance  $H_i(f)$  of the inner element is slightly higher than that of the outer element which leads to a stronger received pulse from the inner element. From the measurements, we could finally calculate  $H_{tt}$ . Its magnitude is plotted in figure 3.9.

In later experiments, we often used a point scatterer reflecting the ultrasound rather than an extended target. Placing such a point target (e.g. a tiny metal sphere or a needle) into the focus of the transducer, measured the third temporal derivative of round trip response in

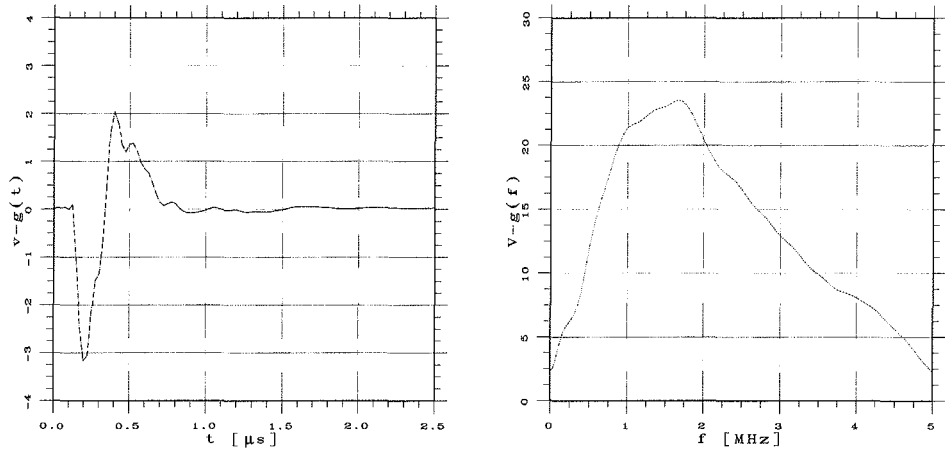


Figure 3.5: Excitation pulse at the electrical port of the transducer (left) and the magnitude of its Fourier spectrum in linear scale (right).

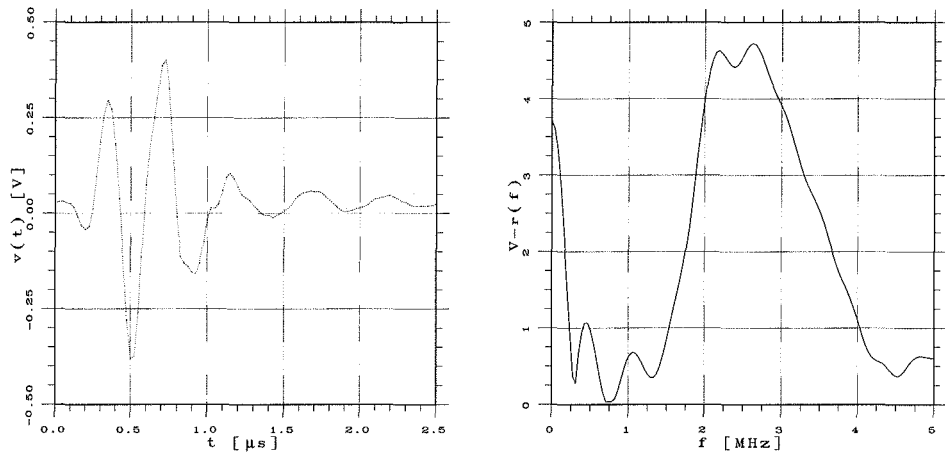


Figure 3.6: Received RF-pulse at the electrical port of the transducer (left) and the magnitude of its Fourier spectrum in linear scale (right).

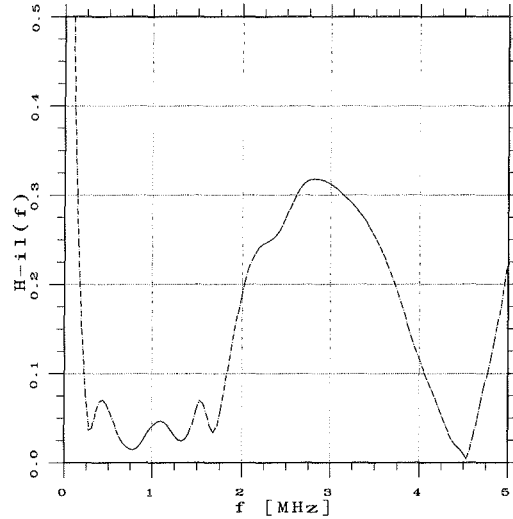


Figure 3.7: Magnitude of the insertion loss function of the transducer. The frequency components below 1MHz and above 4.5MHz are due to clutter signals.

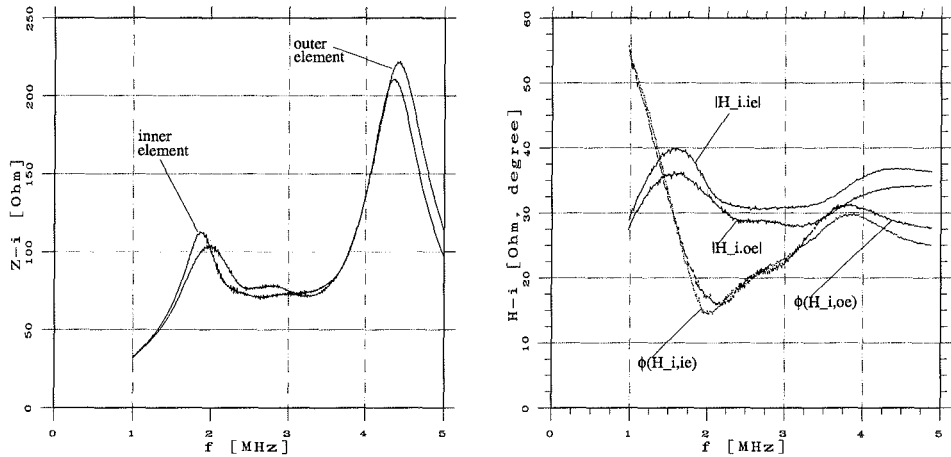


Figure 3.8: Magnitude of the transducer's inner impedance,  $Z_i(f)$ , versus frequency (left), magnitude and phase of the effective receive impedance,  $H_i(f)$ , versus frequency (right).

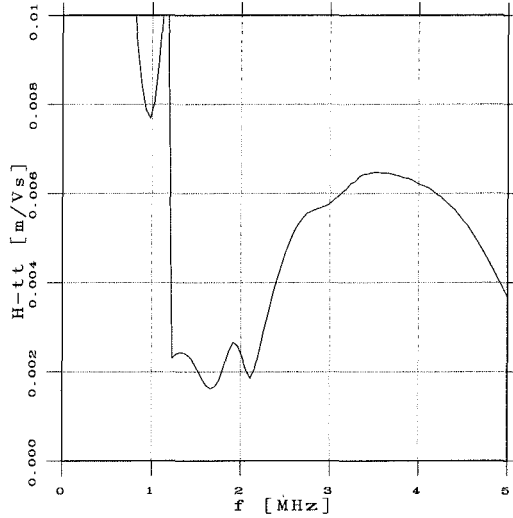


Figure 3.9: Magnitude of the transducer transfer function  $H_{tt}$  in linear scale versus frequency. The signal components below 1.5MHz are due to clutter.

a delayed and attenuated form. The reason the derivative enters in the formula is explained in the next section. Moreover, the transducer is commonly driven with two excitation pulses in series to get a better resonance of the transducer and thus enhance the energy transfer into the medium. Additionally, the received echoes are amplified and bandpass filtered before they are digitized as RF-data. With this, we will measure the following RF-pulse in the focus:

$$u(t) = K \cdot h_{bp}(t) * \delta(t - T_D) * \frac{\partial^3}{\partial t^3} \hat{u}(t) \quad , \quad (3.7)$$

where  $K$  is a proportionality factor,  $h_{bp}(t)$  the impulse response of the bandpass filter, and  $T_D = \frac{2F}{c}$  the time delay of the received pulse.

The RF-pulse,  $u(t)$  of the 3MHz transducer, its frequency spectrum and the magnitude of its analytical signal representation, i.e. its envelope, are shown in figures 3.10, 3.11 and 3.12. From this we see that we can model:

$$u(t) = \Re\{u_e(t) \cdot e^{j2\pi f_0 t}\} \quad (3.8)$$

where  $u_e(t)$  is the complex envelope and  $f_0$  is the nominal center frequency of the transducer.

With this we have studied all functions characterizing the transducer in the first order

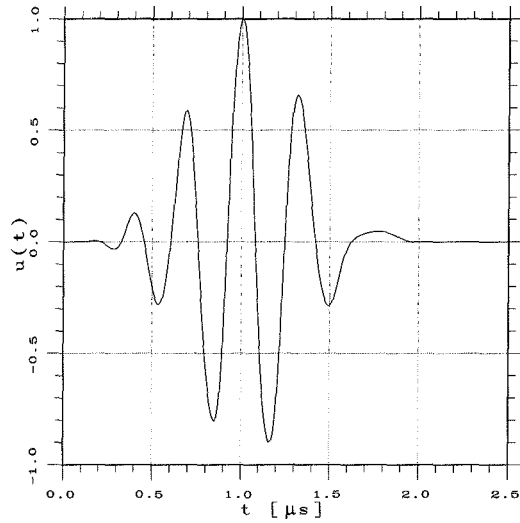


Figure 3.10: Typical ultrasound RF-pulse in linear scale. The nominal transducer center frequency is  $f_0 = 3.0\text{MHz}$ .

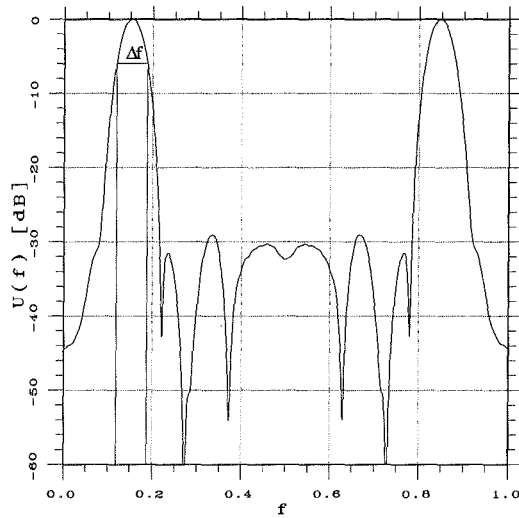


Figure 3.11: Magnitude of the Fourier spectrum in logarithmic scale over normalized frequency. The sampling frequency is  $20\text{MHz}$ . The relative  $-6\text{dB}$ -bandwidth is found to be  $b = \frac{\Delta f}{f_0} = 0.44$

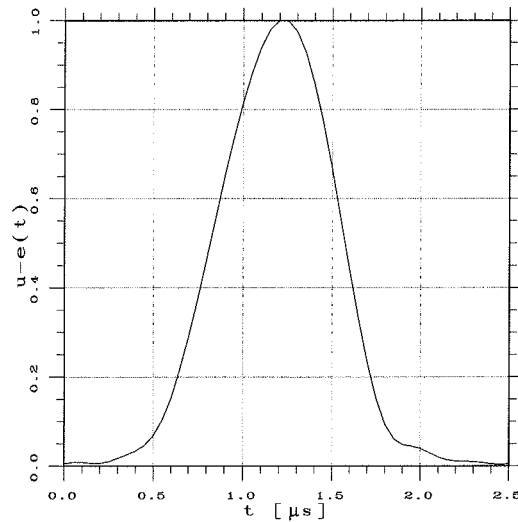


Figure 3.12: Envelope of the RF-pulse in linear scale.

model and can continue with investigating the acoustic pulse propagation.

### 3.3 A 3D acoustic model for pulse propagation

In this section, an acoustic model for pulse wave propagation will be described. Acoustic waves are a subclass of elastic waves neglecting shear waves. This is a valid approximation for biological tissue, because shear waves are heavily attenuated, see Table 3.1 (the data are taken from [22]).

Tissue type	Attenuation in dB/cm
cardiac muscle	-75.56
striated muscle	-73.98
liver	-80.00

Table 3.1: Shear wave attenuation of some tissue material.

### 3.3.1 Acoustic pulse propagation in homogeneous material

Acoustic pulse propagation in a passive, causal and homogeneous medium is governed by conservation laws i.e. mass and momentum<sup>5</sup> (and energy) are conserved:

$$\frac{\partial}{\partial t} \rho_{inst} + \nabla(\rho_{inst} \vec{v}_{inst}) = 0 \quad (3.9)$$

$$\rho_{inst} \frac{\partial}{\partial t} (\vec{v}_{inst}) + \rho_{inst} \vec{v}_{inst} \nabla \vec{v}_{inst} + \nabla p_{inst} = 0 \quad (3.10)$$

where  $\rho_{inst}$  is the instantaneous mass density,  $\vec{v}_{inst}$  the instantaneous particle velocity, and  $p_{inst}$  the instantaneous pressure<sup>6</sup>. In literature, a further equation relating pressure,  $p_{inst}$ , and mass density,  $\rho_{inst}$ , is sometimes derived from entropy considerations in gas dynamics[23]. However, we are dealing with biological tissues and not a gas. We think that it therefore makes more sense to set up a phenomenological equation for linear material:

$$dp = \frac{1}{\kappa} \frac{d\rho}{\rho} \quad (3.11)$$

with  $\kappa$  the compressibility of the material.

To get a treat-able equation, further approximations are made. All instantaneous quantities are Taylor expanded and higher than linear order terms are neglected:

$$\rho_{inst} = \rho_0 + \rho_1(\vec{r}, t) \quad , \quad \vec{v}_{inst} = \vec{v}_0 + \vec{v}_1(\vec{r}, t) \quad , \quad p_{inst} = p_0 + p_1(\vec{r}, t) \quad . \quad (3.12)$$

The quantities  $v_0$ ,  $\rho_0$ , and  $p_0$  are the constant equilibrium values for the undisturbed medium. Especially, we have  $\vec{v}_0 = 0$ . Inserting 3.12 in equations 3.9–3.11 and arranging equal order terms, we get the linear acoustic equations in a Euler coordinate description:

$$\frac{\partial}{\partial t} \rho_1 + \rho_0 \nabla \vec{v}_1 = 0 \quad (3.13)$$

$$\rho_0 \frac{\partial}{\partial t} \vec{v}_1 + \nabla p_1 = 0 \quad (3.14)$$

$$p_1 = \frac{1}{\kappa} \frac{\rho_1}{\rho_0} \quad (3.15)$$

where equation 3.15 results from a Taylor expansion of  $p$  on  $\rho$  in equation 3.11. Combination of equations 3.13–3.15 leads to a linear hyperbolic wave equation for homogeneous material:

$$\nabla^2 p(\vec{r}, t) - \frac{1}{c^2} \frac{\partial^2 p(\vec{r}, t)}{\partial t^2} = 0 \quad (3.16)$$

<sup>5</sup>For momentum conservation a non-viscous medium is assumed[23].

<sup>6</sup>Pressure variation with altitude is negligible for our case.

where the velocity of sound is defined as:

$$c = \frac{1}{\sqrt{\rho_0 k}} \quad (3.17)$$

and we have dropped the index 1 in the notation of the pressure. Applying the Sommerfeld radiation condition[23], the solution of this wave equation in free space is given by Green's function, which can be calculated (see e.g. [19]) as:

$$g(t) = \frac{\delta(t - \frac{r}{c})}{4\pi r} \quad (3.18)$$

From equations 3.16 and 3.18 the Kirchoff-Helmholtz formula can be derived [19] [23], reading:

$$p(\vec{r}, t) = \frac{\rho}{4\pi} \int \frac{\dot{v}_n(\vec{r}_s, t - \frac{|\vec{r} - \vec{r}_s|}{c})}{|\vec{r} - \vec{r}_s|} dr_s^2 + \frac{1}{4\pi c} \int \vec{e}_{rr_s} \vec{n}_s \left( \frac{\partial}{\partial t} + \frac{c}{|\vec{r} - \vec{r}_s|} \right) \frac{p(\vec{r}_s, t - \frac{|\vec{r} - \vec{r}_s|}{c})}{|\vec{r} - \vec{r}_s|} dr_s^2 . \quad (3.19)$$

It can be used together with the *method of mirroring* to calculate the pressure in front of a finite source that is located in the plane  $z = 0$  and radiates into the half space  $z > 0$  :

$$p(\vec{r}, t) = \frac{1}{2\pi c} \int_{\mathcal{S}} \vec{e}_R \vec{n}_s \left( \frac{\partial}{\partial t} + \frac{c}{R} \right) \frac{p(\vec{r}_s, t - \frac{R}{c})}{R} dr_s^2 \quad (3.20)$$

where  $R = |\vec{r} - \vec{r}_s|$ ,  $\vec{e}_R = \frac{\vec{r} - \vec{r}_s}{R}$ , and  $\vec{n}_s$  is the outward unit vector perpendicular on the surface,  $\mathcal{S}$ . This special result holds under the assumptions of Dirichlet boundary conditions i.e. the pressure and time derivative of particle velocity is zero on the  $z = 0$  plane outside the transducer surface. This is also called a pressure released baffle. For a more detailed discussion whether to use a pressure released, rigid baffle or no baffle at all see [19]. Whether or not the factor  $\vec{e}_R \vec{n}_s$  is included has, in practice, no significant influence on the received signal as long as the ultrasound beam is not steered at high angles towards the sides.

If  $R \gg \frac{1}{k} = \frac{c}{\omega}$ , which is typically the case for  $R > 1\text{mm}$  for frequencies of interest in the range  $f > 2\text{MHz}$ , the second term in the parentheses can be neglected, giving the Huygens-Fresnel form of equation 3.20:

$$p(\vec{r}, t) = \frac{1}{2\pi c} \int_{\mathcal{S}} \vec{e}_R \vec{n}_s \frac{\partial}{\partial t} \frac{p(\vec{r}_s, t - \frac{R}{c})}{R} dr_s^2 . \quad (3.21)$$

Approximative solutions of this integral for varying geometrical forms of the radiating baffle can be found in[24][25][19].

Until now, we have considered and solved the wave equation only under the assumption of a homogeneous medium. However, this is not the case for biological tissue where we

have a complex composite of materials such as fat, muscle, connective tissue and blood, which again can be decomposed into cells with different acoustic characteristics. These inhomogeneities are the reason we receive echoes at all and thus can image inner structures of the (human) body. However, the acoustic properties of the different materials are very similar to each other. We can therefore use a scattering model as described below.

### 3.3.2 Scattering from inhomogeneous material

We now allow for mass density as well as compressibility to vary with the location, i.e.:

$$\rho = \rho(\vec{r}) = \rho_0(\vec{r}) + \rho_1(\vec{r}, t) \quad . \quad (3.22)$$

Equations 3.13<sup>7</sup>–3.15 then take a slightly different form:

$$\frac{\partial}{\partial t} \rho_1 + \rho_0 \nabla \vec{v}_1 + \nabla \rho_0 \vec{v}_1 = 0 \quad (3.23)$$

$$\rho_0 \frac{\partial}{\partial t} \vec{v}_1 + \nabla p_1 = 0 \quad (3.24)$$

$$\begin{aligned} \frac{d}{dt} p_{inst} &= \frac{1}{\kappa_{inst} \rho_{inst}} \frac{d\rho_{inst}}{dt} \\ \Leftrightarrow \frac{\partial}{\partial t} p_{inst} + \vec{v}_{inst} \nabla p_{inst} &= \frac{1}{\kappa_{inst} \rho_{inst}} \left( \frac{\partial}{\partial t} \rho_{inst} + \vec{v}_{inst} \nabla \rho_{inst} \right) \\ \Rightarrow \frac{\partial}{\partial t} p_1 &= c^2 \left( \frac{\partial}{\partial t} \rho_1 + \vec{v}_1 \nabla \rho_0 \right) \end{aligned} \quad (3.25)$$

where  $c$  is the locally varying velocity of sound. From this, we can derive a wave equation for inhomogeneous material taking the form:

$$\begin{aligned} \nabla \left( \frac{1}{\rho_0} \nabla p \right) - \frac{1}{c^2 \rho_0} \frac{\partial^2}{\partial t^2} p &= 0 \\ \Leftrightarrow \nabla \frac{1}{\rho_0} \nabla p + \frac{1}{\rho_0} \nabla^2 p - \frac{1}{c^2 \rho_0} \frac{\partial^2}{\partial t^2} p &= 0 \\ \Leftrightarrow \nabla^2 p - \frac{1}{c^2} \frac{\partial^2}{\partial t^2} p &= -\rho_0 \nabla \frac{1}{\rho_0} \nabla p \\ \Leftrightarrow \nabla^2 p - \frac{1}{c_a^2} \frac{\partial^2}{\partial t^2} p &= -\rho_0 \nabla \frac{1}{\rho_0} \nabla p - \left( \frac{1}{c_a^2} - \frac{1}{c^2} \right) \frac{\partial^2}{\partial t^2} p \\ \Leftrightarrow \nabla^2 p - \frac{1}{c_a^2} \frac{\partial^2}{\partial t^2} p &= \frac{1}{\rho_0} \nabla \rho_0 \nabla p - \frac{1}{c_a^2} \left( 1 - \frac{c_a^2}{c^2} \right) \frac{\partial^2}{\partial t^2} p \end{aligned} \quad (3.26)$$

<sup>7</sup>For mass conservation, we have:  $\frac{\partial \rho}{\partial t} + \nabla(\rho \vec{v}) = \frac{\partial \rho}{\partial t} + \nabla \rho \vec{v} + \rho \nabla \vec{v} = \frac{d}{dt} \rho + \rho \nabla \vec{v}$

Here,  $c_a$  is an average of the locally varying velocity of sound,  $c$ , and we have again dropped the index of the pressure. Finally, we introduce the scattering coefficients:

$$\beta = \left(1 - \frac{c_a^2}{c^2}\right) \quad , \quad \gamma = \frac{1}{\rho} \nabla \rho = \nabla \ln(\rho) \quad (3.27)$$

thus the wave equation takes the form:

$$\nabla^2 p - \frac{1}{c_a^2} \frac{\partial^2}{\partial t^2} p = -\frac{\beta}{c_a^2} \frac{\partial^2}{\partial t^2} p + \gamma \nabla p \quad . \quad (3.28)$$

Our notation is similar to that used in [26] whereas [19] and [27] use changes in the adiabatic compressibility instead of changes in the velocity of sound and get at a slightly different form.

The scattering terms on the right side of the equation correspond to a source term,

$$f_{src}(\beta, \gamma, p) = -\frac{\beta}{c_a^2} \frac{\partial^2}{\partial t^2} p + \gamma \nabla p \quad , \quad (3.29)$$

that excites a scattered wave. A perturbation approach is commonly used to calculate this scattered wave field. Because also the inhomogeneous wave equation is linear, we can develop it as follows:

$$\begin{aligned} \nabla^2 p_0(\vec{r}, t) - \frac{1}{c_a^2} \frac{\partial^2 p_0(\vec{r}, t)}{\partial t^2} &= 0 \\ \nabla^2 p_1(\vec{r}, t) - \frac{1}{c_a^2} \frac{\partial^2 p_1(\vec{r}, t)}{\partial t^2} &= f_{src}(\vec{r}, t, p_0(\vec{r}, t)) \\ \nabla^2 p_2(\vec{r}, t) - \frac{1}{c_a^2} \frac{\partial^2 p_2(\vec{r}, t)}{\partial t^2} &= f_{src}(\vec{r}, t, p_1(\vec{r}, t)) \\ \vdots &= \quad \quad \quad \vdots \end{aligned} \quad (3.30)$$

where equal order terms are grouped together and the actual pressure,  $p(\vec{r}, t)$ , is the given by:

$$p(\vec{r}, t) = \sum_{i=0}^{\infty} p_i(\vec{r}, t) \quad . \quad (3.31)$$

Assuming that the scatter parameters  $\beta$  and  $\gamma$  are sufficiently small,  $p_i$  will converge rapidly with increasing  $i$  and we can break the series in equation 3.30 after the second term.

With this we get the scattered field in the Born approximation:

$$p_{sc}(\vec{r}, t) = p_1(\vec{r}, t) \quad . \quad (3.32)$$

Consequently, to calculate the scattered field, we first calculate the field radiated from the transducer into a homogeneous medium ( $\beta = 0$ ,  $\gamma = 0$ ,  $c = c_a$ ). The result is then used to get the equivalent source term for the scattered field. Finally, the scattered field is obtained by convolution with Green's function for free space:

$$\begin{aligned}
p_{sc}(\vec{r}, t) &= \int \int g(\vec{r}, \vec{r}_1, t, t_1) \cdot f_{src}(\vec{r}_1, t_1) dr_1^3 dt_1 \\
&= \int \frac{\delta(t - \frac{|\vec{r} - \vec{r}_1|}{c})}{4\pi|\vec{r} - \vec{r}_1|} * f_{src}(\vec{r}_1, t) dr_1^3 \\
&= \int \frac{\delta(t - \frac{|\vec{r} - \vec{r}_1|}{c})}{4\pi|\vec{r} - \vec{r}_1|} * \left( \frac{\beta(\vec{r}_1)}{c_a^2} \frac{\partial^2}{\partial t^2} p_0(\vec{r}_1, t) + \gamma(\vec{r}_1) \nabla_{r_1} p_0(\vec{r}_1, t) \right) dr_1^3
\end{aligned} \tag{3.33}$$

Now we have all components to set up the spatial echo impulse response.

### 3.3.3 Spatial echo impulse response

Assuming a white transfer function of the transducer crystal(s), a current impulse,  $i(t) = \delta(t)$ , at the electric port will generate a pressure distribution:

$$p(\vec{r}_0, t) = a_s(\vec{r}_0) \cdot \delta(t - \tau_t(\vec{r}_0)) \tag{3.34}$$

where  $a_s(\vec{r}_0)$  is the apodization function over the transducer surface and  $\tau(\vec{r}_0)$  the delay function to enable focusing and/or steering of the ultrasound beam. The pressure distribution over the transducer surface impinged by the backscattered ultrasound will result in a pulse at the electric port given by:

$$i_r(t) = \int_{\mathcal{A}} a_r(\vec{r}_2) \cdot p_{sc}(\vec{r}_2, t - \tau_r(\vec{r}_2)) dr_2^2 \tag{3.35}$$

where  $a_r(\vec{r}_2)$  is the receive apodization function and  $\tau_r(\vec{r}_2)$  the receive delay function, which may differ from the respective functions when transmitting the ultrasound pulse. The spatial echo impulse response,  $s(t)$ , is defined as  $i_r(t) = s(t) * i(t)$ . With equations 3.21, 3.33 and 3.35, we get:

$$\begin{aligned}
s(t) &= \int_{\mathcal{A}} a_r(\vec{r}_2) \int \frac{\delta(t - \tau_r(\vec{r}_2) - \frac{|\vec{r}_2 - \vec{r}_1|}{c_a})}{4\pi|\vec{r}_2 - \vec{r}_1|} * \left( \frac{\beta(\vec{r}_1)}{c_a^2} \frac{\partial^2}{\partial t^2} + \gamma(\vec{r}_1) \nabla_{r_1} \right) \\
&\quad \frac{1}{2\pi c_a} \int_{\mathcal{A}} \vec{e}_{10} \vec{n}_A a_s(\vec{r}_0) \frac{\partial}{\partial t} \frac{\delta(t - \tau_t(\vec{r}_0) - \frac{|\vec{r}_1 - \vec{r}_0|}{c_a})}{|\vec{r}_1 - \vec{r}_0|} dr_0^2 dr_1^3 dr_2^2 \\
&= \frac{1}{2c_a} \int \int_{\mathcal{A}} a_r(\vec{r}_2) \frac{\delta(t - \tau_r(\vec{r}_2) - \frac{|\vec{r}_2 - \vec{r}_1|}{c_a})}{2\pi|\vec{r}_2 - \vec{r}_1|} dr_2^2 * \frac{\partial}{\partial t} \left( \frac{\beta(\vec{r}_1)}{c_a^2} \frac{\partial^2}{\partial t^2} + \gamma(\vec{r}_1) \nabla_{r_1} \right) \\
&\quad \int_{\mathcal{A}} \vec{e}_{10} \vec{n}_A a_s(\vec{r}_0) \frac{\delta(t - \tau_t(\vec{r}_0) - \frac{|\vec{r}_1 - \vec{r}_0|}{c_a})}{2\pi|\vec{r}_1 - \vec{r}_0|} dr_0^2 dr_1^3 \\
&= \frac{1}{2c_a} \int h_r(\vec{r}_1, t) * \frac{\partial}{\partial t} \left( \frac{\beta(\vec{r}_1)}{c_a^2} \frac{\partial^2}{\partial t^2} + \gamma(\vec{r}_1) \nabla \right) h_t(\vec{r}_1, t) dr_1^3 \tag{3.36}
\end{aligned}$$

where  $\vec{e}_{10} = \frac{\vec{r}_1 - \vec{r}_0}{|\vec{r}_1 - \vec{r}_0|}$  and  $h_t(\vec{r}_1, t)$ ,  $h_r(\vec{r}_1, t)$  are the respective beam profiles for transmitting and receiving. Typical beam profiles were shown in figure 2.3 for a monochrome situation. Partial integration applying the Gauss theorem followed by calculation of the gradients including some approximations of the same order as already made (see appendix A for details), gives:

$$\begin{aligned}
s(t) &= \frac{1}{2c_a^3} \frac{\partial^3}{\partial t^3} \int h_r(\vec{r}_1, t) * h_t(\vec{r}_1, t) [\ln(\rho(\vec{r}_1)) + \beta(\vec{r}_1)] \\
&\quad + \vec{h}_r(\vec{r}_1, t) * \vec{h}_t(\vec{r}_1, t) \ln(\rho(\vec{r}_1)) dr_1^3 \tag{3.37}
\end{aligned}$$

where

$$\vec{h}_r(\vec{r}_1, t) = \int_{\mathcal{A}} \vec{e}_{12} a_r(\vec{r}_2) \frac{\delta(t - \tau_r(\vec{r}_2) - \frac{|\vec{r}_2 - \vec{r}_1|}{c_a})}{2\pi|\vec{r}_2 - \vec{r}_1|} dr_2^2 \tag{3.38}$$

and

$$\vec{h}_t(\vec{r}_1, t) = \int_{\mathcal{A}} \vec{e}_{10} (\vec{e}_{10} \vec{n}_A) a_s(\vec{r}_0) \frac{\partial}{\partial t} \frac{\delta(t - \tau_t(\vec{r}_0) - \frac{|\vec{r}_1 - \vec{r}_0|}{c_a})}{2\pi|\vec{r}_1 - \vec{r}_0|} dr_0^2 \tag{3.39}$$

However, if the transmit and receive transducer are identical, integration of  $\vec{e}_{10}$  and  $\vec{e}_{12}$  over  $dr_0^2$  and  $dr_2^2$ , respectively, will result in parallel vectors (at least in a very good approximation, in the case that the apodization functions or delay functions differ), which means that we can drop the vector notation in  $\vec{h}_r(\vec{r}_1, t)$  and  $\vec{h}_t(\vec{r}_1, t)$ .

Defining  $\sigma(\vec{r}_1) = [2 \ln(\rho(\vec{r}_1)) + \beta(\vec{r}_1)]$ , we thus get:

$$s(t) = \frac{1}{2c_a^3} \frac{\partial^3}{\partial t^3} \int h_r(\vec{r}_1, t) * h_t(\vec{r}_1, t) \sigma(\vec{r}_1) dr_1^3 \quad . \quad (3.40)$$

To obtain the electric impulse response for the whole system the spatial echo impulse response must be convolved with the round trip response of equation 3.6:

$$v_{1^{st}order}(t) = \hat{u}(t) * s(t) = u(t) * \frac{1}{2c_a^3} \int h_r(\vec{r}_1, t) * h_t(\vec{r}_1, t) \sigma(\vec{r}_1) dr_1^3 \quad . \quad (3.41)$$

Having found a model describing the relation between the scattering object, the transducer geometry and the RF-signal that is received at the electric port, we continue with deriving a simulation program that will serve to generate artificial ultrasound signals.

### 3.3.4 Simulation program

Ultrasound image generation is a complex process with many aspects and parameters which are difficult to control independently in an experiment. In addition, noise from different sources must always be coped with. Thus, a simulation program where we can control all parameters independently and switch on and off noise will be very useful for getting insight into the imaging process, for studying the influence of various parameters and for evaluating the potential of new filtering algorithms.

Various simulation models are described in literature[28][29][30][31][32]. They operate either in the time or frequency domain. We chose to follow the ideas presented in[28], modifying and extending the algorithm slightly.

#### The algorithm

A simulation program is merely a numerical implementation of equation 3.40 or equation 3.41. This means essentially discretizing the integral for the beam profiles  $h_t(\vec{r}_1, t)$ ,  $h_r(\vec{r}_1, t)$  and the volume integral over the scatterer distribution. We will derive here only the approximation for  $h_t(\vec{r}_1, t)$ , since  $h_r(\vec{r}_1, t)$  has a similar form.

The transducer surface,  $\mathcal{A}$ , is divided into  $N_s = N_x \cdot N_y$  small plane rectangular elements<sup>8</sup>,  $\mathcal{A}_i$ , of the size  $d_x \times d_y$  and with the element centers at  $r_{0i}$ . The orientation of the elements with

<sup>8</sup>These elements are independent of the elements a transducer array may consist of. In fact, each array element would be divided in many simulation elements.

respect to the  $xy$ -plane of a global coordinate system is given by the azimuth and elevation angles,  $\theta_{a,i}$  and  $\theta_{e,i}$ . For the definitions of the coordinate system and vectors used, we refer to figure 3.13. With this we get:

$$\begin{aligned}
 h_i(\vec{r}_1, t) &= \int_{\mathcal{A}} \vec{e}_{10} \vec{n}_{A_i} a_s(\vec{r}_0) \frac{\delta(t - \tau_t(\vec{r}_0) - \frac{|\vec{r}_1 - \vec{r}_0|}{c})}{2\pi |\vec{r}_1 - \vec{r}_0|} d\vec{r}_0^2 \\
 &\approx \sum_{i=1}^{N_s} \int_{\mathcal{A}_i} \vec{e}_{10i} \vec{n}_{A_i} a_s(\vec{r}_{0i} + \vec{r}_i) \frac{\delta(t - \tau_t(\vec{r}_{0i} + \vec{r}_i) - \frac{|\vec{r}_1 - \vec{r}_{0i} - \vec{r}_i|}{c})}{2\pi |\vec{r}_1 - \vec{r}_{0i} - \vec{r}_i|} d\vec{r}_i^2 \quad . \quad (3.42)
 \end{aligned}$$

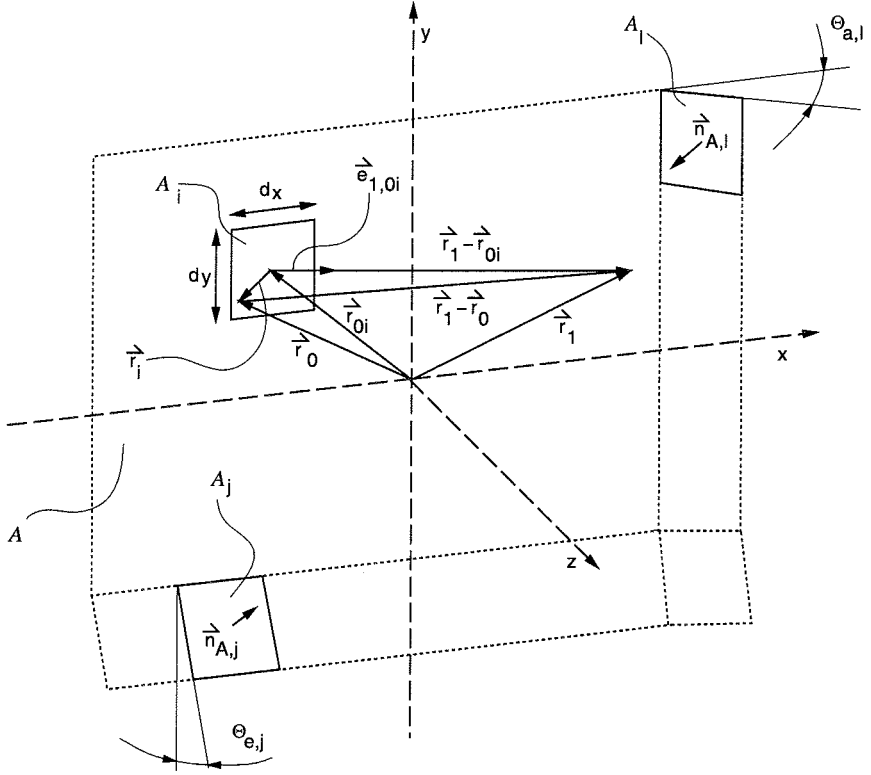


Figure 3.13: Definitions of the vectors used in the simulation model.

If the size of the element,  $\mathcal{A}_i$ , is chosen small enough, the observation point,  $\vec{r}_1$ , lies in the far field<sup>9</sup> (Frauenhofer region) of the element, we can simplify:

<sup>9</sup>The condition here is that  $r_i \ll |\vec{r}_1 - \vec{r}_{0i}|$

$$|\vec{r}_1 - \vec{r}_{0i} - \vec{r}_i| \approx |\vec{r}_1 - \vec{r}_{0i}| - \vec{e}_{10i} \vec{r}_i \quad (3.43)$$

Inserting this into 3.42, neglecting the term  $\vec{e}_{10i} \vec{r}_i$  in the denominator and assuming no apodization or time delay variation over the element, we get:

$$h_t(\vec{r}_1, t) \approx \sum_{i=1}^{N_s} \vec{e}_{10i} \vec{n}_{A_i} a_s(\vec{r}_{0i}) \frac{\delta(t - \tau_t(\vec{r}_{0i}) - \frac{|\vec{r}_1 - \vec{r}_{0i}|}{c})}{2\pi |\vec{r}_1 - \vec{r}_{0i}|} * \int_{\mathcal{A}_i} \delta(t - \frac{\vec{r}_i \vec{e}_{10i}}{c}) dr_i^2 \quad (3.44)$$

The remaining integral can be calculated as:

$$\int_{\mathcal{A}_i} \delta(t - \frac{\vec{r}_i \vec{e}_{10i}}{c}) dr_i^2 = \frac{d_x d_y}{T_x T_y} \text{rect}(\frac{t}{T_x}) * \text{rect}(\frac{t}{T_y}) \quad (3.45)$$

with  $T_x = d_x \vec{e}_x \vec{e}_{10i} / c$  and  $T_y = d_y \vec{e}_y \vec{e}_{10i} / c$ , respectively (see also figure 3.14). Consequently, integrating over the transducer surface to get the beam profiles means merely to sum scaled and delayed versions of trapezoid-functions.

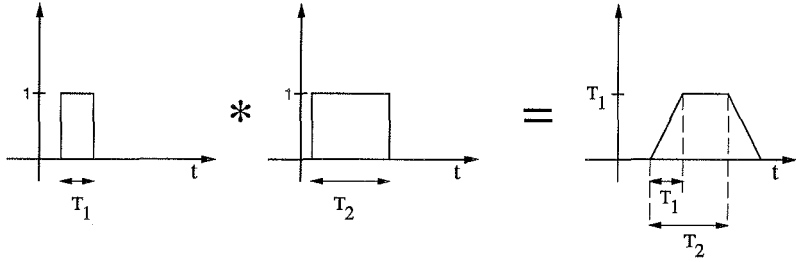


Figure 3.14: Convolution of two rectangular pulses of length,  $T_1$  and  $T_2$  results in a trapezoid-function.

Up to this point, the model is continuous in time. Therefore, we have to look for an appropriate sampling of the signals. The problem is that the pulse defined in equation 3.44 can become arbitrarily short when the target is placed closer and closer to the focus. An infinite sampling frequency would be required in order to represent the pulse correctly. However, we are interested in keeping the simulation frequency as low as possible in order to minimize the computational overhead. On the other hand,  $h_t(\vec{r}_1, t)$  is convolved with the band limited RF-pulse,  $u(t)$ , and consequently a sampling frequency satisfying the Nyquist criterion for the resulting signal can be determined.

We applied the following strategy to discretize the pulse of equation 3.44 (see also figure 3.15). It is sampled according to a chosen sampling frequency that exceeds the Nyquist

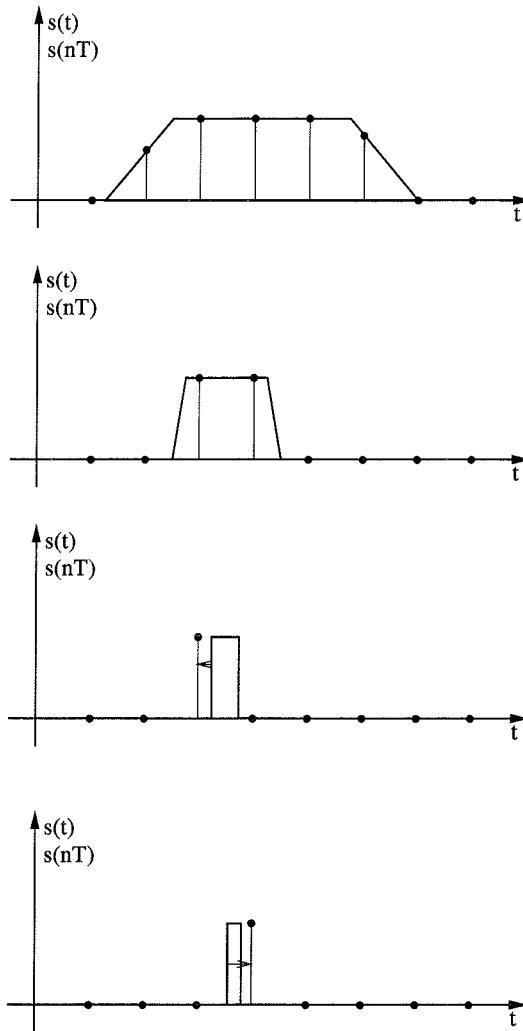


Figure 3.15: Examples showing how the analog trapezoid functions are discretized.

limit given from the RF-pulse. If the pulse length is shorter than a sample time step, it is set to a discrete Dirac pulse with equal signal energy in order not to lose its contribution.

Here, an error is introduced and it is obvious that it decreases with increasing simulation sampling rate. We will analyze this error in the frequency domain and look first at the amplitude component. An analog *rect*-pulse that is just shorter than  $T < \frac{1}{f_s}$  will have a Dirac pulse as its discrete version and has thus a white Fourier spectrum. On the other hand the Fourier spectrum for the analog pulse is:

$$\mathcal{F}\left\{\frac{1}{T}\text{rect}\left(\frac{t}{T}\right)\right\} = \text{sinc}(\pi f T) \quad . \quad (3.46)$$

This function is plotted for the two values  $T = 10\text{ns}$  and  $T = 20\text{ns}$  in figure 3.16. If we

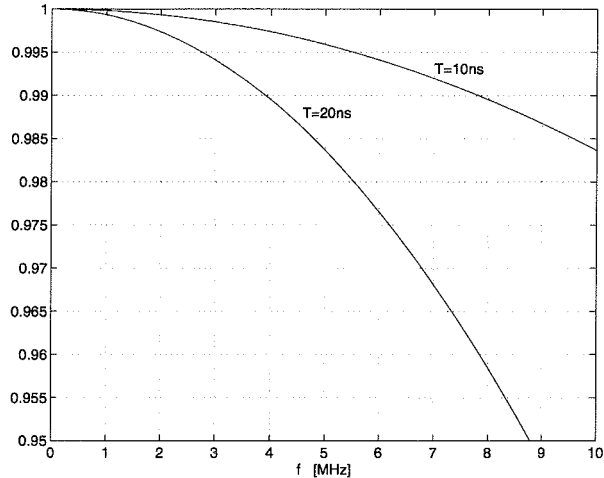


Figure 3.16: Fourier transform of a *rect*-pulse with a pulse width of  $T = 10\text{ns}$  and  $T = 20\text{ns}$ .

require that the Fourier spectrum of the original signal does not deviate more than 1% from the one of the approximation within the frequency band of the RF-pulse, we see that it is sufficient to sample with  $f_s = \frac{1}{20\text{ns}} = 50\text{MHz}$ , when the RF-pulse has an upper band limit of  $f_{max} = 4\text{MHz}$ . Correspondingly, because we have a linear relation, a sample frequency of 100MHz would be necessary, when the upper RF-pulse band limit is  $f_{max} = 8\text{MHz}$ . Or, we see that at a sample frequency of 100MHz, the error for a transducer with  $f_{max} = 4\text{MHz}$  is less than 0.9975.

Yet we have to consider the effect of a phase error also. A discrete Dirac pulse will

always be synchronous to the sampling rate. Hence, a short pulse will be shifted in time up to half the sample step size (since we will always shift it to the nearest sample instance). The difference between the exact and shifted pulse will thus be proportional to:

$$d(t) = \delta(t) - \delta(t \pm \frac{1}{2f_s}) \quad (3.47)$$

or written in the frequency domain:

$$D(f) = |(1 - e^{\pm j\pi f/f_s})| \quad (3.48)$$

Demanding this factor to be less than 1% in the interesting frequency range,  $f < f_{max}$ , gives:

$$f_s/f_{max} > 314 \quad (3.49)$$

For a transducer with the upper band limit at  $f_{max} = 4\text{MHz}$ , that means a sampling frequency of 1.26GHz! Such a high rate exceeded the capabilities of our machine, a Sun Sparc2<sup>TM</sup> and later a 166MHz-Pentium<sup>TM</sup> running Linux, in terms of computation time and memory requirements. We used instead a sampling frequency of 100MHz, which will result in a relative error of 12.5% at  $f_{max} = 4\text{MHz}$  and 9.4% at 3MHz. But one should remember that this boundary is an upper limit and that the error will be averaged out to some degree if many scatterers are involved.

A further critical parameter influencing the accuracy of the model is the number or, equivalently, the size of the simulation elements. The condition is that we have to be in the far field of the individual element, which leads to[28]:

$$d \ll \sqrt{4r_1c_a/f_{max}} \quad (3.50)$$

Additionally, in the case of mechanically focused transducers, we have to be aware of the geometrical error introduced by the approximation of the transducer surface by small plane rectangles. As the authors of [33] point out, this error can require a smaller element size than that given by equation 3.50.

### 3.3.5 Program validation

The algorithm was implemented in C-code and thoroughly tested conducting phantom experiments in a water tank. For the test, we used the 3MHz transducer described in section 3.2.2. The transducer probe was fixed in a rack so that the transducer could be immersed

in the water. The reflecting target was mounted on an arm in the water tank. This arm could be translated in all three dimensions by step motors with a minimal step size of  $10\mu\text{m}$ . The received electrical signal at the transducer was amplified (between 0–50dB), bandpass filtered and then analyzed in a digital oscilloscope operating at a sampling frequency of 800MHz.

For the simulations, the transducer surface was represented by  $N = 2512$  rectangular elements with a side length of 0.25mm.

The transducer RF-pulse (see figure 3.10) needed for the simulations was measured placing a point target (a 0.1mm thin needle) into the focus.

### Point target

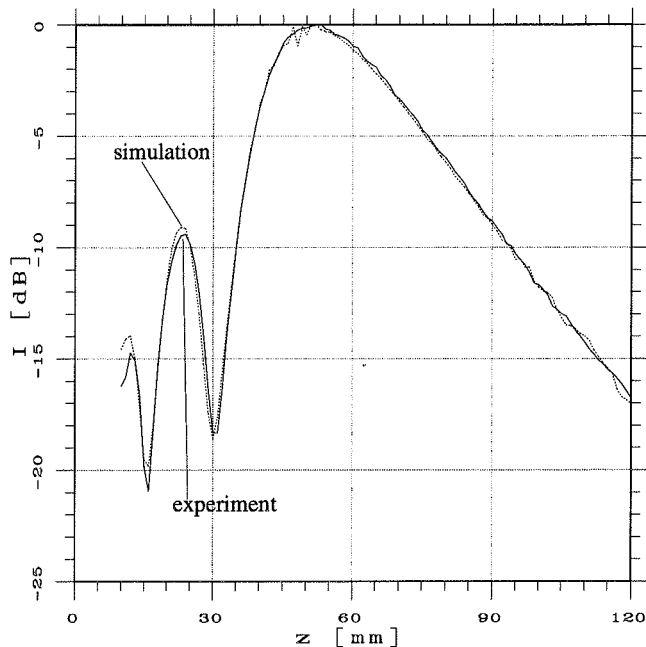


Figure 3.17: On-axis beam profile of a two element annular array transducer. Comparison between experiment and simulation.

In a first series of experiments, we used a needle as a point target. We scanned the beam profile<sup>10</sup> along the center axis of the transducer and three profiles along lines perpendicular

<sup>10</sup>The root mean square (RMS) value of the received RF-pulse echo is calculated.

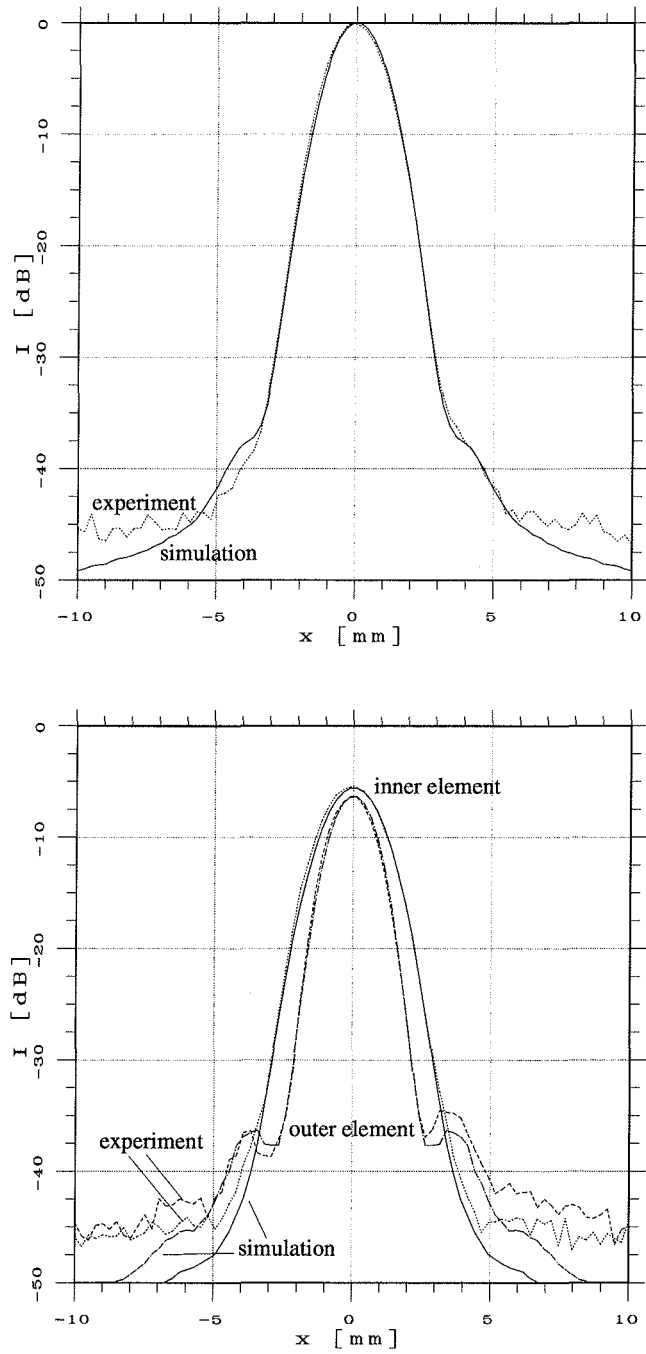


Figure 3.18: Lateral beam profile (two ways) at a range of 70mm. Received summed signal (top) and received signals of the inner and outer element (bottom). Comparison between experiment and simulation.

to the center axis. These three off-axis profiles were recorded at the ranges 40mm, 70mm and 90mm. The corresponding curves were calculated by the simulation program. Figures 3.17 and 3.18 show the comparison between the experimental and simulated profiles for the on-axis beam profile and the off-axis profile at 70mm. For the other off-axis plots the reader should refer to Appendix A. We see that experiment and simulations correspond nicely. Even the near field of the transducer from 10mm to 20mm is calculated quite accurately.

### Extended target

We studied the performance of the simulation model further by replacing the point target that scatters the ultrasound in all directions with a target object that had larger dimensions. This means that the received echo response will also depend on the orientation of the object with respect to the transducer and not just its position. A 4.75mm  $\times$  4.75mm thick rectangular Plexiglas rod served as target. It was placed on the transducer axis with its plane surface perpendicular to the axis as accurately as this was possible to adjust. The on-axis beam profile was measured.

In the simulation, the target surface was represented by an equi-distant point grid. Here, again, the question of appropriate grid spacing comes up. Intuitively, it should be chosen equal to that of the transducer surface representation (in our case 0.25mm). However, in order to cut down the calculation overhead of the simulation, we were interested in increasing this value. Therefore, we examined the convergence behavior of the simulated echo response when decreasing the grid spacing or, equivalently, increasing the number of points,  $N_t$ , that represent the object surface. The convergence depends, of course, on the range where the object is placed. Echo signals from targets at larger ranges converge more rapidly. In figure 3.19, the relative error between the simulated echo response and its limit is plotted over  $N_t$  for two ranges, 30mm and 100mm. The error is less for larger ranges, as expected. We can conclude that choosing  $N_t = 49$ , which corresponds to a grid spacing of 0.79mm, results in an echo response that deviates less than 6% from the echo response with continuous surface representation for ranges  $r > 30$ mm.

Having determined this parameter, we calculated the on-axis beam profile and compared it with the experiment results (see figure 3.20). We see that for ranges greater than 30mm both curves correspond well. The deviation is less than 1dB. This deviation is mostly due to the variance of the values in the experiment.

We cannot expect our simulation program to perform much better. The accuracy is in

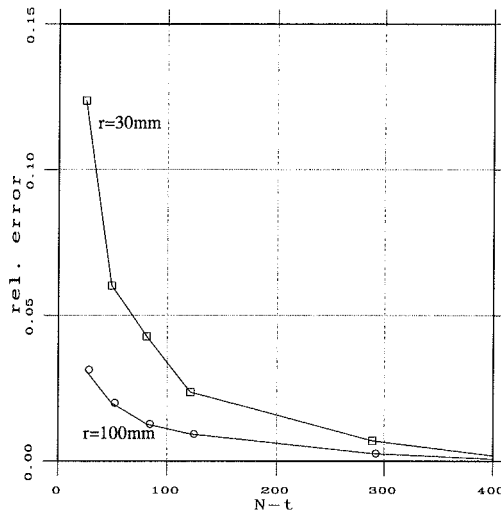


Figure 3.19: Convergence of the relative error between the simulated echo response and its simulated limit versus increasing the number of grid points. The plane rectangular object is located at a range of 30mm and 100mm on the transducer axis.

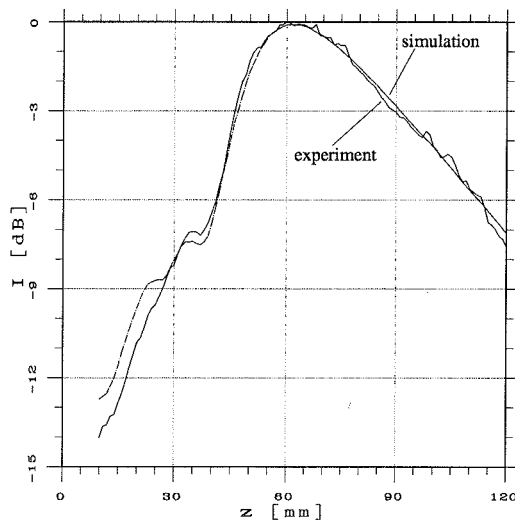


Figure 3.20: On-axis beam profile (RMS values of the received echos) from a 4.75mm  $\times$  4.75mm plane surface reflector. Comparison between simulation and experiment.

the same order as reported by other researchers[28]. Reasons for the deviations are limited accuracy in positioning and orienting the reflecting target with reference to the transducer surface, as well as acoustic and electronic noise.

Further, we represented only the top surface of the Plexiglas target and neglected all creeping waves. Finally, as pointed out before, the simplifying assumptions made in the derivation of our model will contribute to the deviations especially in the near field.

Anyway, the validation tests have shown that our simulation model is in good correspondence with reality. Therefore, we may draw conclusions directly from simulation results without proving these experimentally in every detail. But it is clear that essential assumptions or results of further modeling should always be verified by experiments.

### 3.4 Reverberations

So far, we have introduced a signal model that is commonly used, perhaps with slight variations, to describe the ultrasound imaging process. But this model neglects acoustic noise; this is a consequence of the Born approximation which neglects all kind of multiple scattering. However, having strong scatterers within the ultrasound beam and a large dynamic range (typically 60dB) for the detectable signal amplitude, we reach the validity limits of the Born approximation. Consequently, we take into consideration higher order terms in the source term on the right side of equation 3.30. Each further scattering is accompanied by an amplitude attenuation proportional to the reflectivity of the scattering medium. We will therefore limit our considerations to higher order cases only where two or three reflectors are incorporated.

It should be noted that the transducer itself can be one of the reflectors. It has a well defined and smooth reflecting surface and lies, of course, within the ultrasound beam. Even though it is possible to cut down the reflection factor by proper transducer design[34] (including  $\lambda/4$  matching layers and electric impedance matching), the reflectivity of a commercially available transducer still lies around  $R \approx 0.2-0.3$ .

At first glance, one would model the source pressure distribution for the pulse reflected at the transducer surface as given by the pressure distribution of the incoming echo multiplied with the reflection factor,  $R$ , of the tissue transducer interface. However, the transducer is a more complex reflector and we find that the electrodes which define the transducer element(s) play an important role. We will investigate these relations in the following

section.

### 3.4.1 A model for the transducer reflection factor

In the one-dimensional case the transducer can be appropriately described by the KLM model [21] and we can calculate the transducer reflection factor. It can also be measured, if we have a plane wave hitting the plane transducer perpendicularly. However, if the plane wave hits the transducer at an angle or if the phase fronts of the incoming wave are not plane, the situation is more intriguing.

An incoming spherical wave front,  $p_i$ , will activate the piezoelectric material only at the infinitesimal small area,  $dA$ , that the wave is covering at that instant in time (figure 3.21). An electric field is developed which leads to a difference in the electric potential between the two opposite sides of the transducer on the active area. Once this difference exists, it spreads quasi-simultaneously (within the order of the velocity of light) over the electrodes. The active area thus excites the rest of the transducer element, and this will lead to a re-radiation. Because the area of the electrodes is large compared to the active area, the situation is the same as if the transducer is shorted. For this short-cut situation, we can calculate or measure a reflection factor. It is the one by which the incoming pressure wave is reflected from the active area. It is purely acoustic and does not depend on the electric receive impedance but varies according to the characteristic impedance and thickness of the backing, the piezoelectric material and the matching layer(s). We call this component the acoustic component of the reflection factor,  $r_{ac}$ .

On the other hand, we will find a re-radiated wave due to the short-cut current that drives the rest of the transducer element defined by the electrodes. It will generate a uniform vibration over the transducer element surface just as the original excitation voltage did. From our two-port model in section 3.2, we get for the short-cut current:

$$\mathcal{F}\{i_{sc}\} = 2H_{tt}(f) \cdot \mathcal{F}\{p_i\}dA \quad . \quad (3.51)$$

Note that the current is proportional to the active area. The inner impedance of the equivalent current source representing the active area is inverse proportional to the active area. Thus, the short-cut current drives the impedances  $Z_i \frac{A}{dA}$ ,  $Z_r$ , and  $Z_i \frac{A}{A-dA}$  in parallel, see figure 3.22. It follows that we get the voltage induced by the active area as:

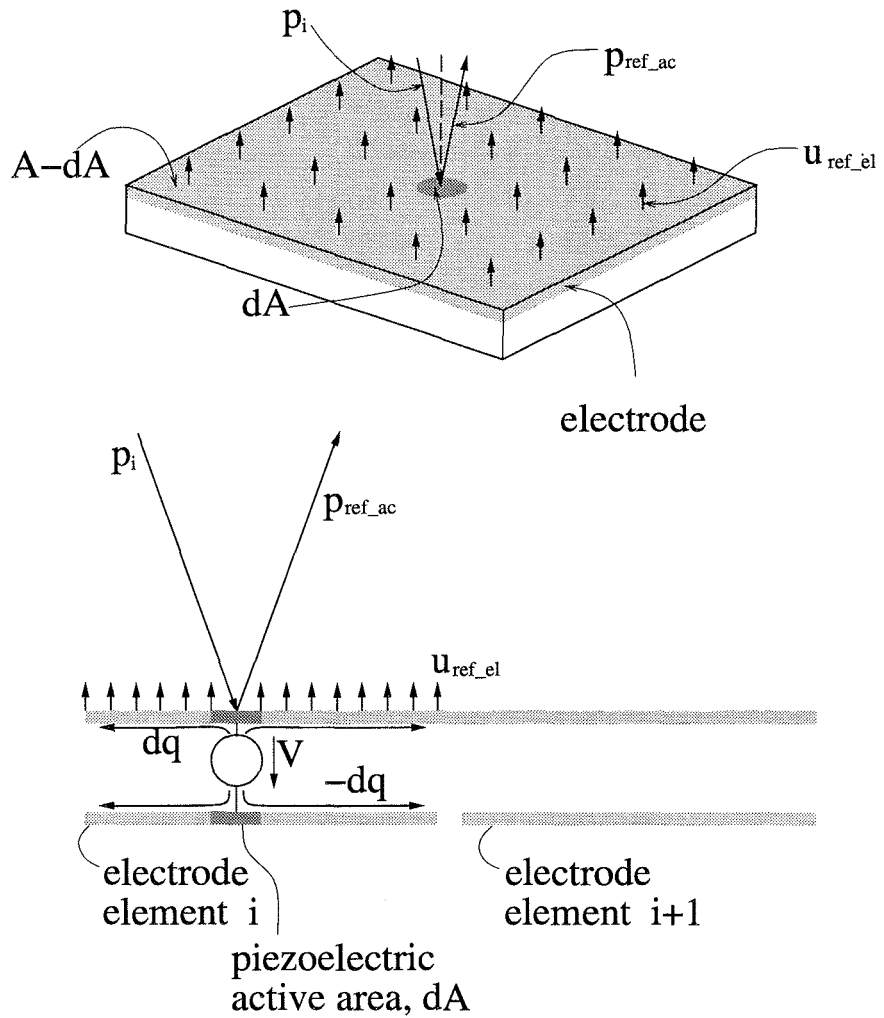


Figure 3.21: Pressure and vibration velocity distribution over a plane transducer reflecting an incoming wave.

$$\begin{aligned} \mathcal{F}\{dV\} &= \frac{Z_i \cdot Z_r}{Z_i + Z_r} \cdot \mathcal{F}\{i_{sc}\} \\ &= H_i(f) \cdot \mathcal{F}\{i_{sc}\} \end{aligned} \quad (3.52)$$

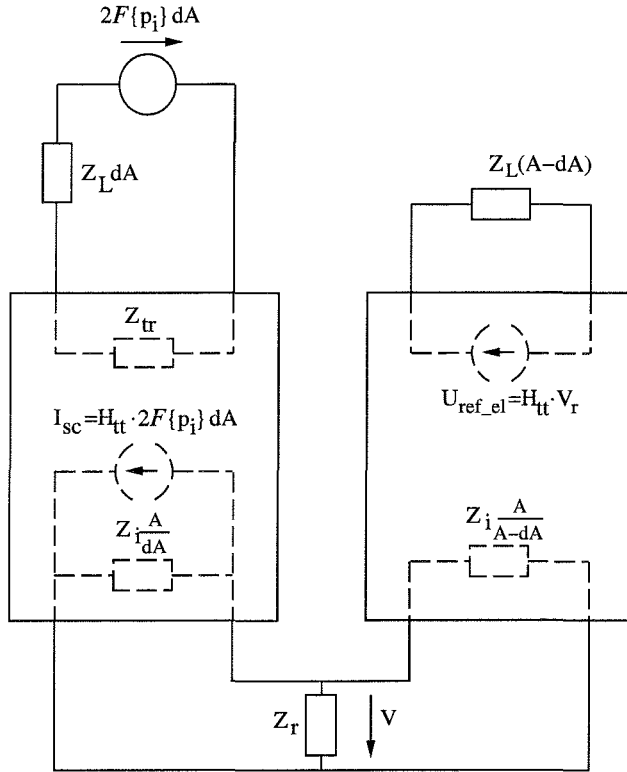


Figure 3.22: Block scheme illustrating the electric re-radiation of an incoming pressure pulse,  $p_i$ .

As pointed out, this voltage simultaneously drives the rest of the transducer element, thus we get the following uniform vibration velocity distribution:

$$\begin{aligned} \mathcal{F}\{u_{ref\_el}\} &= H_{tt}(f) \cdot \mathcal{F}\{dV\} \\ &= 2H_{tt}^2(f)H_i(f)\mathcal{F}\{p_i\}dA \end{aligned} \quad (3.53)$$

The corresponding pressure force is easily found by multiplication with the characteristic impedance,  $Z_L$ . Hence, we get the following expression for the electric component of the reflection factor:

$$r_{el} = 2H_{tt}^2(f)H_i(f)Z_L dA \quad . \quad (3.54)$$

If we assume that a plane wave hits a plane transducer perpendicularly, the incoming pressure is the same all over the surface. This simplifies the spatial integration and for the total reflection factor we get:

$$\begin{aligned} r_{plane} &= r_{el} + r_{ac} \\ &= 2H_{tt}^2(f)H_i(f)Z_L A + r_{ac} \quad . \end{aligned} \quad (3.55)$$

Experimentally, we meet this situation for a point target in the focus of the transducer or using a spherically shaped surface placed a few mm in front of the transducer, where the center of the sphere and the focus of the transducer coincide (see section 3.2.2).

Even though the model seems consistent, we provide a verification in form of an experiment.

### 3.4.2 Verification experiment

From the derivation above, we see that the electric component of the reflection factor and hence the reradiated pulse depends on the receive impedance,  $Z_r$ . Moreover, shorting the receive impedance will cancel the electrically reflected part and only the acoustic reflection will remain. But, of course, shorting the transducer will not produce any output signal. However, this problem can be circumvented using a transducer with two elements where only one element is shorted.

This was done in the experiment described in the following. We again used the 3MHz annular array transducer with two equal area elements. A point target was placed at the focus of the transducer in order to get a quasi-plane wave situation. An ultrasound pulse was emitted and received only at the inner element. The outer element was either shorted electrically or operated with its ordinary receive impedance. The returning first order echo hit the transducer and was reflected according to the reflection factor of the individual elements. Because the acoustic propagation path from the transducer to the focus point

and back had the same length for all points on the transducer surface, the total reflection factor of the transducer was just the sum of the reflection factors of the individual elements:

$$\begin{aligned} r_{tot} &= r_i + r_o \\ &= r_{el,i} + r_{ac,i} + r_{el,o} + r_{ac,o} \end{aligned} \quad (3.56)$$

Since the elements have equal area and are produced with the same material parameters, we find that:

$$r_{ac,i} = r_{ac,o} = r_{ac} \quad (3.57)$$

and for the electric reflection factors depending whether the outer element is shorted or not:

$$r_{el,i} = r_{el} \quad , \quad r_{el,o} = \begin{cases} r_{el} & \text{not shorted} \\ 0 & \text{shorted} \end{cases} \quad (3.58)$$

Now measuring the reverberation pulse for these two cases, we get two signals proportional to the total reflection factor:

$$v_1(t) \propto (2r_{ac} + 2r_{el}) \quad (3.59)$$

and

$$v_2(t) \propto (2r_{ac} + r_{el}) \quad (3.60)$$

Hence, we can decompose:

$$v_{ac}(t) = (v_2(t) - 0.5v_1(t)) \quad (3.61)$$

and

$$v_{el}(t) = (v_1(t) - v_2(t)) \quad (3.62)$$

where  $v_{ac}(t) = k \cdot r_{ac}(t)$ ,  $v_{el}(t) = k \cdot r_{el}(t)$  and  $k$  is a proportionality factor. The signals  $\frac{1}{2}v_1(t)$  as well as  $v_{ac}(t)$  and  $v_{el}(t)$  and their corresponding Fourier transforms are shown in figures 3.23 and 3.24. It is interesting to note that the two components have a phase difference of  $\pi$  and hence keep the overall reflection factor low by destructive interference.

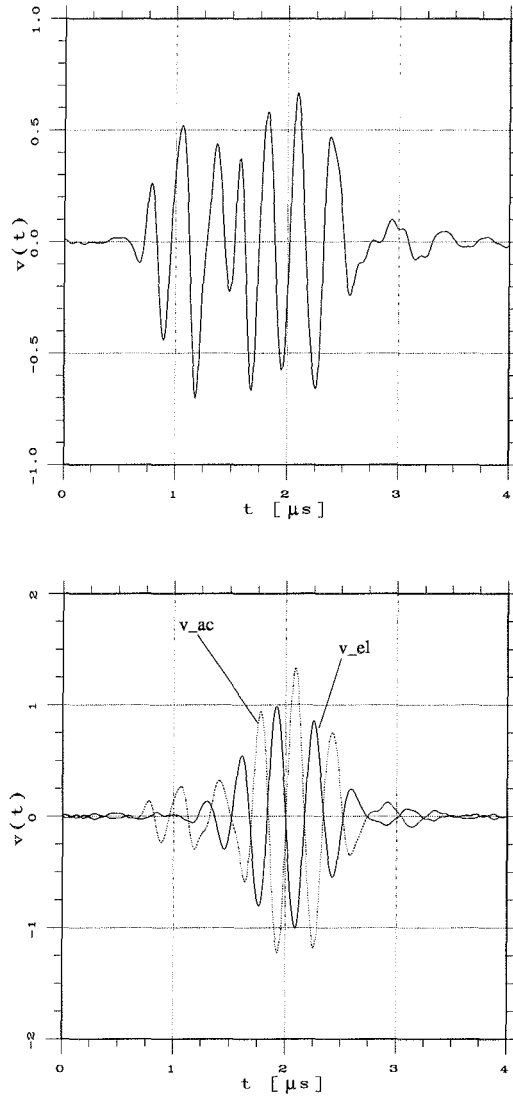


Figure 3.23: Comparison of the reverberation RF-pulse (top) and its acoustic and electric component (bottom). The amplitude is normalized to the maximum of the electric component.

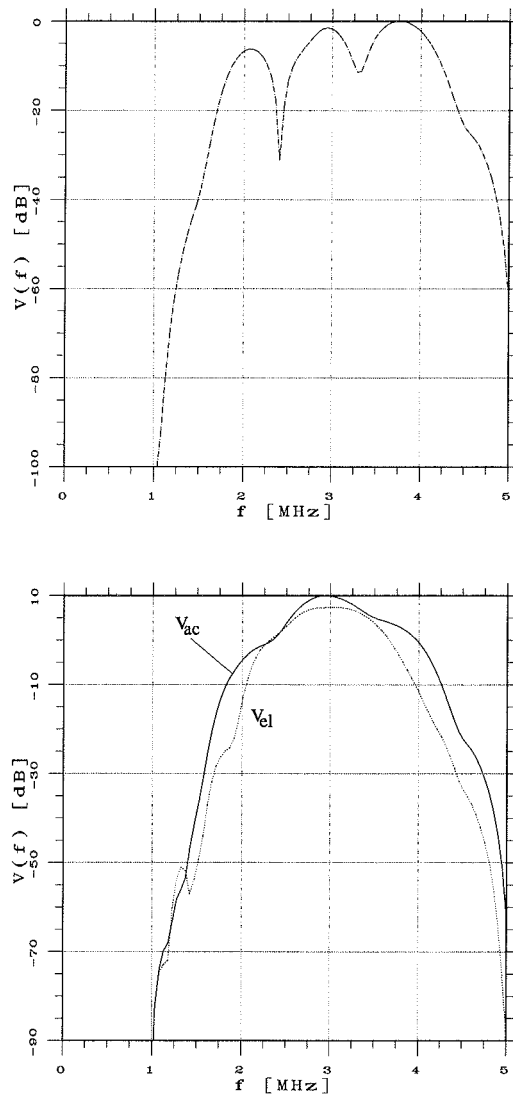


Figure 3.24: Magnitude of the Fourier transforms of the reverberation pulse (top) and its acoustic and electric component (bottom). The plots have a logarithmic scale and are normed to the maximum of the reverberation pulse spectrum.

This signal decomposition is yet not the prove for our model. But, if we can show that we can predict the resulting reverberation pulse when terminating the transducer with an arbitrary impedance enough evidence should be given. For this purpose, we measured also the reverberation echo pulses when shunting the outer element with a pure resistance of  $37\Omega$  and  $70\Omega$ . Once again, from our model, we expect that the acoustic reflection factor stays the same whereas the electric reflection factor changes to:

$$\begin{aligned}
 r_{el,tot} &= r_{el,i} + r_{el,o,sh} \\
 &= r_{el} + r_{el} \frac{\frac{1}{Z_R} + \frac{1}{Z_i}}{\frac{1}{Z_R} + \frac{1}{Z_i} + \frac{1}{Z_{shunt}}} \\
 &= r_{el} \left( 1 + \frac{\frac{1}{Z_R} + \frac{1}{Z_i}}{\frac{1}{Z_R} + \frac{1}{Z_i} + \frac{1}{Z_{shunt}}} \right)
 \end{aligned} \tag{3.63}$$

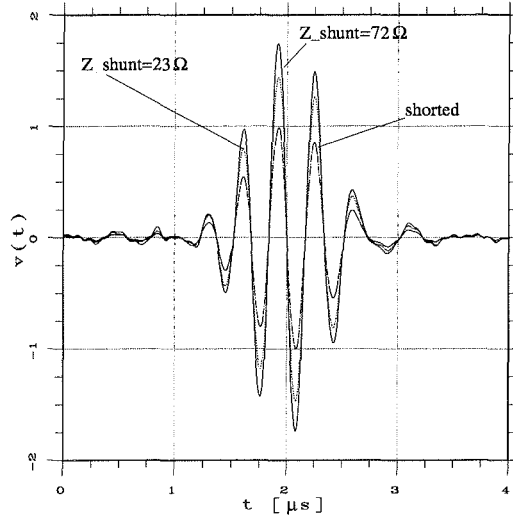


Figure 3.25: Comparison of the electric component of the reverberation pulse when terminating the outer element with a resistance of  $0\Omega$ ,  $23\Omega$  and  $71\Omega$ .

The plot of the outer impedance of the transducer in parallel to the receive impedance,  $Z_R$  was given in figure 3.8 and we see that the magnitude of the inner element stays approximately constant  $|Z| = 28\Omega$ ,  $\varphi = 20^\circ$  in the interesting frequency range from 2MHz to 4MHz. Hence, the pulse form of the electric component will stay constant and there will only be a scaling according to the factor given in equation 3.63.

Extracting the electric reflected signal component of the total signal for the two shunt cases in the same manner as before and comparing it with the ordinary electric reflected component from one element, we see (figure 3.25) that the pulse form is essentially equal and the scaling factors correspond to the calculated ones:

$$\alpha_{23\Omega} = 1.50, \quad \alpha_{72\Omega} = 1.72 \quad (3.64)$$

Furthermore, comparing the extracted acoustic components of the three terminations, we observe that they match perfectly, see figure 3.26.

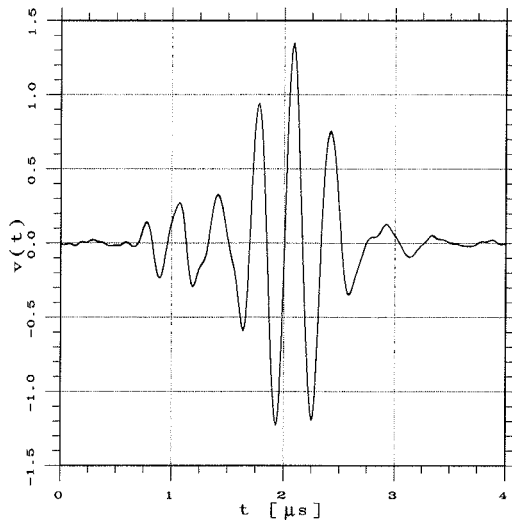


Figure 3.26: Comparison of the acoustic component of the reverberation pulse when terminating the outer element with a resistance of  $0\Omega$ ,  $23\Omega$  and  $72\Omega$ . There is no visible difference.

Having established a model for the reflection factor of the transducer, we now proceed with investigating the pattern of the reverberation beam when the target is not in the focus.

### 3.4.3 Reverberation beam pattern

The major reason for decomposing the reflection factor of the transducer into an acoustic and an electric component is that they are accompanied by different beam patterns. These beam patterns are derived in the following.

**The electric component** of the reflected pulse is generated by a vibration velocity distribution or equivalent pressure distribution that is uniform over an element,  $n$ . In other words, this pressure distribution does not depend on the point,  $\vec{r}_{2i}$ , where the incoming wave hits, but on the time instant when the wave hits the surface. The beam pattern of the reradiated pulse is therefore the same as the beam pattern of the first order pulse of that element. Thus, for the electrically reflected pressure wave:

$$p_{el,n}(\vec{r}_3, t) = \int_{\mathcal{A}_n} \vec{e}_{32} \vec{n}_A \frac{\delta(t - \frac{|\vec{r}_3 - \vec{r}_2|}{c_a})}{2\pi|\vec{r}_3 - \vec{r}_2|} * \frac{1}{c_a} \frac{\partial}{\partial t} p_o(\vec{r}_2, t) dr_2^2 \Big|_{\vec{r}_2 \neq \vec{r}_{2i}} \quad (3.65)$$

where the outgoing pressure distribution,  $p_o(\vec{r}_2, t)$ , is obtained from the incoming pressure,  $p_i(\vec{r}_{2i}, t)$ , by integration and subsequent convolution with the electric reflection factor (see equation 3.54):

$$p_o(\vec{r}_2, t) = r_{el,n}(t) * \frac{1}{A_n} \int_{\mathcal{A}_n} p_i(\vec{r}_{2i}, t) dr_{2i}^2 \quad (3.66)$$

The distribution of the incoming pressure over the transducer surface was already implicitly calculated in section 3.3.3. We thus get:

$$dp_o(\vec{r}_{2i}, t) = r_{el,n}(t) * \frac{1}{A_n} \int_{\mathcal{A}_n} \frac{\delta(t - \frac{|\vec{r}_{2i} - \vec{r}_1|}{c_a})}{4\pi|\vec{r}_{2i} - \vec{r}_1|} dr_1^2 * \frac{1}{c_a^2} \frac{\partial^2}{\partial t^2} \sigma(\vec{r}_1) p(\vec{r}_1, t) dr_1^3 \quad (3.67)$$

Consequently:

$$\begin{aligned} dp_{el,n}(\vec{r}_3, t) &= \int_{\mathcal{A}_n} \vec{e}_{32} \vec{n}_A \frac{\delta(t - \frac{|\vec{r}_3 - \vec{r}_2|}{c_a})}{2\pi|\vec{r}_3 - \vec{r}_2|} * \\ &\frac{1}{c_a} \frac{\partial}{\partial t} \left( r_{el,n}(t) * \frac{1}{A_n} \int_{\mathcal{A}_n} \frac{\delta(t - \frac{|\vec{r}_{2i} - \vec{r}_1|}{c_a})}{4\pi|\vec{r}_{2i} - \vec{r}_1|} dr_{2i}^2 * \frac{1}{c_a^2} \frac{\partial^2}{\partial t^2} \sigma(\vec{r}_1) p(\vec{r}_1, t) dr_1^3 \right) dr_2^2 \Big|_{\vec{r}_2 \neq \vec{r}_{2i}} \\ &= r_{el,n}(t) * \frac{1}{A_n} \int_{\mathcal{A}_n} \vec{e}_{32} \vec{n}_A \frac{\delta(t - \frac{|\vec{r}_3 - \vec{r}_2|}{c_a})}{2\pi|\vec{r}_3 - \vec{r}_2|} dr_2^2 * \int_{\mathcal{A}_n} \frac{\delta(t - \frac{|\vec{r}_{2i} - \vec{r}_1|}{c_a})}{4\pi|\vec{r}_{2i} - \vec{r}_1|} dr_{2i}^2 \\ &\quad * \frac{1}{c_a^3} \frac{\partial^3}{\partial t^3} \sigma(\vec{r}_1) p(\vec{r}_1, t) dr_1^3 \quad (3.68) \end{aligned}$$

Defining:

$$h_{rev,el,n}(\vec{r}_1, \vec{r}_3, t) = \frac{1}{A_n} \int_{\mathcal{A}_n} \frac{\delta(t - \frac{|\vec{r}_{2i} - \vec{r}_1|}{c_a})}{2\pi|\vec{r}_{2i} - \vec{r}_1|} dr_{2i}^2 * \int_{\mathcal{A}_n} \vec{e}_{32} \vec{n}_A \frac{\delta(t - \frac{|\vec{r}_3 - \vec{r}_2|}{c_a})}{2\pi|\vec{r}_3 - \vec{r}_2|} dr_2^2 \Big|_{\vec{r}_{2i} \neq \vec{r}_2} \quad (3.69)$$

we get the pressure wave due to the electric reflection for the whole transducer as the sum over individual element contributions:

$$\begin{aligned} dp_{el}(\vec{r}_3, t) &= \sum_n r_{el,n}(t) * h_{rev,el,n}(\vec{r}_1, \vec{r}_3, t) * \frac{1}{2c_a^3} \frac{\partial^3}{\partial t^3} \sigma(\vec{r}_1) p(\vec{r}_1, t) dr_1^3 \\ &= r_{el}(t) * h_{rev,el}(\vec{r}_1, \vec{r}_3, t) * \frac{1}{2c_a^3} \frac{\partial^3}{\partial t^3} \sigma(\vec{r}_1) p(\vec{r}_1, t) dr_1^3 \end{aligned} \quad (3.70)$$

where we have assumed that the elements have equal area and equal material parameters i.e.  $r_{el,n}$  is the same for all elements.

**For the acoustic component** we find that the reflected pulse is emitted directly from the point where the incoming wave hits. The pressure distribution for the reflected pulse is hence:

$$p_{2o}(t, \vec{r}_{2i}) = r_{ac}(t) * p_{2i}(t, \vec{r}_{2i}) \quad (3.71)$$

The incoming pressure is the same as above. Consequently we have:

$$dp_{2o}(t, \vec{r}_{2i}) = r_{ac}(t) * \frac{\delta(t - \frac{|\vec{r}_{2i} - \vec{r}_1|}{c_a})}{4\pi |\vec{r}_{2i} - \vec{r}_1|} * \frac{1}{c_a^2} \frac{\partial^2}{\partial t^2} \sigma(\vec{r}_1) p(\vec{r}_1, t) dr_1^3 \quad (3.72)$$

To get the pressure of the acoustically reflected wave component at the position  $\vec{r}_3$ , we convolve with the transducer's Green's function and integrate over the whole surface:

$$dp_{ac}(t, \vec{r}_1, \vec{r}_3) = r_{ac}(t) * \frac{1}{c_a} \frac{\partial}{\partial t} \int_{\mathcal{A}} \vec{e}_{32i} \vec{n}_A \frac{\delta(t - \frac{|\vec{r}_3 - \vec{r}_{2i}|}{c_a})}{2\pi |\vec{r}_3 - \vec{r}_{2i}|} * \frac{\delta(t - \frac{|\vec{r}_{2i} - \vec{r}_1|}{c_a})}{4\pi |\vec{r}_{2i} - \vec{r}_1|} dr_{2i}^2 * \frac{1}{c_a^2} \frac{\partial^2}{\partial t^2} \sigma(\vec{r}_1) p(\vec{r}_1, t) dr_1^3. \quad (3.73)$$

Defining:

$$h_{rev,ac}(\vec{r}_1, \vec{r}_3, t) = \int_{\mathcal{A}} \vec{e}_{32i} \vec{n}_A \frac{\delta(t - \frac{|\vec{r}_{2i} - \vec{r}_1|}{c_a} - \frac{|\vec{r}_3 - \vec{r}_{2i}|}{c_a})}{4\pi^2 |\vec{r}_{2i} - \vec{r}_1| |\vec{r}_3 - \vec{r}_{2i}|} dr_{2i}^2, \quad (3.74)$$

we have:

$$dp_{ac}(t, \vec{r}_1, \vec{r}_3) = r_{ac}(t) * h_{rev,ac}(\vec{r}_1, \vec{r}_3, t) * \frac{1}{2c_a^3} \frac{\partial^3}{\partial t^3} \sigma(\vec{r}_1) p(\vec{r}_1, t) dr_1^3 \quad (3.75)$$

**The sum of the electric and acoustic** component hence becomes:

$$\begin{aligned} dp(t, \vec{r}_1, \vec{r}_3) &= \left( r_{el}(t) * h_{rev,el}(\vec{r}_1, \vec{r}_3, t) + r_{ac}(t) * h_{rev,ac}(\vec{r}_3, \vec{r}_1, t) \right) * \frac{1}{2c_a^3} \frac{\partial^3}{\partial t^3} \sigma(\vec{r}_1) p(\vec{r}_1, t) dr_1^3 \\ &= h_{rev}(\vec{r}_1, \vec{r}_3, t) * \frac{1}{2c_a^3} \frac{\partial^3}{\partial t^3} \sigma(\vec{r}_1) p(\vec{r}_1, t) dr_1^3, \end{aligned} \quad (3.76)$$

and analog to the derivation of the first order echo signal in section 3.3.3, for the total reverberation signal received at the electrical port of the transducer we can finally write:

$$\begin{aligned} v_{rev}(t) &= u(t) * \delta'''(t) * \frac{1}{4c_a^6} \iint h_r(\vec{r}_3, t) \sigma(\vec{r}_3) * h_{rev}(\vec{r}_1, \vec{r}_3, t) * \sigma(\vec{r}_1) h_t(\vec{r}_1, t) \, dr_1^3 dr_3^3 \\ &= \hat{u}(t) * \left( r_{ac}(t) * s_{ac}(t) + r_{el}(t) * s_{el}(t) \right) \end{aligned} \quad (3.77)$$

with

$$s_{ac}(t) = \frac{1}{4c_a^6} \cdot \frac{\partial^6}{\partial t^6} \iint h_r(\vec{r}_3, t) \sigma(\vec{r}_3) * h_{rev,ac}(\vec{r}_1, \vec{r}_3, t) * \sigma(\vec{r}_1) h_t(\vec{r}_1, t) \, dr_1^3 dr_3^3 \quad (3.78)$$

and

$$s_{el}(t) = \frac{1}{4c_a^6} \cdot \frac{\partial^6}{\partial t^6} \iint h_r(\vec{r}_3, t) \sigma(\vec{r}_3) * h_{rev,el}(\vec{r}_1, \vec{r}_3, t) * \sigma(\vec{r}_1) h_t(\vec{r}_1, t) \, dr_1^3 dr_3^3 \quad (3.79)$$

Consequently, the total received signal can be written as:

$$v(t) = v_{1^{st}order}(t) + v_{rev}(t) + n_{ac}(t) + n_{el}(t) \quad (3.80)$$

where the first two terms on the right side are derived above and where  $n_{ac}(t)$  and  $n_{el}(t)$  represents other acoustic noise and electronic noise, respectively. Having established the model for transducer reverberations, we tersely state how it is implemented numerically and then test its adequacy with a few experiments.

#### 3.4.4 Reverberation simulation program

The simulation program developed in section 3.3.4 is easily expanded to handle transducer reverberation signals, as well. We have only to discretize the integrals,  $h_{rev,el}(\vec{r}_1, \vec{r}_3, t)$  and  $h_{rev,ac}(\vec{r}_1, \vec{r}_3, t)$ , as additional components. As shown,  $h_{rev,el}(\vec{r}_1, \vec{r}_3, t)$  consists of a convolution of the already known first order beam pattern of the individual elements with themselves. Hence, it only remains to discretize  $h_{rev}(\vec{r}_1, \vec{r}_3, t)$ .

Again, we divide the transducer surface,  $\mathcal{A}$ , into small rectangles,  $\mathcal{A}_i$ , of the size  $d_x \times d_y$  and, using the same approximations as before, we find from equation 3.74:

$$\begin{aligned}
h_{rev,ac}(\vec{r}_1, \vec{r}_3, t) &\approx \sum_{i=1}^{N_s} \vec{e}_{32i} \vec{n}_{Ai} \frac{\delta(t - \frac{|\vec{r}_1 - \vec{r}_{2i}|}{c})}{2\pi |\vec{r}_1 - \vec{r}_{2i}|} * \frac{\delta(t - \frac{|\vec{r}_3 - \vec{r}_{2i}|}{c})}{2\pi |\vec{r}_3 - \vec{r}_{2i}|} \\
&\quad * \int_{\mathcal{A}_i} \delta(t - \frac{\vec{r}_i(\vec{e}_{12i} + \vec{e}_{32i})}{c}) dr_i^2 \\
&= \sum_{i=1}^{N_s} \vec{e}_{32i} \vec{n}_{Ai} \frac{\delta(t - \frac{|\vec{r}_1 - \vec{r}_{2i}|}{c})}{2\pi |\vec{r}_1 - \vec{r}_{2i}|} * \frac{\delta(t - \frac{|\vec{r}_3 - \vec{r}_{2i}|}{c})}{2\pi |\vec{r}_3 - \vec{r}_{2i}|} \\
&\quad * \frac{d_x}{T_{rev,x}} \frac{d_y}{T_{rev,y}} \text{rect}\left(\frac{t}{T_{rev,x}}\right) * \text{rect}\left(\frac{t}{T_{rev,y}}\right) \quad (3.81)
\end{aligned}$$

where:

$$T_{rev,x} = \frac{d_x}{c} \vec{e}_x \left( \frac{\vec{r}_{12i}}{r_{12i}} + \frac{\vec{r}_{32i}}{r_{32i}} \right), \quad T_{rev,y} = \frac{d_y}{c} \vec{e}_y \left( \frac{\vec{r}_{12i}}{r_{12i}} + \frac{\vec{r}_{32i}}{r_{32i}} \right). \quad (3.82)$$

Having discrete forms of  $h_t(\vec{r}_1, t)$ ,  $h_r(\vec{r}_3, t)$ ,  $h_{rev}(\vec{r}_1, \vec{r}_3, t)$ , we have to sum twice over the scatterer distribution,  $\sigma(\vec{r})$ , and convolve the result with the RF-pulse to get the reverberation signal.

#### Remark on the calculation overhead

We have already indicated that the simulations can be very time consuming. This is especially true when calculating reverberation signals. To generate a first order echo signal we need to calculate  $2 \times N_s \times M_1$  trapezoid functions and perform  $M_1$  convolutions, where  $N_s$  is the number of simulation elements the transducer surface is divided into, and  $M_1$  the number of points representing the target surface. The factor 2 enters when we have different focus settings for the transmit and the receive signal. Correspondingly, we need to calculate  $2N_s \times M_1 + M_1 \times N_s \times M_2 + 2N_s \times M_2$  trapez functions and perform  $M_1 \times M_2 + N \times M_1 \times M_2$  convolutions to get the reverberation signal where  $M_1$ ,  $M_2$  is the number of points representing the first and second target and  $N$  is the number of transducer array elements. We are hence restricted to simulate targets with small diameters, which can be represented by a few points, in order to get acceptable response times from our computer.

#### 3.4.5 Experimental validation

The extension of our model to also include transducer reverberations is straightforward so the simulation model ought to correspond well with experiments. However, confirming this, was not without problems.

First, from the previous section, it is clear that we should use small scatterers, ideally point targets in the validation experiments. Doing so, however, leads to weak reverberation signals due to diffraction of the scattered ultrasound echo pulse. This, then requires strong reflectivity of the point target in order to get an acceptable signal to noise ratio. It turned out that using a tiny metal sphere (e.g. the ball of a pen), which has a reflectivity close to  $R_{metal} \approx 1$  was impractical because of signals from ringing ultrasound within the sphere and creeping surface waves overlaid on the reverberation signal.

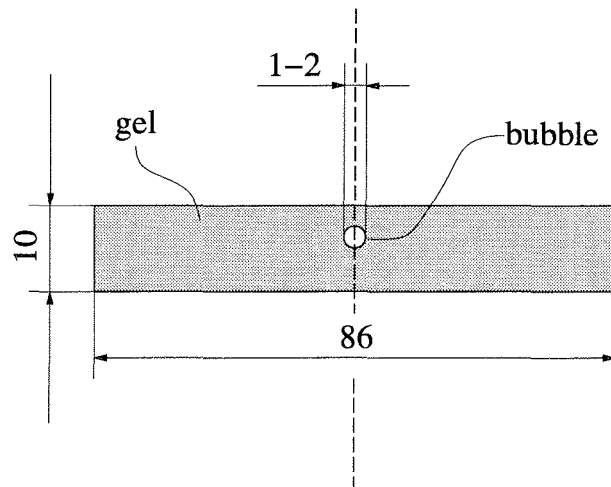


Figure 3.27: Sketch of an air bubble fixed in an agarose gel. The bubble is injected into the gel a short moment before the gel stiffens.

However, as is known, gas bubbles are strong scatterers, too (ultrasound contrast agents make use of this fact). We managed to stabilize, at least for some hours, a single air bubble with a diameter of 1mm–2mm in an agarose gel (see sketch in figure 3.27). It served as a point target to experimentally examine the profile of the reverberation beam. We did not observe any creeping wave effects or any ringing ultrasound in the received echo signal. We used just one bubble as a target and looked at the reverberation echoes traveling from the transducer to the bubble, back to the transducer, and, once more, to the bubble and back to the transducer.

For this experiment, it was important that the bubble was not located directly in the middle of the gel. Otherwise, a multiple echo traveling between the front surface of the

gel, the transducer and the back surface of the gel, would occur simultaneously with the reverberation echo of the bubble and thus distort the signal.

### 3.4.6 Testing and remodeling

In figure 3.28, the measured and simulated beam profiles are shown for the case where the bubble is scanned along the center axis of the transducer from a range of 20mm to 80mm. Figure 3.29 show the corresponding off-axis scans (perpendicular to the center axis) at the range 75mm and 40mm.

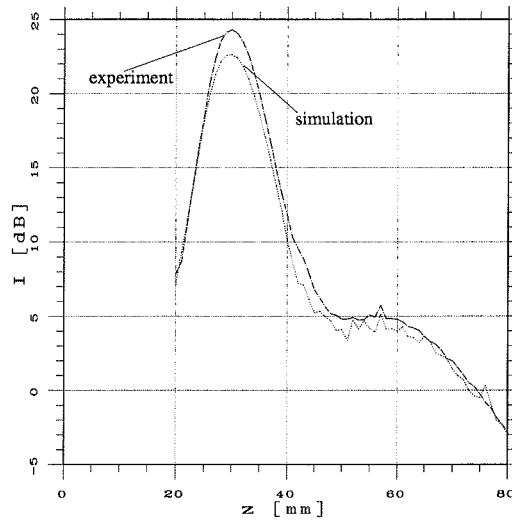


Figure 3.28: On-axis reverberation beam profile. The intensity (RMS value) of the received pulses is plotted versus the target range.

We see from the plots that there is good correspondence between experiment and simulation in the far field region. However, in the near field, the deviations exceed a 1dB limit which we consider as acceptable tolerance. One may ascribe this deviation to near field problems which are due the approximations in the model. However, from the beam profile of the first order echo, figure 3.17, we saw that our model is accurate enough as close as to a range of 10mm–20mm. The deviation must therefore have other reasons. After further experiments, scanning the reverberation beam with various receiver impedances or shorting the outer element, we were convinced that the deviations could be ascribed to the reflected

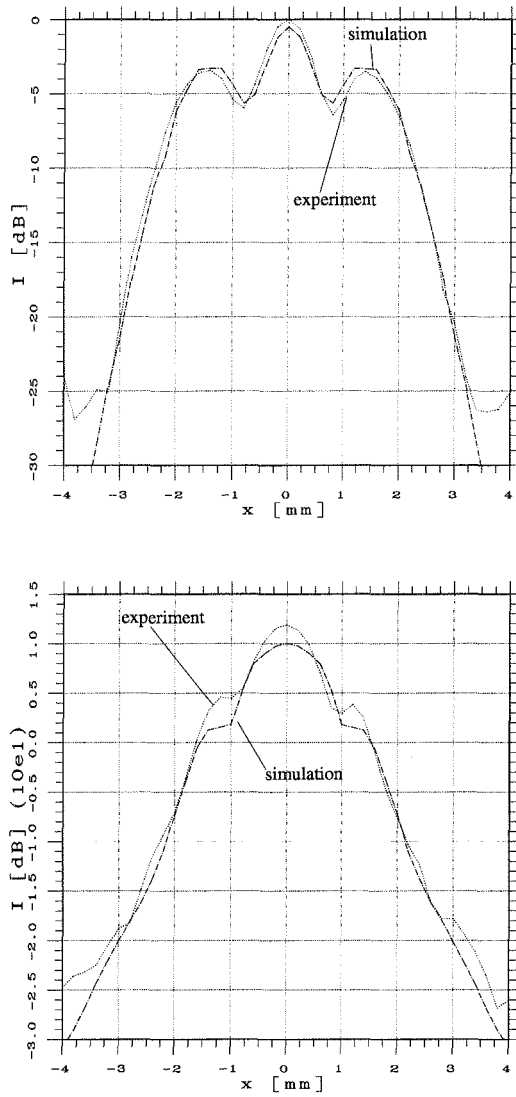


Figure 3.29: Off-axis reverberation beam profile at a range of 75mm (top) and 40mm (bottom). The intensity of the received pulses is plotted versus the offset of the target from the center axis.

echo from the kerf of the transducer separating the two elements. The kerf has other acoustic properties than the elements because it contains only epoxy filling and no piezoelectric ceramic. Additionally, inspecting the transducer surface more accurately, we saw that the kerf was not filled totally. A slight groove remained on the transducer surface (see figure 3.30). This will delay the reflected kerf pulse slightly and result in a phase difference. However, we had no means of getting an exact curvature of the transducer surface to be able to perform more accurate simulations. Nor, did we know the exact form of the kerf pulse. It might be possible to measure the kerf pulse with a laser scanning system, as described in [35], but we had no access to such a system.

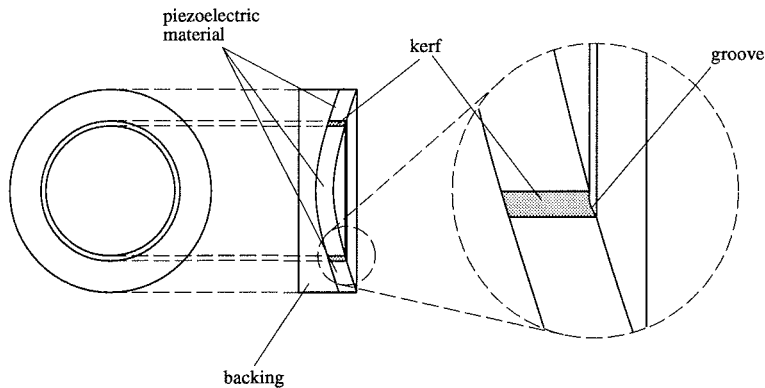


Figure 3.30: Detail drawing of the transducer kerf.

In order to demonstrate that the kerf may be the reason for the observed deviations, we used the measured electric reverberation pulse as kerf pulse and delayed it slightly. Figures 3.31–3.33 show the beam profiles for the same three cases as above. We see that the maximum deviation is now around 1dB for the on-axis scan.

For the 40mm off-axis scan the deviation at the side-lobes still exceeds 1dB. Their level seems not to be influenced by the kerf pulse at all. Even with the tuning of other model parameters we did not manage to get a better match. Reasons for this may be, apart from the ignorance of the exact kerf pulse, variations in the transducer shape and material parameters.

However, we feel that we have demonstrated a good accordance between our simulation model and reality. We can thus rely on simulations for the further examination of transducer

reverberations and the development of reduction algorithms. This is important because we had no access to suitable RF-data from a 1D phased array to verify our further findings experimentally. Moreover, we are able to investigate the benefit of 1.5D or even 2D arrays which are not available at this time.

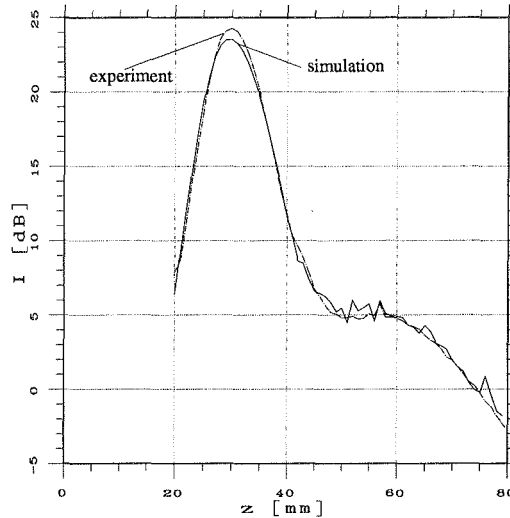


Figure 3.31: On-axis reverberation beam profile where the effect of the kerf is included. The intensity of the received pulses is plotted versus the target range.

### 3.5 1D signal model

It is often convenient to reduce the 3D model to one dimension. This can be done assuming that the ultrasound beam is narrow in comparison to the lateral correlation lengths in the medium. A narrow beam is obtained with dynamic focusing as illustrated in Chapter 2. Further, specular targets have rather long lateral correlation lengths resulting in high reflectivity. Specular targets thus give the strongest echoes; correspondingly, reverberations between these specular targets and the transducer will dominate in the reverberation noise, too.

Assuming that the ultrasound beam is infinitesimally thin, or, equivalently, that the target distribution has constant acoustic properties over the beam width, we can integrate over the lateral dimensions in equations 3.41 and 3.77 and for equation 3.80 get:

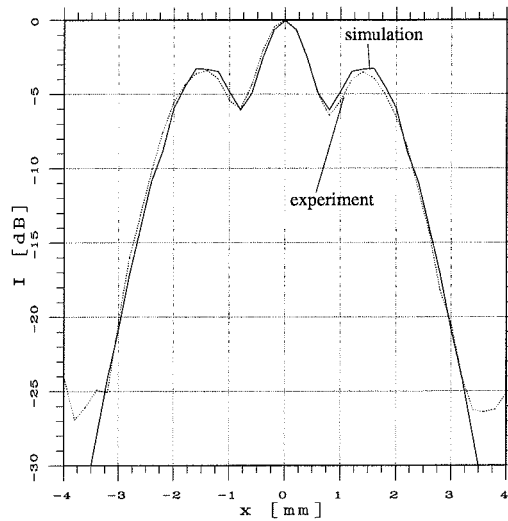


Figure 3.32: Off-axis reverberation beam profile at a range of 75mm. The intensity of the received pulses is shown versus the offset of the target from the center axis.

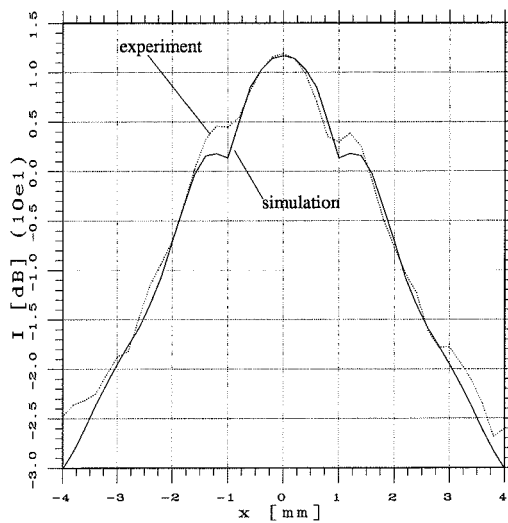


Figure 3.33: Off-axis reverberation beam profile at a range of 40mm. The intensity of the received pulses is plotted versus the offset of the target from the center axis.

$$\begin{aligned}
v(t) = & u(t) * \frac{1}{2c_a^3} \int h_r(r_1, t) * h_t(r_1, t) \cdot \sigma(r_1) dr_1 \\
& + u(t) * \frac{1}{4c_a^6} * \delta'''(t) \\
& * \int \int h_r(r_1, t) * h_t(r_3, t) * h_{rev}(r_1, r_3, t) \cdot \sigma(r_1) \cdot \sigma(r_3) dr_1 dr_3 . \quad (3.83)
\end{aligned}$$

Inspecting the term  $h_r(r, t)$ , in more detail, we see that:

$$\begin{aligned}
h_t(r, t) &= \int \frac{\delta(t - \frac{|r\vec{e}_z - \vec{r}_0|}{c})}{2\pi|r\vec{e}_z - \vec{r}_0|} dr_0^2 \\
&= \delta(t - \frac{r}{c}) * \int \frac{\delta(t - \frac{|r\vec{e}_z - \vec{r}_0| - r}{c})}{2\pi|r\vec{e}_z - \vec{r}_0|} dr_0^2 \\
&= \delta(t - \frac{r}{c}) * f_t(t, r) \quad (3.84)
\end{aligned}$$

Correspondingly, we can write:

$$h_r(r, t) = \delta(t - \frac{r}{c}) * f_r(t, r) \quad (3.85)$$

and

$$h_{rev}(r_1, r_3, t) = \delta(t - \frac{r_1}{c}) * \delta(t - \frac{r_3}{c}) * f_{rev}(t, r_1, r_3) \quad (3.86)$$

Further, combining  $f_t(t, r)$  and  $f_r(t, r)$  as well as  $f_t(t, r_1)$ ,  $f_r(t, r_3)$  and  $f_{rev}(t, r_1, r_3)$ , as follows:

$$\begin{aligned}
f_{1^{st}order}(t, r) &= f_t(t, r) * f_r(t, r) \\
f_{revecho}(t, r_1, r_3) &= f_t(t, r_1) * f_{rev}(t, r_1, r_3) * f_r(t, r_3) ,
\end{aligned}$$

we can finally write:

$$\begin{aligned}
v(t) = & u(t) * \frac{1}{2c_a^3} \int \delta(t - \frac{2r_1}{c}) * f_{1^{st}order}(t, r_1) \cdot \sigma(r_1) dr_1 \\
& + u(t) * \delta'''(t) * \frac{1}{4c_a^6} \int \int \delta(t - \frac{2r_1}{c}) * \delta(t - \frac{2r_3}{c}) * f_{revecho}(t, r_1, r_3) \cdot \sigma(r_1) \cdot \sigma(r_3) dr_1 dr_3 . \quad (3.87)
\end{aligned}$$

This is the 1D formulation of the signal model that we will use in Chapter 5.

### 3.6 Summary and discussion

In this chapter, we derived a model describing the signals in an ultrasound scanner system from the excitation pulse at the electrical port of the transducer to the RF-signal which is received as the output of the beam former.

The model was decomposed into four main parts:

- A model describing the transducer transfer functions based on the 1D KLM model.
- A first order description (Born approximation) of pulse propagation in a linear acoustic medium.
- A model describing the reflection factor of the transducer.
- A description of the propagation pattern of pulses reflected at the transducer surface.

An important new finding was that the transducer reflection factor consists of an acoustic and electric component, each of which is accompanied by its own pulse propagation pattern.

Furthermore, we demonstrated the accuracy of a numerical implementation of the model with several water-tank experiments. It is thus valid to use simulations when studying further properties of the reverberation echoes. This has the advantage that we can switch on and off other noise effects or focus on special effects of multiple scattering. Further, it allows us to investigate 1D transducer arrays, which we had no RF-signal access to, or 1.5D, or even 2D, transducer arrays, which are not yet available on the market.

The main shortcoming of our model is that it neglects frequency dependent attenuation when the ultrasound pulse propagates through the medium. The main reason for this simplification was to save computation time by dropping a further convolution with a range-dependent loss function. However, we feel that this simplification has no significant influence on the results of our further work.

Finally, we introduced a simplified one-dimensional model interpreting the ultrasound beam as a thin ray. This model will be used for sake of simplicity when it is appropriate in developing new reduction algorithms.



## Chapter 4

# Reduction of stationary reverberations

In this chapter, we address the problem of stationary reverberations in cardiac imaging. In some cases, stationary reverberations overlay visibly<sup>1</sup> on the first order image of the cardiac apex. They are due to the strong reflecting fatty tissue interfaces under the skin. The transmitted ultrasound pulse bounces back and forth between these tissue interfaces or between them and the transducer surface. Because the transducer and the tissue interfaces are not moving<sup>2</sup>, in contrast to the heart, these reverberations show up as a stationary fog in the apex region, see figure 4.1. The effect is not clearly visible inspecting a single frame of an image sequence (figure 4.2), but, when animating a whole sequence in order to study the mobility of the apex region, the artifact can be annoying.

To remove these stationary reverberations, a highpass filtering scheme along time suggests itself. Filtering along time in this context means to process single pixels from frame to frame. We will study the design of such a filter in the following.

### 4.1 Filter design

Filter design commonly consists of three steps[36]. First, the specifications that the filter should meet are established. Then, an error function and an appropriate norm to minimize this error function has to be found. Here, one may also have to consider additional side

---

<sup>1</sup>In other cases they are still there but do not appear that pronounced.

<sup>2</sup>A mechanical scanned transducer moves, of course, when rotated over the image sector. But looking at single pixels from frame to frame the transducer is supposed to be in the same position.

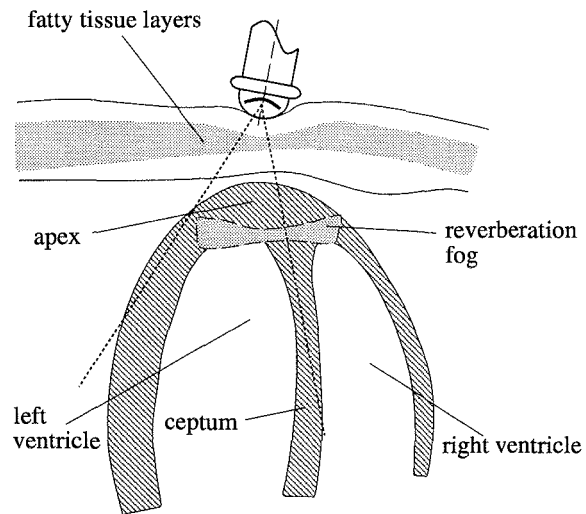


Figure 4.1: Illustration of stationary reverberations in cardiac imaging due to the body wall.

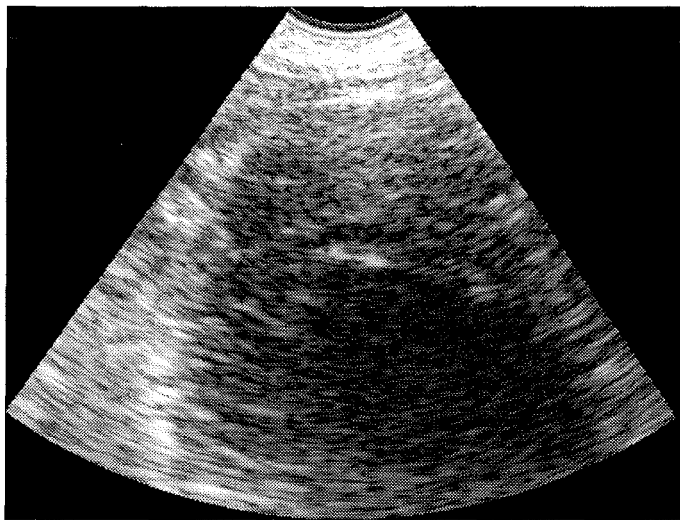


Figure 4.2: Example where stationary reverberations overlay on the apex region. Without animation they are, however, hardly visible.

constraints. Finally, the filter has to be realized, if possible. If not, the specifications must be modified.

#### 4.1.1 Filter specifications

For our purposes, the reverberation reduction filter should:

- remove the reverberations
- not distort first order signals significantly

In order to establish more detailed filter specifications, we must analyze the properties of the different signal types encountered in ultrasound imaging of the heart.

#### Time/frequency dependence of the signals

While imaging the hearts of two volunteers using a mechanically scanning probe, we acquired several 2D sector sequences. The frame rate was approximately  $30 \frac{\text{frames}}{\text{s}}$ , changing slightly with the size of the image sector; the sequences consisted of 35 frames (about one cardiac cycle). The analog RF-data were digitized at a rate of 10MHz using 12bit per sample. Consecutively, the signals were demodulated beam for beam with a mixing frequency of 3.25MHz, which corresponded to the nominal center frequency of the transducer.

From visual examination of the B-mode sequences, we determined several pixels<sup>3</sup> belonging to one of the groups:

- stationary tissue layer
- stationary reverberation
- moving heart wall
- combination of stationary reverberation and moving heart wall

Typical examples of these signal groups and their corresponding Fourier transforms are plotted in figures 4.3–4.10. The frequency spectra are plotted versus normalized frequency where the value 1 corresponds to the frame rate of the sequence.

---

<sup>3</sup>To be clear, a pixel corresponds to a point with a constant beam angle and range. The change in the grey value at this location from frame to frame thus makes up the 1D pixel signal.

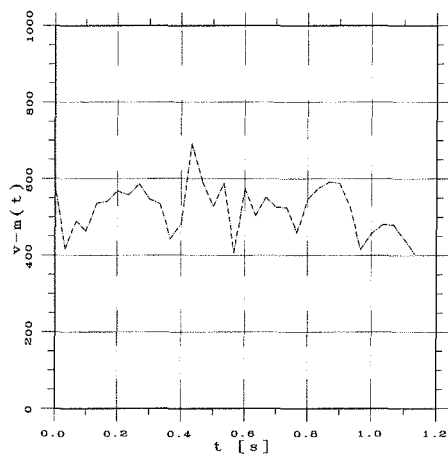


Figure 4.3: Stationary reverberation signal. The magnitude of the analytical signal is plotted versus time.

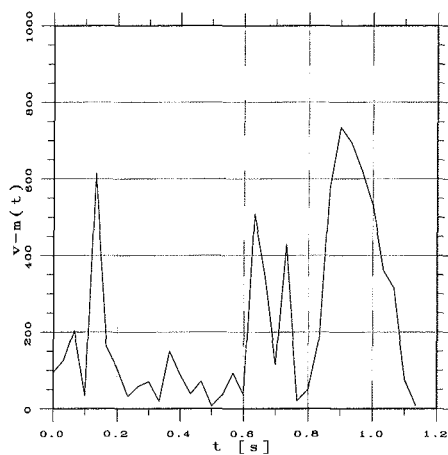


Figure 4.4: Moving wall signal. The magnitude of the analytical signal is plotted versus time.

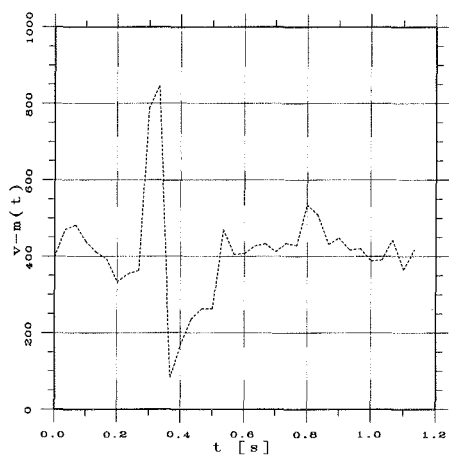


Figure 4.5: A combination of a stationary reverberation and the moving wall. The magnitude of the analytical signal is plotted versus time.

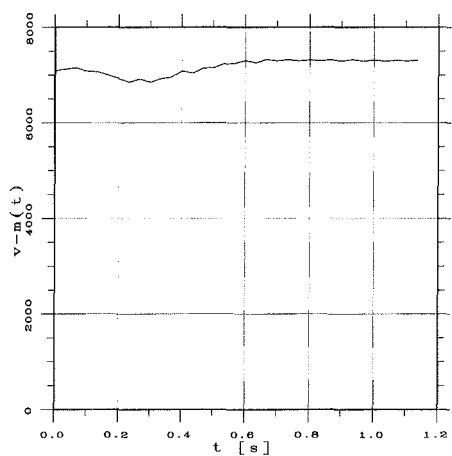


Figure 4.6: Stationary signal from fatty tissue. The magnitude of the analytical signal is plotted versus time. Note the different scale at the ordinate.

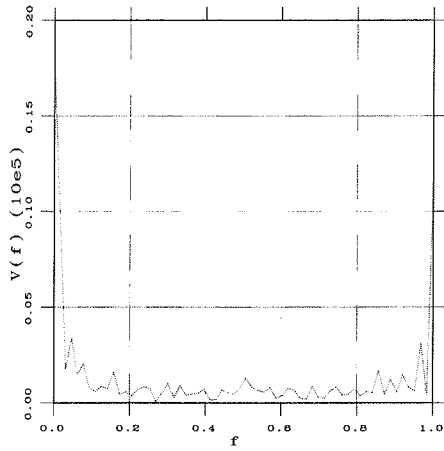


Figure 4.7: FFT of the stationary reverberation signal. The magnitude is plotted versus normalized frequency.

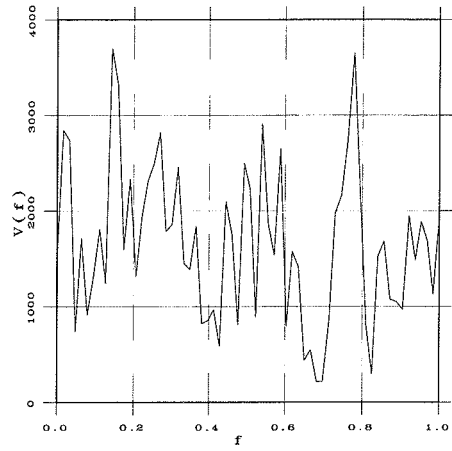


Figure 4.8: FFT of the moving wall signal. The magnitude is plotted versus normalized frequency.

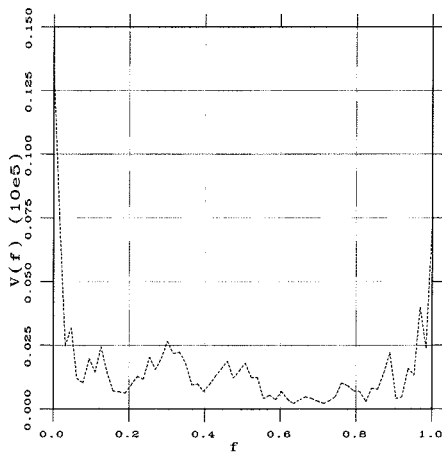


Figure 4.9: FFT of the combination of a stationary reverberation and a moving wall signal. The magnitude is plotted versus normalized frequency.

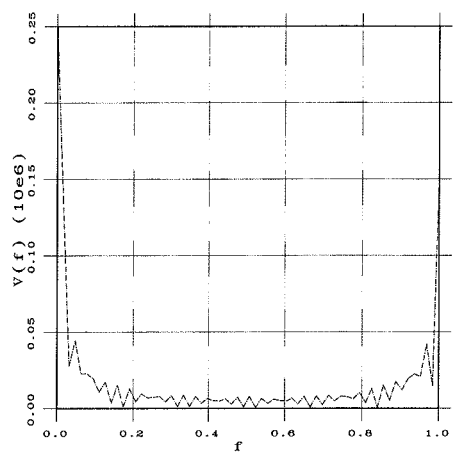


Figure 4.10: FFT of the stationary signal from fatty tissue. The magnitude is plotted versus normalized frequency.

We clearly see the peak around zero frequency for those signal types having a stationary component. Furthermore, we can specify from this that a cut-off frequency of  $f_c = 0.1$  seems to be appropriate in order to remove the stationary components in the signals. To use a stop band from 0 to 0.1 rather than removing just the component at zero frequency reflects the fact that the *stationary* signals are not strictly stationary. Reasons for this are slight movements of the ultrasound probe due to the operator or respiration of the patient.

#### 4.1.2 Error function, norm and side constraints

Before trying to find an appropriate error function and norm, let us look at some side constraints. Even if stationary reverberations are definitely annoying in some cases, a reduction filter operating off-line will not be accepted. Yet, for reasons of cost-efficiency, the real time hardware of an ultrasound scanner system will have a limited memory capacity inhibiting to buffer up a large number of frames. This means that we are restricted to use a low filter order,

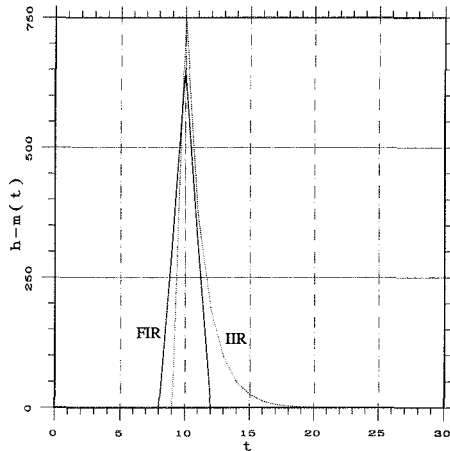


Figure 4.11: Magnitude data of a highpass filtered Dirac pulse. The highpass filters are of FIR and IIR type with equal order. The IIR filter is superior to the FIR filter in terms of the RMS value of the error signal.

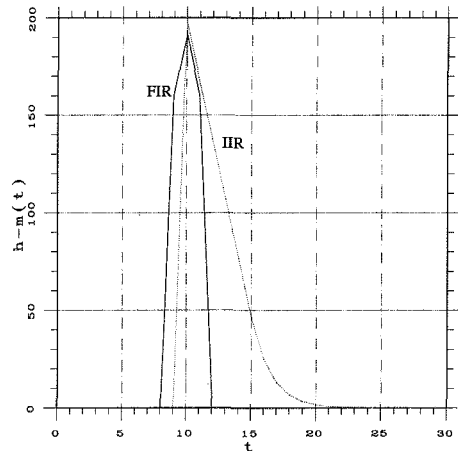


Figure 4.12: Compressed amplitude data of a highpass filtered Dirac pulse. The highpass filters are of FIR and IIR type with equal order. The IIR filter is inferior to the FIR filter in terms of the RMS value of the error signal.

$P$  i.e.  $P \leq 4$ . This fact favors IIR filters, which in theory can achieve steeper transition

bands than can FIR filters with the same filter order. But, IIR filters have a nonlinear phase behavior, which may cause undesired artifacts.

Another aspect calling for low filter order is grey-scale compression. As mentioned in Chapter 2, B-mode signals are commonly compressed by a nonlinear function  $\mathcal{C}\{\cdot\}$  to fit their dynamic range into the perceptive range of the human observer. Now, if a pixel signal includes a sudden event, e.g. the heart wall is passing the pixel for only one time sample, the filter impulse response will be imaged. Since weak signals are amplified more than strong ones through compression, the low-valued coefficients of the filter response will be emphasized leading to a prolonged filter response. This effect is demonstrated in figures 4.11 and 4.12. We see that an IIR filter with its infinitely long impulse response suffers more from this than does a FIR filter. Even though the IIR response is slightly shorter<sup>4</sup> in a linear scale, it exceeds the duration of the FIR signal after nonlinear compression resulting in an increased blurring of the signal event.

We applied a two-step approach to determine the optimal filter. First, we used classic design methods to get filters that match the given frequency specifications (lowpass cut-off frequency at 0.1) as best as possible. The FIR filter coefficients were calculated minimizing the error between the frequency response of the filter and the specified stop and pass band where the bands could be weighted differently. The transition band was a “don’t care”<sup>5</sup> region. The error was minimized applying the Euclidean norm  $L_2\{err(f)\} = \|err(f)\|_2 = \sqrt{\int |err(f)|^2 dt}$ .

The IIR filters were all Butterworth filters specified by the filter order and the  $-3\text{dB}$  cut-off frequency. Their coefficients were also calculated by minimizing the Euclidean norm of the error in the frequency domain. The magnitudes of the frequency response of the calculated filters are plotted in figure 4.13. The exact design parameters and the filter coefficients are given in Appendix B.

The second step consisted of selecting from the filters of the first step the one that minimized the following nonlinear criterion:

$$J = \frac{\|d_{mw}(t)\|_2 / \|\mathcal{C}\{v_{mw}(t)\}\|_2}{\|d_{rev}(t)\|_2 / \|\mathcal{C}\{v_{rev}(t) * h(t)\}\|_2} \quad (4.1)$$

where  $d_i(t) = \mathcal{C}\{v_i(t)\} - \mathcal{C}\{v_i(t) * h(t)\}$ ,  $i = mw, rev$ . Here,  $v_{mw}(t)$  and  $v_{rev}(t)$  are typical

<sup>4</sup>The length of the signal is defined here as the duration the signal exceeds the  $-6\text{dB}$  level relative to its maximum.

<sup>5</sup>“Don’t care” means that zero weight is assigned to this region.

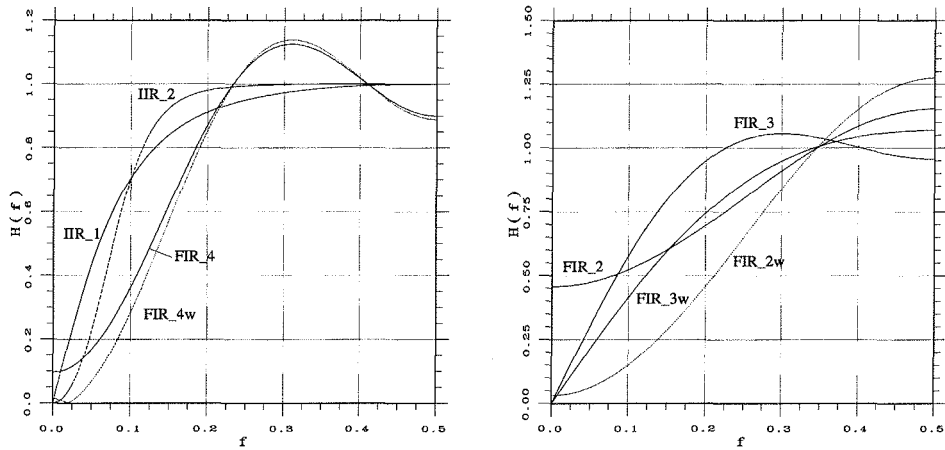


Figure 4.13: Magnitude of the frequency responses of the designed filters.

examples from the moving wall and reverberation signal group, respectively. The applied criterion is motivated by the following reasoning: As pointed out, the image sequence is displayed after amplitude compression. Hence, it seems natural to assess the error after this process. Furthermore, from the specifications we understand that the moving wall signals should not be affected. The error introduced in the moving wall signal should be minimized, thus it enters in the numerator of the expression. On the other hand, the stationary reverberation signal should be reduced. Consequently, the difference between the unprocessed and the processed signal should be a maximum. It enters therefore in the denominator. Finally, we have to normalize the differences to the strength of the ‘ideal’ signals, which are the moving wall signal before and the reverberation signal after filtering, to get an equal weighting of both contributions.

It is clear that the outcome of the criterion is dependent on the choice of the typical signals. Consequently, we can make a reliable decision whether one filter outperforms the other, only when there is a significant difference in the criterion value. Ultimately, one has to assess the processing result visually because mathematical criteria hardly can be adapted to all aspects of human perception.

## 4.2 Optimum filter and performance test

filter	$J$
fir2	0.64
fir2w	0.18
fir3	0.21
fir3w	0.18
fir4	0.21
fir4w	0.15
iir1	0.17
iir2	0.21

Table 4.1: Compiled error criterion values for the designed filters.

The calculated criterion values for the different filters are given in Table 4.2. From this we see that the weighted fourth order FIR filter performs best. However, the first order IIR and weighted second order FIR filter perform quite well, too, and have the advantage of lower memory demand.

The filtering results for these three optimal filters operating on the signal with a combination of the moving wall and a reverberation (figure 4.5) are shown after amplitude compression in figures 4.14–4.16. (The processing results operating on the other typical signals are given in Appendix B.)

We see that the stationary signal part is reduced efficiently while the characteristic dynamic features of the signals are preserved. Inspecting the plots, we find similar filter performance, which was already indicated by the criterion values. Hence, we recommend a first order IIR highpass filter in the case when the frame buffer has to be minimized (we indeed need only to store the last input frame in addition because the output frame is available anyway) otherwise a weighted fourth order FIR filter.

Next, we applied the filters on a whole image sequence and inspected the results which proved to be satisfying (see also figure 4.17). As above, no significant difference was observed between the three filters in this visual test.

The highpass filter naturally also reduces the strength of the stationary signal of the fatty tissue under the skin. But this is no serious problem because it is the functionality of the heart that stands in the focus of the observer. In fact, the strong signals near to the transducer are commonly attenuated by the operator adjusting the depth gain compensation on the scanner.

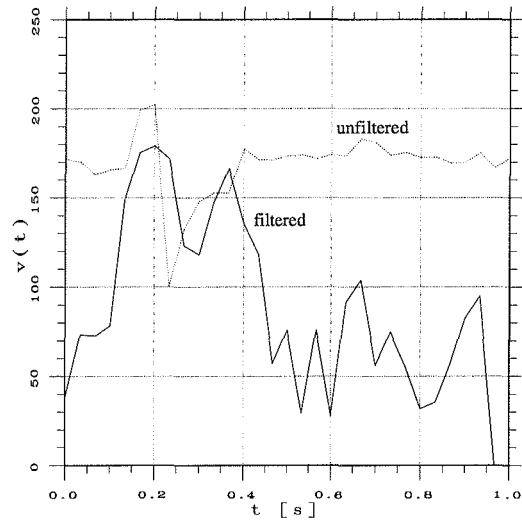


Figure 4.14: Combination signal before and after filtering with the weighted fourth order FIR filter. The compressed magnitude of the analytical signal is plotted versus time.

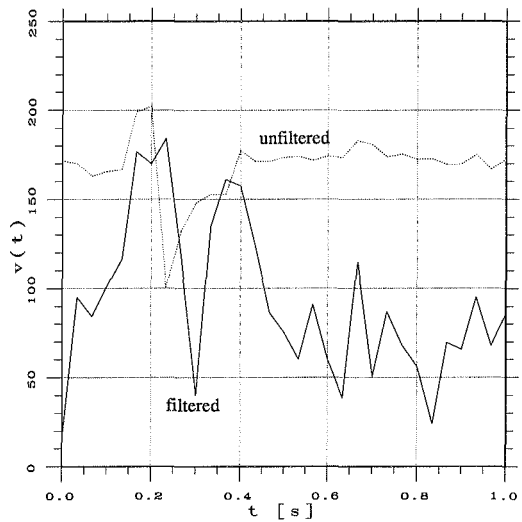


Figure 4.15: Combination signal before and after filtering with the first order IIR filter. The compressed magnitude of the analytical signal is plotted versus time.

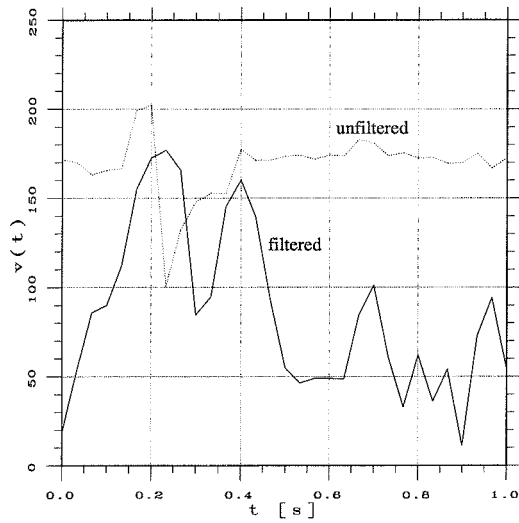


Figure 4.16: Combination signal before and after filtering with the weighted second order FIR filter. The compressed magnitude of the analytical signal is plotted versus time.

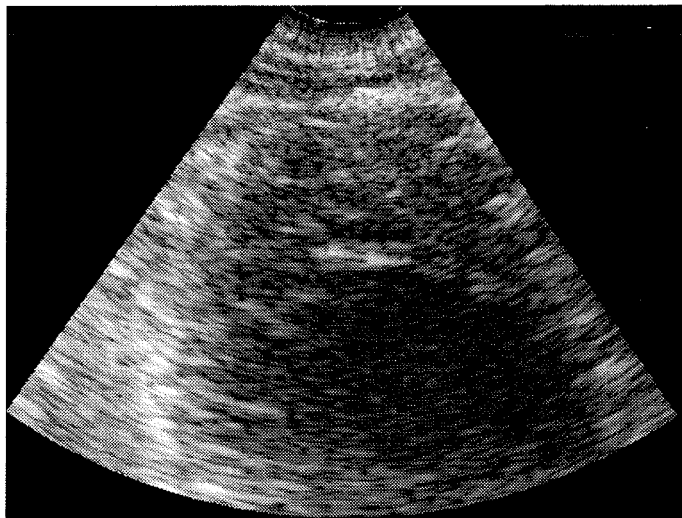


Figure 4.17: The same frame as in figure 4.2 after processing with the weighted fourth order FIR filter. The improvement is more easily discernible when the sequence is animated.

However, when this part is filtered, fluctuating noise becomes apparent. We think that this is due to a problem with the mechanical scanning.

### 4.3 Left right scan problem

The beam positions for left and right scans do not match exactly (see figure 4.18) and the stationary signal will thus vary slightly for consecutive frames. But presuming the probe is not moved the signal will be constant for each second frame. This behavior is, in fact, observed inspecting figure 4.19 showing the magnitude of the stationary fat signal before amplitude compression.

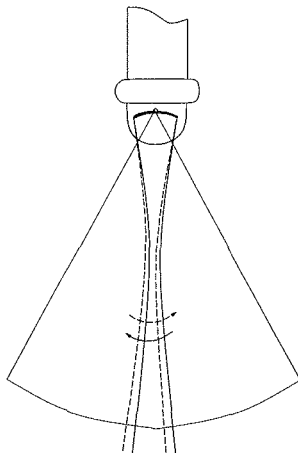


Figure 4.18: Position mismatch when sweeping the beam left and right.

In order to minimize this mismatch it is possible to tune the scanning so the beams coincide as well as possible. This was also done in our case, but we could not completely compensate for the effect. The remaining deviation is not visible when displaying the unfiltered sequence because the signal changes are weak compared to the absolute signal amplitude that lies in the saturated part of the compression function. However, when applying a highpass filter along time, the strong stationary signal part is removed and the fluctuations become apparent. As an ad hoc solution, we suggest a lateral second order median filter to smooth the filtered time signals before amplitude compression. However, we did not investigate this problem thoroughly and other filters may perform better. The reason

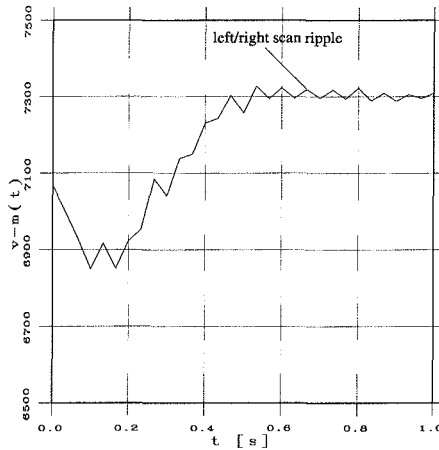


Figure 4.19: Ripple noise on the stationary signal due to the position mismatch when the beam is swept left/right. Note the scale at the ordinate. (There is an additional probe movement in the first 400ms).

for neglecting this noise artifact is that it is typical for mechanical scanning. Electronically phased arrays with a precisely steered ultrasound beam will not suffer from this artifact. Unfortunately, we could not test the performance of our filter on such a system, because we had no access to the tissue RF-data.

#### 4.4 Other processing domains

The filtering in the scheme presented above is performed directly on each component (real and imaginary part) of the analytical signal,  $\hat{v}(t)$ , which is equivalent to processing the raw RF-data. On the other hand, it would be possible to process only the amplitude images,  $v_m(t)$ , or even the compressed images,  $v_{gr}(t)$ . In this case we could use higher filter orders because dropping the phase component frees memory to buffer frames.

One problem, then, is that we no longer have linear signals and, hence, it is not possible to say exactly what we are removing. Further, when the phase information is dropped the time signals become more low frequent. This becomes apparent in figure 4.20 where we show the Fourier transform of the magnitude of the moving wall signal and the stationary reverberation signal. In both signals, we find a significant part of the signal energy around zero frequency which, when removed, changes the signal features significantly.

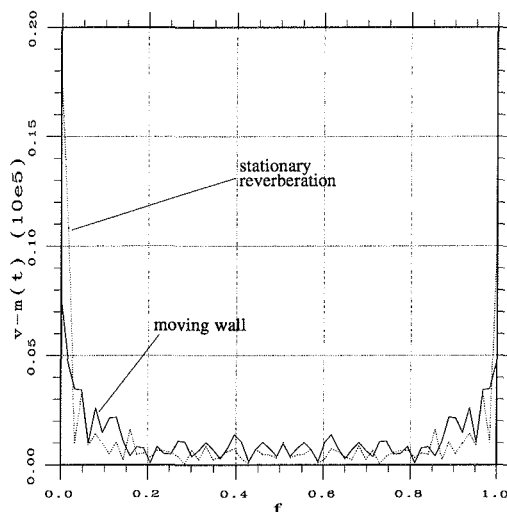


Figure 4.20: Fourier transform of the magnitude representation of the typical time signals 'moving wall' and 'stationary reverberation'.

The filter scheme devised in this chapter is thus an example where it is mandatory to process in the RF-signal domain or, equivalently, in the analytical signal domain.

## 4.5 Summary and discussion

In this chapter, we presented a simple filtering scheme operating in the analytical signal domain that reduced the effect of stationary reverberations overlaying on the echo signals of the moving heart. The dynamic features of the signals are retained while stationary components are significantly reduced. Low filter order as a side constraint enables us to implement the scheme as a real time application. The choice of the optimal filter(s) was based on comparing standard design FIR and IIR filters using a reasonable criterion. However, other filter types e.g. nonlinear or time-variant filters may prove to perform better. The main reason for not investigating the optimal filter question more thoroughly was that we waited to get access to RF-data from a digital scanner using phased arrays which would also solve the left/right scan problem and other signal synchronization problems we had with the RF-unit of the analog scanner.

There is the danger (though we did not find evidence for it in our sequences) that parts

of the heart wall can be attenuated during end diastoly when the heart is moving very slowly. For those cases, an adaptive scheme that classifies regions of reverberations and executes the highpass filtering only on these regions, may perform better. It would also avoid any blurring of pure *moving wall* signals. The author of [37] looked into the design of such an adaptive approach, but it remains to be tested whether the adaptive scheme clearly outperforms our simple approach and thus justifies the higher complexity.



## Chapter 5

# Reverberation reduction by transducer displacement

In the previous chapter, we used the temporal characteristics of the ultrasound signals to discriminate between the first order echoes and stationary reverberations. By that approach, both transducer reverberations and internal reverberations were reduced.

In the approach we present in the following, only reverberations produced by a reflection at the transducer surface are addressed. Further, we assume this time that there are no moving targets in the scanned object. The reverberation reduction scheme makes use of the fact that the propagation paths for the first order echoes and the reverberations echoes are different. The idea is to vary the propagation lag between the transducer and the targets. This can be done, for example, by displacing the transducer a small distance,  $\Delta r$ , as illustrated in figure 5.1. The first order echoes will thus experience a difference in the propagation time lag of  $\Delta T_{1^{st}order} = 2\Delta r/c$ , whereas the reverberation echoes will be shifted in time by  $\Delta T_{rev} = 4\Delta r/c$ . The consecutive filter algorithm combines these two RF-echo signals from the same beam direction.

To be more concrete, we will proceed with the formulation of the signal model for the problem at hand. Thereafter, we will examine performance limits through theoretical considerations and simulations. Then, we will present the results of experiments where we imaged a phantom in a water tank. Finally, we will look at some realization aspects and end the chapter with a discussion.

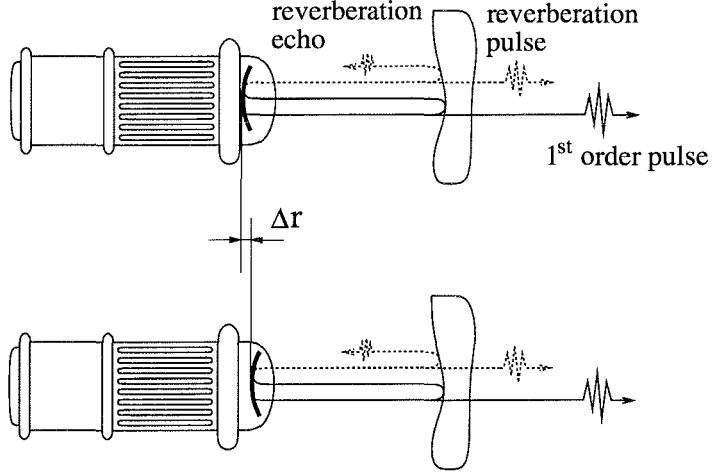


Figure 5.1: Propagation paths for 1<sup>st</sup> order echoes (solid) and reverberation echoes (dotted) for two distances between the transducer and the target.

### 5.1 Signal model

For the sake of simplicity, we will use the 1D signal model introduced in section 3.5. It is appropriate for this case because the essential features of the algorithm can be explained, even if the lateral effects of the beam pattern are neglected. The signal of a first scan line is given by equation 3.87:

$$\begin{aligned}
 v_1(t) = & u(t) * \frac{1}{2c_a^3} \int \delta(t - \frac{2r_1}{c}) * f_{1^{st}order}(t, r_1) \cdot \sigma(r_1) dr_1 \\
 & + u(t) * \delta'''(t) * \frac{1}{4c_a^6} \iint \delta(t - \frac{2r_1}{c}) * \delta(t - \frac{2r_3}{c}) \\
 & \quad * f_{revecho}(t, r_1, r_3) \cdot \sigma(r_1) \cdot \sigma(r_3) dr_1 dr_3 \quad .
 \end{aligned}$$

Next, the transducer is translated a small distance,  $\Delta r$ , in the positive direction along its center axis. This is equivalent to moving the target distribution,  $\sigma(r)$ , towards the transducer. Thus, we can substitute:

$$\sigma(r) \rightsquigarrow \sigma(r + \Delta r) \quad . \tag{5.1}$$

For a realization, it is important to note that the target distribution must not be deformed. This means that the transducer shift should be done, for example, within a fluid filled housing. After translating the transducer, a second acquired scan line signal becomes:

$$\begin{aligned}
v_2(t) &= u(t) * \frac{1}{2c_a^3} \int \delta\left(t - \frac{2r_1}{c}\right) * f_{1^{st}order}(t, r_1) \cdot \sigma(r_1 + \Delta r) dr_1 \\
&\quad + u(t) * \delta'''(t) * \frac{1}{4c_a^6} \iint \delta\left(t - \frac{2r_1}{c}\right) * \delta\left(t - \frac{2r_3}{c}\right) \\
&\quad \quad \quad * f_{revecho}(t, r_1, r_3) \cdot \sigma(r_1 + \Delta r) \cdot \sigma(r_3 + \Delta r) dr_1 dr_3 \\
&= u(t) * \frac{1}{2c_a^3} \int \delta\left(t - \frac{2(r_1 - \Delta r)}{c}\right) * f_{1^{st}order}(t, r_1 - \Delta r) \cdot \sigma(r_1) dr_1 \\
&\quad + u(t) * \delta'''(t) * \frac{1}{4c_a^6} \iint \delta\left(t - \frac{2(r_1 - \Delta r)}{c}\right) * \delta\left(t - \frac{2(r_3 - \Delta r)}{c}\right) \\
&\quad \quad \quad * f_{revecho}(t, r_1 - \Delta r, r_3 - \Delta r) \cdot \sigma(r_1) \cdot \sigma(r_3) dr_1 dr_3 \tag{5.2}
\end{aligned}$$

where we have substituted  $r_1 + \Delta r$  by  $r_1$ ,  $r_3 + \Delta r$  by  $r_3$  to get the last equation. Since  $\Delta r$  is independent of the range, we can extract the convolution factors,  $\delta\left(t + \frac{2\Delta r}{c}\right)$ , out of the integrals and lump them into the RF-pulse,  $u(t)$ :

$$\begin{aligned}
v_2(t) &= u\left(t + \frac{2\Delta r}{c}\right) * \frac{1}{2c_a^3} \int \delta\left(t - \frac{2r_1}{c}\right) * f_{1^{st}order}(t, r_1 - \Delta r) \cdot \sigma(r_1) dr_1 \\
&\quad + u\left(t + \frac{4\Delta r}{c}\right) * \delta'''(t) * \frac{1}{4c_a^6} \iint \delta\left(t - \frac{2r_1}{c}\right) * \delta\left(t - \frac{2r_3}{c}\right) \\
&\quad \quad \quad * f_{revecho}(t, r_1 - \Delta r, r_3 - \Delta r) \cdot \sigma(r_1) \cdot \sigma(r_3) dr_1 dr_3 \tag{5.3}
\end{aligned}$$

The two scan line signals,  $v_1(t)$  and  $v_2(t)$ , are processed in order to reduce reverberations as follows. The signal  $v_{r2}(t)$  is shifted back by  $\Delta T = \frac{4\Delta r}{c}$  thus the reverberation components of the two signals coincide in time. Subsequently, the signals are subtracted, giving:

$$\begin{aligned}
v_p(t) &= v_1(t) - v_2\left(t - \frac{4\Delta r}{c}\right) \\
&= u(t) * \frac{1}{2c_a^3} \int \delta\left(t - \frac{2r_1}{c}\right) * f_{1^{st}order}(t, r_1) \cdot \sigma(r_1) dr_1 \\
&\quad - u\left(t - \frac{2\Delta r}{c}\right) * \frac{1}{2c_a^3} \int \delta\left(t - \frac{2r_1}{c}\right) * f_{1^{st}order}(t, r_1 - \Delta r) \cdot \sigma(r_1) dr_1 \\
&\quad + v_{rev,res}(t) \tag{5.4}
\end{aligned}$$

where the residual reverberation signal is given by:

$$v_{rev,res}(t) = u(t) * \delta'''(t) * \frac{1}{4c_a^6} \iint \delta(t - \frac{2r_1}{c}) * \delta(t - \frac{2r_3}{c}) * \left[ f_{revecho}(t, r_1, r_3) - f_{revecho}(t, r_1 - \Delta r, r_3 - \Delta r) \right] \cdot \sigma(r_1) \cdot \sigma(r_3) dr_1 dr_3 \quad (5.5)$$

As investigated in section 5.4.1, the function,  $f_{revecho}(t, r_1, r_3)$ , is rather smooth. Consequently, we get:

$$f_{revecho}(t, r_1, r_3) \approx f_{revecho}(t, r_1 - \Delta r, r_3 - \Delta r) \quad (5.6)$$

for small  $\Delta r$  and hence  $v_{rev,res}(t)$  becomes very small.

On the other hand, the remaining first order signal component should be as similar as possible to the original first order echo signal. This depends on the choice of  $\Delta r$ . Therefore, we will examine next which value we should assign to the transducer displacement.

## 5.2 The optimal choice of $\Delta r$

Neglecting the residual reverberation signal and approximating  $f_{1^{st}ord}(t, r_1) \approx f_{1^{st}ord}(t, r_1 - \Delta r)$ <sup>1</sup>, for the processed first order signal we get:

$$v_{p,1^{st}order}(t) = \left[ u(t) - u\left(t - \frac{2\Delta r}{c}\right) \right] * \frac{1}{2c_a^3} \int \delta\left(t - \frac{2r_1}{c}\right) * f_{1^{st}order}(t, r_1) \cdot \sigma(r_1) dr_1 \quad (5.7)$$

Consequently, the term  $u_d(t) = \left[ u(t) - u\left(t - \frac{2\Delta r}{c}\right) \right]$  should approximate  $u(t)$  as well as possible. Now, recalling that  $u(t)$  is an RF-pulse that can be written (equation 3.8 ) as  $u(t) = \mathcal{Re}\{u_e(t) \cdot e^{j2\pi f_0 t}\}$ , we get:

$$u_d(t) = \mathcal{Re}\{u_e(t) \cdot e^{j2\pi f_0 t} - u_e\left(t - \frac{2\Delta r}{c}\right) \cdot e^{j2\pi f_0 \left(t - \frac{2\Delta r}{c}\right)}\} \quad (5.8)$$

$$\approx \mathcal{Re}\{u_e(t) \cdot e^{j2\pi f_0 t} \cdot (1 - e^{-j2\pi f_0 \frac{2\Delta r}{c}})\} \quad (5.9)$$

where the last approximation is valid for a transducer with a smooth pulse envelope i.e. a narrow band transducer. From this, we see that  $\Delta r = \lambda_0/4$  is the optimum choice, because it maximizes the factor:

$$\left(1 - e^{-j2\pi f_0 \frac{2\Delta r}{c}}\right) \Big|_{\Delta r = \lambda_0/4} = \left(1 - e^{-j2\pi f_0 \frac{1}{2f_0}}\right) = 2 \quad (5.10)$$

<sup>1</sup>An approximation similar to that in equation 5.6.

We see that we have no envelope distortion in this approximation. Furthermore, the first order echo signal is even amplified compared to the residual reverberation signal and always present electronic noise. (The gain in the signal to noise ratio for electronic noise is 3dB.) Choosing  $\Delta r$  as an odd integer multiple of  $\lambda_0/4$  will naturally give a maximum for the factor  $(1 - e^{-j2\pi f_0 \frac{2\Delta r}{c}})$ , too, but we are likely to violate our assumption of small  $\Delta r$ .

Yet, becoming more accurate, we will find a slight distortion of the first order echo signal due to the fact that the smooth envelope approximation is not fully suitable for wide band transducers. This naturally raises the question of whether or not the bandwidth has a significant influence on the optimum transducer shift. Further, it is interesting to know the behavior of the processed first order echo signal,  $v_{p,1^{st}order}$  when varying  $\Delta r$  around its optimum value. We will use simulations to examine these features in the following.

### Dependence on the bandwidth

First, we investigated the dependence of the optimal transducer shift on the envelope bandwidth. We simulated RF-pulses with Gaussian envelopes having a  $-6\text{dB}$  bandwidth of 2MHz, 3MHz, 4MHz and 5MHz, respectively. The envelopes were modulated at a center frequency of  $f_0 = 5\text{MHz}$ . For these RF-pulses, we calculated  $u_d(t)$  according to equation 5.8 for various values of  $\Delta r$ . The plot in figure 5.2 shows the normalized intensity  $I/I_0 = RMS\{u_d(t)\}/RMS\{u(t)\}$  versus the transducer shift.

We see that the position of the intensity maximum decreases with increasing bandwidth. However, this dependence is rather weak and even for a relative bandwidth of  $b = \Delta f/f_0 = 1$ , the actual optimum position deviates less than 10% from the theoretical value of  $\frac{\lambda_0}{4}$ .

We see also that the maximum is rather broad; thus we do not lose much intensity when using the theoretical optimum instead of the real optimum. If we do not want to lose more than 5% of the maximum available intensity, we have to be within a 15% interval of the optimum shift value for a given bandwidth. Finally, it is interesting to note that the maximum available intensity also decreases with increasing bandwidth. This is expected since a broader bandwidth means a shorter pulse. The proportion where the envelopes do not overlap increases and, consequently, the amplitude of the resulting envelope decreases.

### Dependence on the pulse form

The form of the envelope has no significant impact on the value of the optimal transducer shift as long as the bandwidth is the same. This becomes evident from the simulation

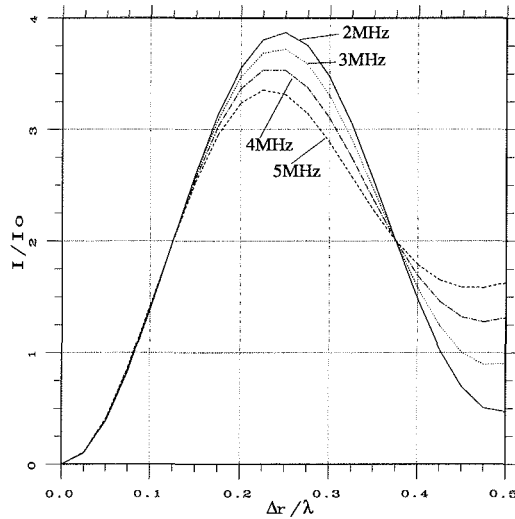


Figure 5.2: Intensity of the processed 1<sup>st</sup> order pulse versus transducer shift. The intensity is normalized to the intensity of the unprocessed 1<sup>st</sup> order pulse. The transducer shift is normalized to the wavelength at the center frequency  $\lambda_0 = \frac{1500\text{m/s}}{5\text{MHz}} = 0.3\text{mm}$ . The bandwidth of the pulse is a parameter.

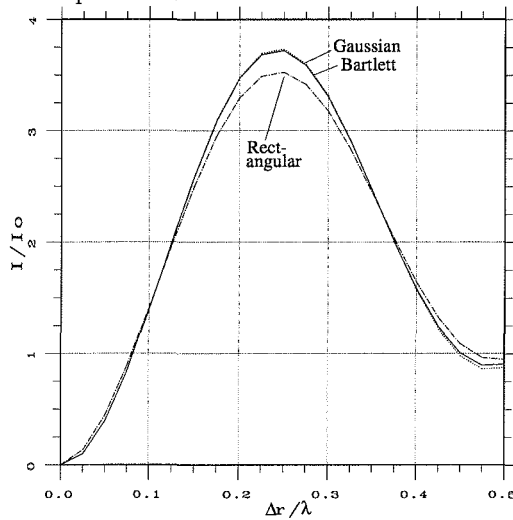


Figure 5.3: Intensity of the processed 1<sup>st</sup> order pulse versus transducer shift. The intensity is normalized to the intensity of the unprocessed 1<sup>st</sup> order pulse. The transducer shift is normalized to the wavelength at center frequency,  $\lambda_0 = 0.3\text{mm}$ . The envelope form is a parameter.

results plotted in figure 5.3. For the rectangular envelope, the maximum available intensity is slightly decreased compared to the other envelope forms. But, the rectangular envelope is also the envelope form which differs most from the one which can be realized.

### Dependence on the center frequency

A change in the center frequency of the transducer modifies, of course, the position of the maximum, but has no significant influence otherwise. The curves are simply dilated versions of each other if we presume that the relative bandwidth  $b = \Delta f/f_0$  stays constant (see figure 5.4).

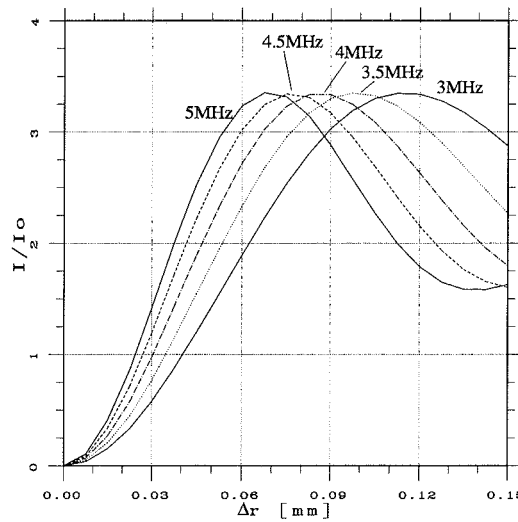


Figure 5.4: Intensity of the processed 1<sup>st</sup> order pulse versus transducer shift. The intensity is normalized to the intensity of the unprocessed 1<sup>st</sup> order pulse. The center frequency of the pulse is a parameter. The relative bandwidth of the different pulses is constant  $b = 1$ .

### Envelope distortion

Next, we will look at the envelope distortion as dependent on the bandwidth. Using  $\Delta r = \lambda_0/4$  as transducer shift, we see from equation 5.8 that the processed envelope becomes:

$$u_{d,e}(t) = u_e(t) + u_e\left(t - \frac{2\Delta r}{c}\right) \quad (5.11)$$

It is obvious that the envelope duration increases meaning that we lose resolution. Using the  $-6\text{dB}$  bandwidth of the Fourier transform of the envelope as a measure for resolution and comparing it with the bandwidth of  $u_e(t)$  (a Gaussian envelope in this case), we see (figure 5.5) that the loss in resolution is proportional to the squared relative bandwidth,  $b^2$ . The loss in resolution is less than 18% for a relative bandwidth less than  $b = 1$ . We think we can tolerate this loss compared to the benefit we get in reverberation reduction.

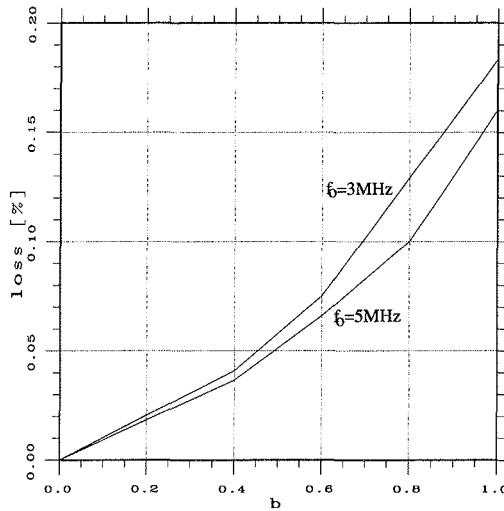


Figure 5.5: Loss in resolution in per cent versus relative bandwidth,  $b$ , of the RF-pulse. The center frequency of the transducer is a parameter.

After studying the most interesting parameters influencing the appearance of the processed first order echo signal, we will concentrate on the residual reverberation signal in the next section.

### 5.3 Residual reverberation signal

In practice, it is not possible to cancel the reverberation signal component completely. One reason for this is that the match between the two reverberation signal components will not be perfect. We are processing time discrete signals. Thus, even if we know the transducer displacement exactly, we cannot guarantee that we can match the reverberation signal components to better than half the sample step size at which we are operating.

Interpolation to a higher sampling rate enables us, however, to reduce this mismatch.

We can formulate the following approximative upper boundary for the residual reverberation signal in dependence of the sampling rate. Having a time delay,  $\delta T$ , between the two reverberation signal components, we get:

$$v_{rev,res}(t) \approx [\delta(t) - \delta(t - \delta T)] * u(t) * \delta'''(t) * \frac{1}{4c_a^6} \iint \delta(t - \frac{2r_1}{c}) * \delta(t - \frac{2r_3}{c}) * f_{revecho}(t, r_1, r_3) \cdot \sigma(r_1) \cdot \sigma(r_3) dr_1 dr_3 \quad (5.12)$$

Consequently, as  $\delta T \rightarrow 0$ , the convolution factor,  $[\delta(t) - \delta(t - \delta T)]$ , will vanish and so will the residual reverberation signal. To find out more about the dependence of this factor, we formulate it in the frequency domain:

$$RA(f) = |\mathcal{F}\{\delta(t) - \delta(t - \delta T)\}| = |1 - e^{-j2\pi f \delta T}| \quad (5.13)$$

As pointed out, the match cannot be guaranteed to be better than half the sample step size, i.e.:

$$\delta T \leq \frac{1}{2f_s} \quad (5.14)$$

where  $f_s$  is the signal sampling rate. Inserting this into equation 5.13, we get an approximative upper boundary for the reverberation attenuation:

$$RA(f) \leq |1 - e^{-j\pi \frac{f}{f_s}}| \quad (5.15)$$

In figure 5.6 this function is plotted for various center frequencies and we see for example, that for a 3MHz transducer  $RA(f_s = 10\text{MHz}) = -2\text{dB}$  (10MHz corresponds to sampling rate of the A/D converter in our experiment system). This is by no means sufficient. Consequently, we have to up-sample (interpolate) the signals to a higher rate in order to guarantee a better reduction.

## 5.4 Limits for improvement through up-sampling

As we may expect, there will be a lower limit where up-sampling will not lead to any further improvement. This limit defines an optimal sampling frequency at which we should perform the signal processing.

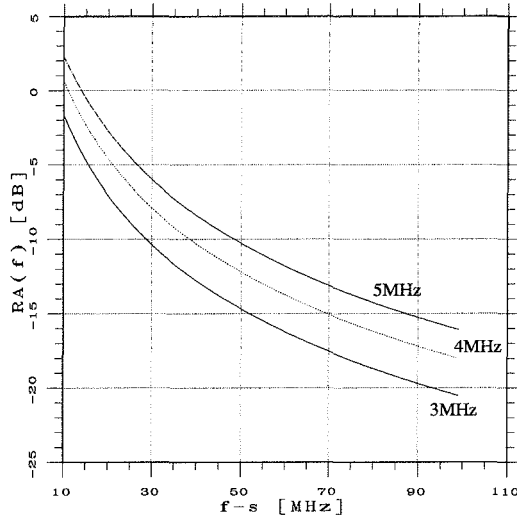


Figure 5.6: Approximative upper boundary of the reverberation attenuation factor in dependence of the sampling rate. The transducer center frequency is a parameter.

It is given either by the fact that the displacement of the transducer is not known exactly and we have to estimate it, or, that we reach the validity limit of approximation 5.6. The latter case will be studied first.

#### 5.4.1 Limit from model accuracy

Assuming a perfect match, we have a residual reverberation signal as given in equation 5.5. The attenuation of the reverberation signal will thus be proportional to the difference:

$$\Delta f_{revecho} = f_{revecho}(t, r_1, r_3) - f_{revecho}(t, r_1 - \Delta r, r_3 - \Delta r) \quad (5.16)$$

This expression cannot be treated analytically, and we will therefore use simulation results to get an idea of the significance of the difference,  $\Delta f_{revecho}$ .

We conducted the following simulation for the 3MHz transducer described in section 3.2.2. A first target consisting of 7 point targets assembled in form of a hexagon with a diameter of 10mm was placed at a range of  $r_1 = 10mm, 20mm, 30mm, 40mm, 50mm,$  and  $60mm$  on the axis in front of the transducer. A second target, identical to the first one in form, was placed on-axis at  $20mm, 40mm, 60mm, 70mm, 80mm, 90mm$  and  $100mm$ . The reverberation pulses were calculated and the targets were consecutively shifted by

0.1275mm i.e. approximately  $\lambda_0/4$  and the new reverberation pulses were calculated. These were matched to the phase of the first ones and subtracted. In figure 5.7, we show  $\frac{RMS(v_{rev, res})}{RMS(v_{rev})} \approx \frac{RMS(\Delta f_{revelcho})}{RMS(f_{revelcho})}$  versus the range of the first target,  $r_1$ , for  $\Delta r = \lambda_0/4$  and with the range of the second target,  $r_2$ , as a parameter. We observe that we cannot expect to reduce the reverberation pulse more than some  $-15\text{dB}$  to  $-20\text{dB}$  because of the change in  $f_{revelcho}$ . With this limit, we see from figure 5.6 that the sample frequency should be 50MHz–100MHz.

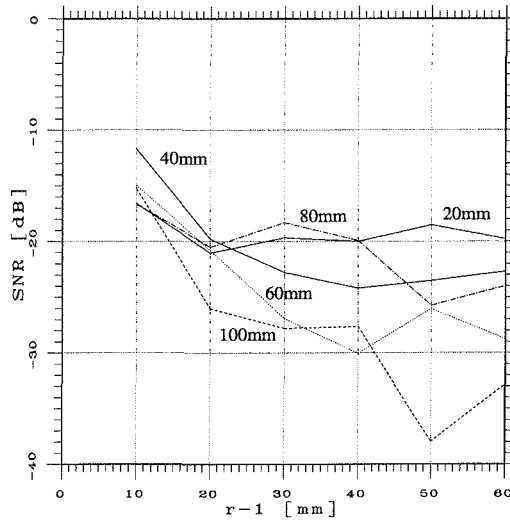


Figure 5.7: Effect of the change in the pulse envelope form when translating the transducer  $\lambda_0/4$  along the axis versus range of the first target. The range of the second target is a parameter.

#### 5.4.2 Sampling limit from shift variance

The actual transducer shift is always known only to a certain degree of accuracy given by mechanical constraints. Hence, we may have to estimate it. For this purpose, we can estimate the time lag between the two received signals,  $v_1(t)$  and  $v_2(t)$ . This is a very common problem within ultrasound imaging and many publications have been devoted to it [38][39]. The estimate itself has a certain variance that can be given a lower boundary by the Cramér-Rao bound. From [40], we find that the variance in the time delay error about the true time delay is given by:

$$\sigma^2(\Delta T - \hat{\Delta T}) \geq \frac{N_0}{\int_{-\infty}^{\infty} |2\pi f \cdot S(f)|^2 df} \quad (5.17)$$

Here,  $S(f)$  is the Fourier transform of the measured (noiseless) signal. In our case we have:

$$S(f) = \mathcal{F}\left\{u(t) * \frac{1}{2c_a^3} \int \delta\left(t - \frac{2r_1}{c}\right) * f_{1^{st}order}(t, r_1) \cdot \sigma(r_1) dr_1\right\} \quad (5.18)$$

i.e. we consider the reverberation signal contribution as additive noise which enters through  $N_0$ .

For a band-limited signal the Cramér-Rao bound is equivalent to [40]:

$$\sigma(\Delta T - \hat{\Delta T}) \geq \left(\frac{1}{8\pi^2}\right)^{\frac{1}{2}} \frac{1}{\sqrt{\text{SNR}}} \frac{1}{\sqrt{T\Delta f}} \frac{1}{f_0} \frac{1}{\sqrt{1 + \frac{\Delta f^2}{12f_0^2}}} \quad (5.19)$$

where SNR is the signal-to-noise ratio,  $T$  the observation time, and  $\Delta f$  the bandwidth of the signal.

In our case, we have typically  $f_0 = 3\text{MHz}$ ,  $\delta f = 2\text{MHz}$ ,  $T = 0.13\text{ms}$ ,  $\text{SNR} = 20\text{dB}$  giving:

$$\sigma(\Delta T - \hat{\Delta T}) = 0.7\text{ns} \quad (5.20)$$

This suggests that there may be a benefit in up-sampling up to:

$$f_s = \frac{1}{2\sigma(\Delta T - \hat{\Delta T})} = 703\text{MHz} \quad (5.21)$$

We can thus conclude that the actual limit is given by the inaccuracy in our approximations and not by our ability to estimate the transducer shift precisely enough. The found limit of 50MHz-100MHz corresponds to experimental findings where the signals were up-sampled to the point where no further improvement was obtained [41].

## 5.5 Filter scheme

The signal processing scheme for a realization of the algorithm is summarized in the scheme in figure 5.8. Actually, it is not necessary to perform the sampling rate conversion by a factor  $M$  to a higher rate, if we only want to perform a determined subsample resolution shift. As detailed in [36] or [42] a polyphase filter of the form:

$$p_\rho(n) = h_{LP}(nM + \rho) \quad (5.22)$$

can be designed for this task. Here,  $h_{LP}(m)$  are the coefficients of a lowpass filter suitable to remove the image spectra, which are caused by up-sampling to the high sampling rate  $Mf_s$ . The number  $\rho$  defines the subsample shift i.e. the input signal is delayed by the fraction  $\rho/M$ . Note that the actual processing is done at the low rate,  $f_s$ .

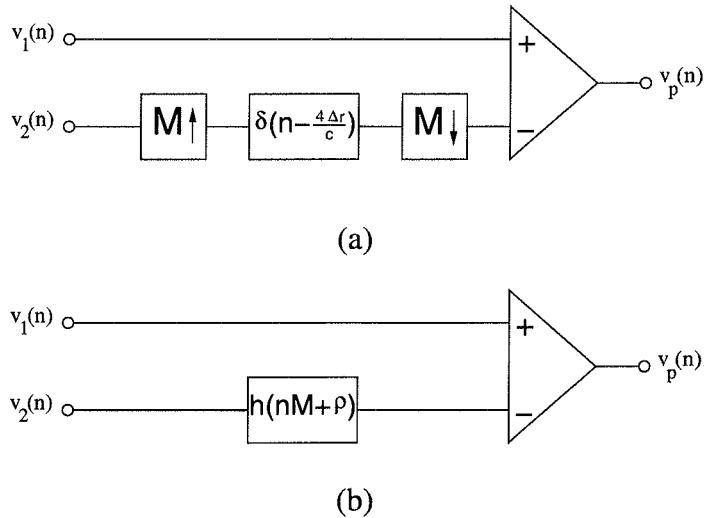


Figure 5.8: Signal processing scheme for the reverberation reduction scheme. General realization (a), low rate realization with a polyphase filter (b).

## 5.6 An alternative to transducer displacement

A further aspect is the realization of the propagation lag. So far, we have discussed a mechanical displacement of the transducer. Another possibility is to use a phase plate[43]. This means that the transducer is not translated, but a thin plate with a velocity of sound different from that of the dome fluid is introduced into the sound path when acquiring the second signal. The reverberation pulse has to travel four times through the plate whereas the first order echo passes only twice. This results again in a different propagation lag change for reverberations and the first order echoes.

However, a disadvantage with this method will be the echo and the induced reverberations from the phase plate itself. Since the phase plate echoes/reverberations occur only in the second signal they are not filtered out by the algorithm. Whether such phase plate

echoes are significant or not remains to be investigated by experiments.

## 5.7 Phantom experiments

The next step in evaluating the proposed reduction method was to perform 2D imaging. Since we lacked a prototype of a probe displacing the transducer within its protecting dome or introducing a phase plate into the beam, we were restricted to conducting water-tank experiments. The probe was mounted in a holder over a water tank thus the transducer was immersed just into the water. The holder could be translated precisely along the probe axis by a step motor. The minimum step size was  $10\mu m$ .

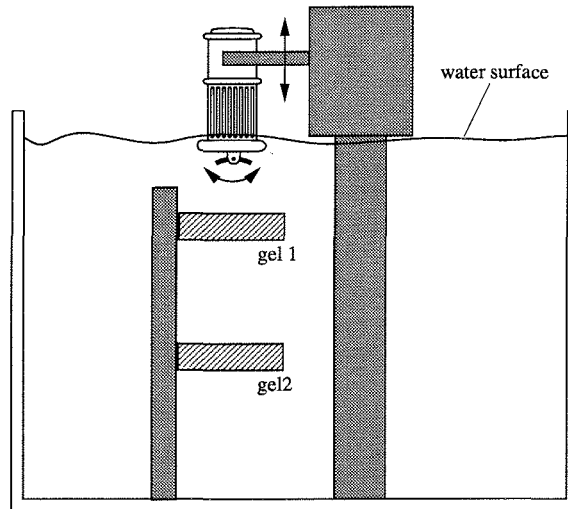


Figure 5.9: Water tank experiment set-up.

In a first experiment, we placed two agarose<sup>2</sup> gelatine blocks in the water tank (see figure 5.9) and imaged them by a 2D-sector scan. The transducer again had a center frequency of  $f_0 = 3\text{MHz}$  and a relative  $-6\text{dB}$ -bandwidth of  $b = 0.44$ . The quarter wavelength in water is thus  $\frac{\lambda_0}{4} \approx 125\mu m$ . Further, the dome was removed from the probe to get rid of the echoes from the dome/water interface. In the experiment, the dome would have followed the movement of the transducer and this would not have been in conformance with our assumption

<sup>2</sup>#A360 Fisher Scientific

that the target distribution remains the same before and after transducer displacement.

We acquired the RF-signals of several frames with different transducer displacements,  $\Delta r$ . Consecutively, pairs of frames were processed as detailed above in order to reduce reverberations. Finally, conventional processing steps such as demodulation, magnitude range compression, etc. were performed to get the display images. A time gain compensation was, however, not necessary because we can neglect attenuation in water and the water based gels.

Figure 5.10 shows the processing result for a displacement of  $\Delta r = 100\mu\text{m}$ . (The scan with  $\Delta r = 120\mu\text{m}$ , which is closer to  $\lambda_0/4$ , proved to be erroneous due to some synchronization problems.) In the upper image, we see the original frame with the two agar gels and the reverberation between the first water-agar interface and the transducer showing up in the gap between the gels. This reverberation is significantly reduced after applying our method. Admittedly, reverberations are commonly not as dominating as in the presented experiment. (For instance, the losses in the dome fluid contribute to their attenuation.) But, the intention was to test and visualize the performance of the algorithm.

To further approximate a real situation, we used a bacon slice as the first target in a further experiment. The second target was again an agarose gelatine block and the probe displacement was  $100\mu\text{m}$ . In the unprocessed image (see figure 5.11), we observe that the reverberation cloud stretching from the image center to the right beneath the bacon signal has a strength that is comparable to that of the gel echo signal. After applying the reduction approach, reverberations, especially those in the image center, are significantly reduced (around 11dB). Yet the reduction proves to be inferior at the edge of the image sector. Searching for a reason for this behavior, we found a possible explanation in the way we performed the transducer translation. As detailed, we moved the whole probe, not just the transducer, along its center axis in the experiment. This reflects a possible design constraint. Because of inertia it might be difficult to have a mechanism that translates only the transducer and that has to be rotated rapidly together with the transducer to perform the scanning.

But translating the probe, instead of the transducer, leads to a different displacement,  $\Delta r_v$ , along the transducer axis compared to the displacement,  $\Delta r$ , along probe axis when there is an angle,  $\alpha$ , between the two axes. From figure 5.12, it becomes clear that:

$$\Delta r_v = \Delta r \cdot \cos(\alpha) \quad . \quad (5.23)$$

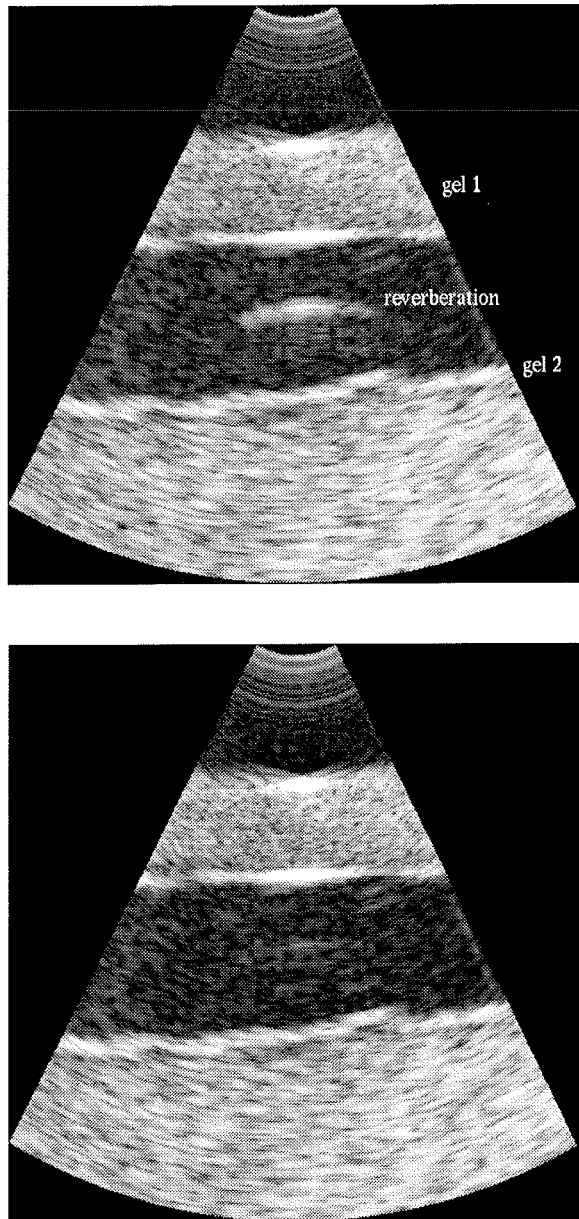


Figure 5.10: 2D sector scan image of two agarose gel in water before (upper) and after (lower) reverberation reduction.

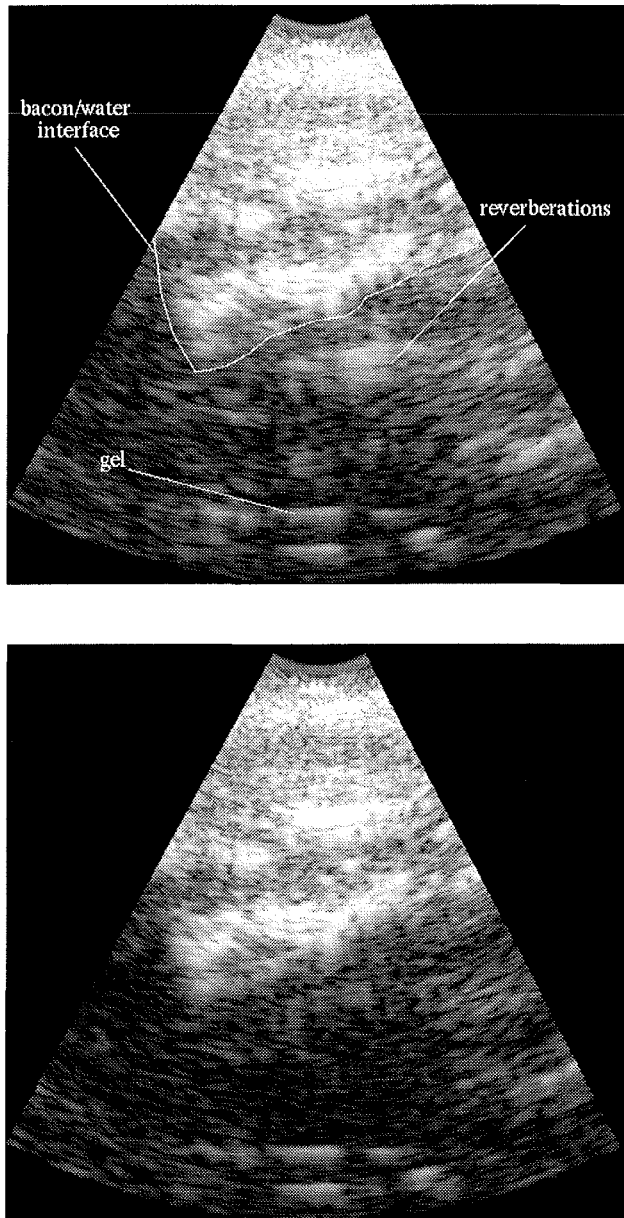


Figure 5.11: 2D sector scan image of a bacon slice and an agarose gels before (upper) and after (lower) reverberation reduction.

Additionally, a lateral shift of  $\Delta r_h = \Delta r \sin(\alpha)$  is introduced.

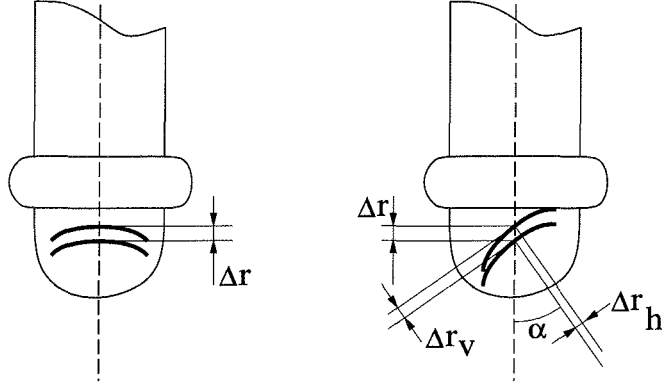


Figure 5.12: Situation when the transducer is moved along the probe axis while steered off-probe-axis.

If we neglect the lateral shift<sup>3</sup>, we can use equation 5.13 to determine if we should compensate for the vertical variation in  $\Delta r_v$  or if we can neglect it. Depending on the angle,  $\alpha$ , to which the transducer is steered, the time lag mismatch in the residual reverberation signal will be:

$$\delta T = \frac{4\Delta R(1 - \cos(\alpha))}{c} = \frac{\lambda_0}{c}(1 - \cos(\alpha)) \quad (5.24)$$

where it is supposed that we have chosen the theoretical optimum transducer shift  $\Delta R = \frac{\lambda_0}{4}$ . Inserting this in equation 5.13, we get:

$$RA(f, \alpha) = |1 - e^{j2\pi \frac{f}{f_0}(1 - \cos(\alpha))}| \quad (5.25)$$

This function is plotted in figure 5.13 for  $f = f_0$ . We see that the attenuation factor increases over 0.1 (-20dB) for  $\alpha > 10^\circ$ . Consequently, we should account for the effect when performing the back shift of the signals.

We estimated the actual radial transducer displacement for each beam signal of the bacon experiment by extracting the maximum position of the cross-correlation. Inspecting the estimated displacement variation in dependence of the angle (figure 5.14), we find the expected cos-function dependence.

<sup>3</sup>A valid assumption since the ultrasound beam has lowpass characteristics in the lateral direction.

However, when the corrected shift was applied in the processing scheme, the improvement was very poor (figure 5.15). We were not able to explain this, but suspect that the remaining signal might be due to other noise sources.

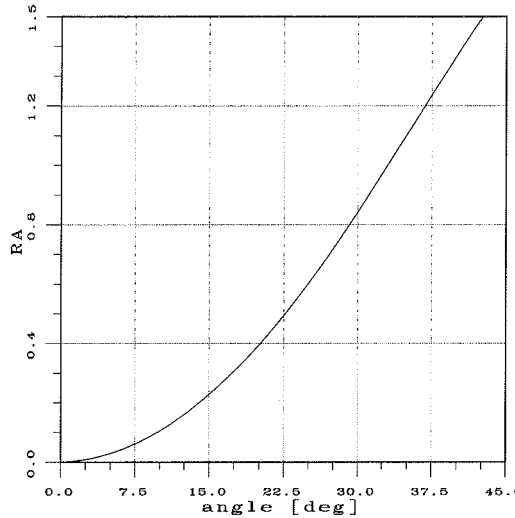


Figure 5.13: Estimated and theoretical transducer displacement measured in pixels as a function of the beam angle (number).

## 5.8 Summary and discussion

In this chapter, we presented a method to reduce reverberations that are due to a reflection at the transducer surface. Reverberations were reduced efficiently by processing two RF-signals that were acquired under same conditions with just a slight displacement of the transducer. The optimal displacement was found to be near to the theoretical narrow-band optimum value of  $\lambda_0/4$ . It proved not to be critical if the displacement optimum was not matched accurately.

From theory we could expect a reverberation reduction of 15dB to 20dB plus a 3dB gain of the first order echoes against the electronic noise floor. In the experiments, the reduction was around 11dB.

First order echoes were not distorted significantly and the loss in resolution due to envelope broadening was hardly visible in the displayed ultrasound images.

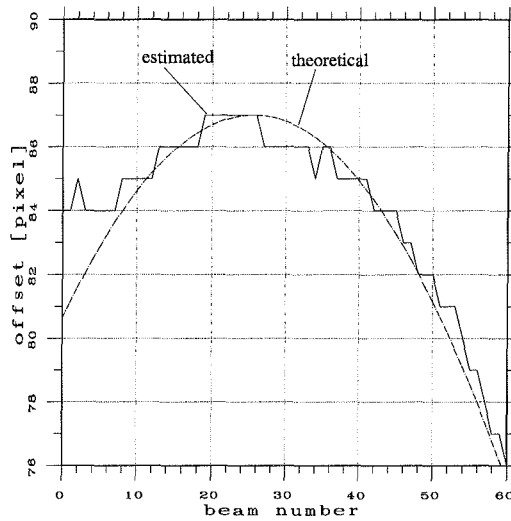


Figure 5.14: Reverberation attenuation factor in dependence of the steering angle when not compensated.

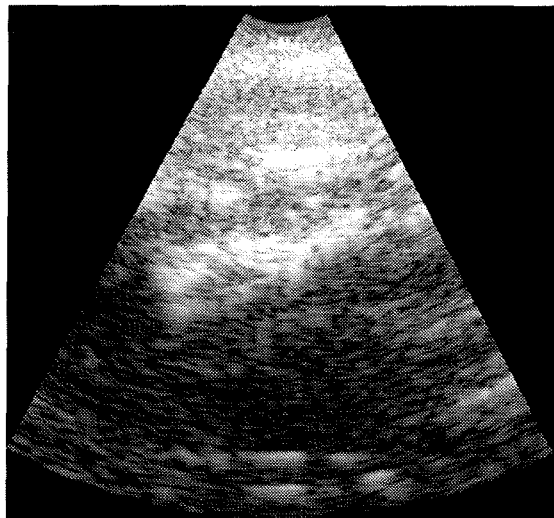


Figure 5.15: Improved reverberation cancelation by accounting for the angle dependent shift. An improvement is, however, hardly visible.

The disadvantage with the method is that the transducer (or a phase plate) must be moved mechanically. This makes a new probe design necessary which is cost-intensive. Further, we do not see a good way to transfer the method to electronically phased arrays, which have no fluid filled dome in which the transducer can be displaced without distorting the target distribution. Therefore, we will look for further reduction algorithms in the next chapters.



## Chapter 6

# Reverberation reduction by impedance change

In the following, we present another approach to reducing reverberations that are due to a reflection at the transducer surface. As in the method of Chapter 5, we acquire two images of the target distribution. But this time, instead of moving the transducer, we change the electric receive impedance of the transducer elements. As alluded to in section 3.4.1, this will modify the reflection factor of the transducer, or, to be more precise, it will change only the electric component. As shown in the following, it is thus possible to extract the electric component of the reverberation signal from the total received RF-signal. Having found the electric component, an appropriate mapping lets us determine an approximation of the acoustic component and, finally, we can subtract both components from the total signal.

### 6.1 The algorithm

We recall that the total signal at the electrical port of the transducer is given by the sum of the first order signal, the transducer reverberation contribution and other present noise contributions:

$$v(t) = v_{1^{st}order}(t) + v_{rev}(t) + n(t) \quad (6.1)$$

In the Fourier domain, the first order signal can be written as (see equations 3.6 and 3.41):

$$V_{1^{st}order}(f) = 2V_g(f)H_{tt}^2(f)H_i(f) \cdot S(f) \quad (6.2)$$

where  $S(f)$  is the transfer function representing the effects of the acoustic pulse propagation in the medium,  $V_g(f)$  is the driving voltage and  $H_{tt}(f)$  is the transfer function of the transducer. We see that the first order signal is directly proportional to:

$$H_i(f) = \frac{Z_i(f) \cdot Z_r(f)}{Z_i(f) + Z_r(f)} \quad (6.3)$$

and thus actually depends on the receive impedance  $Z_r(f)$ <sup>1</sup>.

In the same way, for the received reverberation signal combining equations 3.6, 3.54 and 3.77 we find:

$$\begin{aligned} V_{rev}(f) &= 2V_g(f)H_{tt}^2(f)H_i(f) \cdot (R_{ac}(f) \cdot S_{ac}(f) + H_{tt}^2(f)H_i(f)2Z_{LA} \cdot S_{el}(f)) \\ &= \underbrace{2V_g(f)H_{tt}^2(f)H_i(f) \cdot R_{ac}(f) \cdot S_{ac}(f)}_{V_{rev,ac}} \\ &\quad + \underbrace{2V_g(f)H_{tt}^2(f)H_i(f) \cdot H_{tt}^2(f)H_i(f)2Z_{LA} \cdot S_{el}(f)}_{V_{rev,el}}. \end{aligned} \quad (6.4)$$

We see that the electric reverberation component,  $V_{rev,el}$ , is proportional to  $H_i^2(f)$ , whereas the acoustic reverberation component,  $V_{rev,ac}$  is, like the first order signal, proportional to  $H_i(f)$ .

Next, we acquire two signals,  $v_1$  and  $v_2$ , with two different receive impedances,  $Z_{r,1}$  and  $Z_{r,2}$  and define the difference signal,  $\Delta$ , neglecting other noise contributions and dropping the explicit notation for frequency dependency:

$$\begin{aligned} \Delta &= H_{i,2} \cdot V_1 - H_{i,1} \cdot V_2 \\ &= H_{i,2} \cdot V_{rev,el,1} - H_{i,1} \cdot V_{rev,el,2} \\ &= 2V_g H_{tt}^2 H_{i,1} H_{i,2}^2 2Z_{LA} \cdot S_{el} (H_{i,1} - H_{i,2}) \end{aligned} \quad (6.5)$$

<sup>1</sup>Note that we assume equal element transfer functions and equal receive impedances in the case of array transducers.

This equation is equivalent to:

$$2V_g H_{tt}^2 H_{i,1} H_{tt}^2 H_{i,1} 2Z_L A \cdot S_{el} = \frac{H_{i,1} \Delta}{(H_{i,1} - H_{i,2}) H_{i,2}}$$

i.e.

$$V_{rev,el,1} = \frac{H_{i,1} \Delta}{(H_{i,1} - H_{i,2}) H_{i,2}} \quad (6.6)$$

Hence, we have isolated the electrical component of the reverberation signal and can subtract it from the total signal. However, since the acoustic component has a phase difference of  $\Delta\varphi = 180^\circ$  compared to the electric component, we would actually increase the total reverberation signal. In other words, we also have to find an estimate of the acoustic component of the reverberation signal and subtract both components from the total signal. Consequently, we have to look for a mapping:

$$V_{rev,el} \rightsquigarrow V_{rev,ac} \quad (6.7)$$

from the electric component to the acoustic component.

## 6.2 Determining the acoustic component

We have observed earlier that the two reverberation components differ in the RF-pulse, i.e. the pulse that is measured when a single point target in the focus of the transducer reverberates against itself (plane wave case) and that they also differ in their beam patterns, i.e. the way in which a reflected pulse propagates from the transducer into the medium.

In a first step, we assume a plane wave situation (i.e. the acoustic impulse propagation for both components is equal) and study the performance of an inverse filtering scheme to get:

$$\hat{V}_{rev,ac}(f) = W(f) \cdot V_{rev,el}(f) \quad (6.8)$$

where:

$$W(f) = \frac{V_{rev,ac}(f)}{V_{rev,el}(f)} \quad (6.9)$$

in a straight forward approach, or:

$$W(f) = \frac{V_{rev,el}^*(f) \cdot V_{rev,ac}(f)}{|V_{rev,el}(f)|^2 + 1/SNR} \quad (6.10)$$

in a Wiener filter approach.

Since the RF-pulse of the electric reverberation component has no singularities in the interesting frequency band (see figure 3.24) a pure inverse filter may perform sufficiently well. In the next section, this question is examined with the help of simulations.

In a second step, we examine the performance of the scheme using the propagation pattern of the electric component as an estimate for the acoustic propagation pattern. Here, important aspects are the scatterer distribution and the size of the transducer elements.

### 6.2.1 Testing inverse filtering schemes

In order to test the inverse filtering scheme, we generated artificial RF-signals of the two reverberation components by convolving a Gaussian distributed, white random sequence with the measured RF-pulses  $v_{ac}(t)$  (equation 3.61) and  $v_{el}(t)$  (equation 3.62). The convolution was performed at a sampling rate of 100MHz.

Next, we decimated the RF-signals by a factor of 10 and added white noise to both signals, accounting for other present distortions. The resulting signals are shown in figure 6.1.

Then, we calculated the filters from the decimated<sup>2</sup> versions of  $v_{ac}(t)$  and  $v_{el}(t)$  and performed the inverse and the Wiener filtering. The resulting estimates are plotted in figures 6.2 and 6.3, respectively, for a signal-to-noise ratio  $SNR = 20\text{dB}$ . We see that the two estimates correspond well to the original signal. The RMS value of the error between the estimate and the original is given in Table 6.1 for different SNR values of the additive noise. We see that the two filter schemes perform almost equally with the Wiener filter performing slightly more favorably. The magnitudes of the filter frequency responses are given in figure 6.4. Within the frequency band of the transducer, the filter responses are nearly the same, explaining the comparable performance. The magnitude of inverse filter rises sharply only at the band edges; this continues until a preset threshold is reached. Magnitudes above this threshold are interpreted as noise and they are truncated to zero.

Consequently, if we have a signal to noise ratio of 20dB–30dB, the estimation error after inverse filtering is low enough to make the reverberation reduction scheme interesting. Or,

---

<sup>2</sup>by a factor of 10, obtaining thus a rate of 10MHz

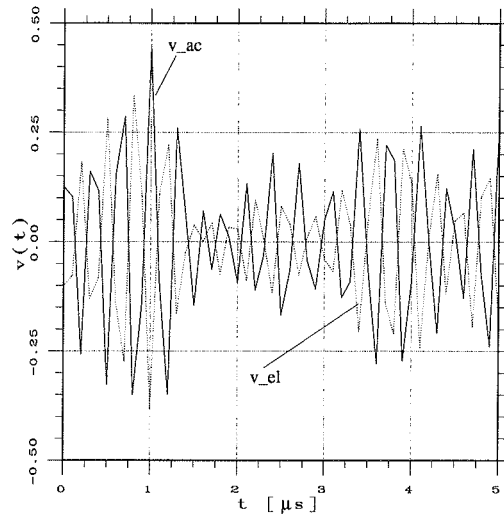


Figure 6.1: Simulated RF-signals of the electric and acoustic reverberation components. As expected, the signals have a phase difference of  $180^\circ$ .

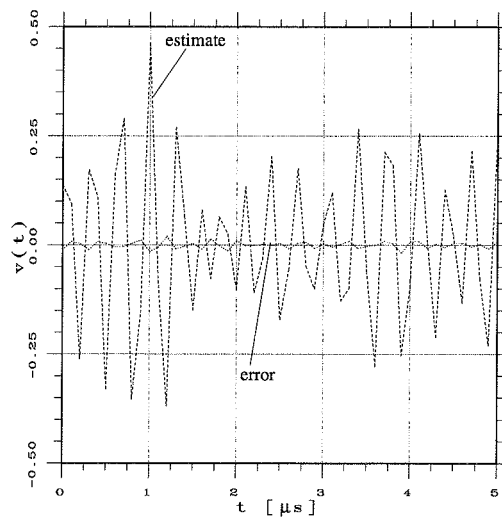


Figure 6.2: Estimated acoustic component and the estimation error using a simple inverse filter.

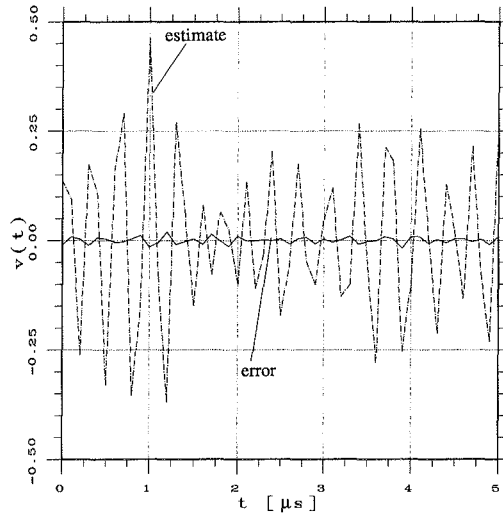


Figure 6.3: Estimated acoustic component and the estimation error using a Wiener filter.

in other words, we can expect the limitations of the scheme to be given by constraints other than by inverse filtering performance because the electronic noise level commonly lies well below  $-20\text{dB}$ .

SNR in dB	Inverse filter $E_r/N_{rev}$ in dB	Wiener filter $E_r/N_{rev}$ in dB
10	-5.0	-5.5
20	-14.3	-14.6
30	-24.3	-24.3
40	-34.0	-34.0
$\infty$	-46.3	-47.8

Table 6.1: Reverberation reduction using an inverse filter and a Wiener filter in dependence of additive noise strength (SNR)

### 6.2.2 Effect of the different beam patterns

As mentioned above, the beam pattern of the electric and acoustic component differ. The electric pattern will always radiate in a direction perpendicular to the element surface

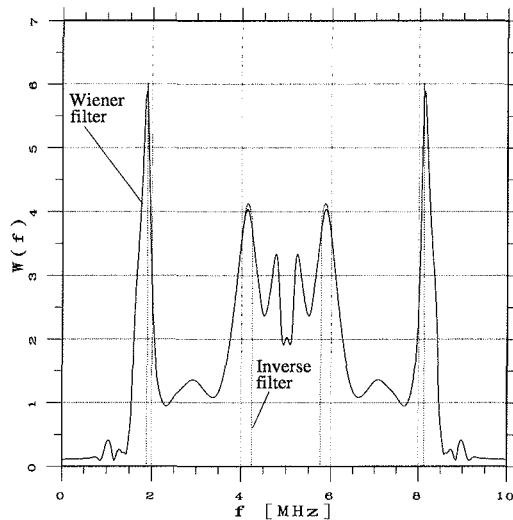


Figure 6.4: Magnitude of the frequency response of the inverse and Wiener filter.

whereas the acoustic component radiates in a direction determined by the angle between the incoming wave and the transducer surface (Snell's law). Thus, if transducer elements exhibit a strong directivity i.e. if the element diameter exceeds the wavelength of the RF-pulse, the two beam pattern will differ significantly and there would seem to be little hope to succeed with our reduction scheme. However, thinking of phased array transducers rather than annular array transducers, element sizes are designed (at least for the azimuth direction) to radiate as uniformly as possible over an as large as possible angle. In this case, the acoustic beam pattern and the electric beam pattern become more comparable. To illustrate this, in figure 6.5 we show the monochrome reverberation radiation diagrams in the azimuth direction for element sizes of 1mm and 0.18mm. The wavelength is 0.5mm. An incoming spherical wave hits the element under an angle of  $45^\circ$  (from the right). For the 1mm element and the acoustic component, the outgoing wave directs its main energy towards  $45^\circ$  to the left i.e. a distinct main lobe is observed, while the main lobe of the electric component radiates perpendicular to the element.

For the 0.18mm width element, we do not observe a clear main lobe or, in other words, the main lobe is very broad and energy is radiated in almost all directions. Still, there is a main direction that again points perpendicular to the element surface for the electric

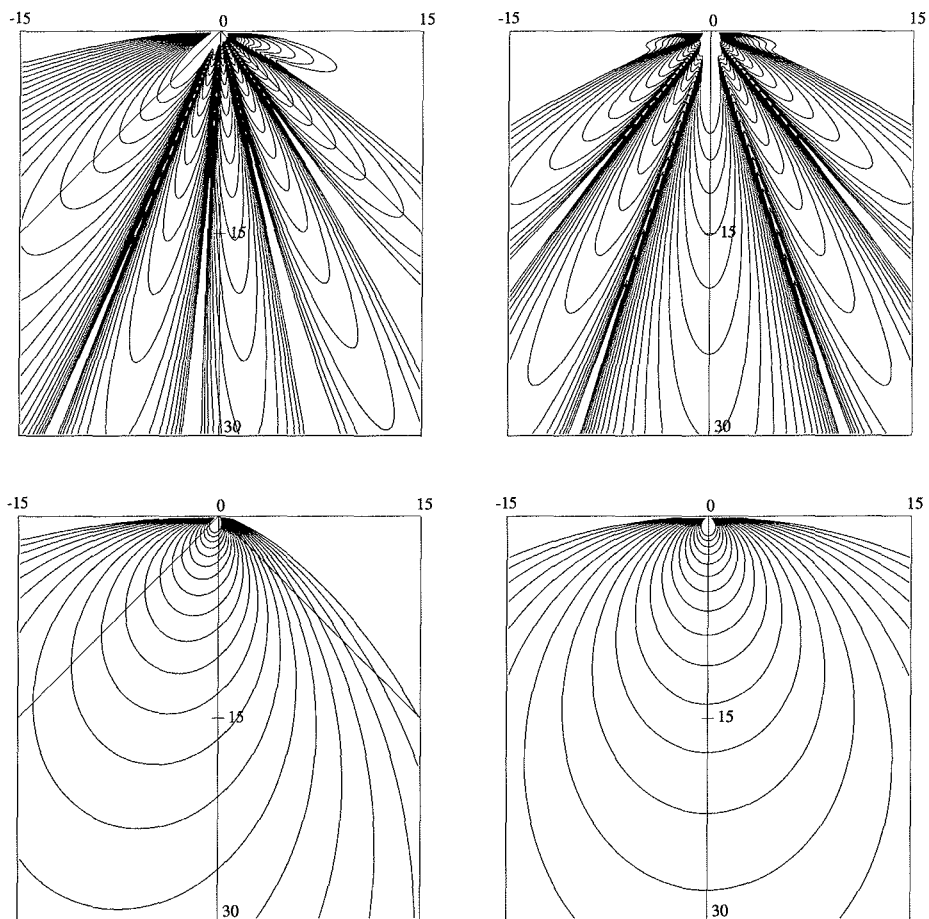


Figure 6.5: Monochrome ( $\lambda = 0.5\text{mm}$ ) reverberation radiation diagram of an element. Acoustic component (left) and electric component (right). The element width is 1mm (top) and 0.18mm (bottom). Contours of equal signal amplitude are shown. The dimensions at the coordinate axes are given in millimeters.

component. But for the acoustic component, the main direction has turned towards the element axis even though the incoming wave direction was the same.

Hence, for a phased array transducer with a typical element width of  $180\mu\text{m}$  and a center frequency of  $3\text{MHz}$ , we can expect that the beam profiles are comparable. Consequently, the reduction scheme should perform well. However, with an element height of  $10\text{mm}$  (though the elements are mechanically focused in the elevation plane) the effect of the different beam pattern may dominate and the reduction algorithm may break down. To investigate this further, we conducted simulations with various reflectors placed at different locations.

### 6.3 Simulations for various target distributions

In this section, we present the results of simulations applying the devised reverberation reduction algorithm to echo signals generated from different target configurations. We concentrated on situations where we had two targets. The first one was located in the near field region of the transducer ( $0\text{mm}$ – $40\text{mm}$ ), while the second target was placed in the far field region and on the transducer axis. Moreover, since it is common to apply dynamic focusing in order to obtain a narrow receiver beam, we could approximate the second target by a point scatterer to shorten computation time. (For a simulation examining this assumption, see Appendix C). In the near field, however, the ultrasound beam is rather broad and we have to account for the target extension. Therefore, we represented the target e.g. a muscle/fat interface, by a mesh of point scatterers. If not stated otherwise this mesh had a grid width of  $0.5\text{mm}$  and consisted of 40 points in the x-direction (azimuth) and 20 points in the y-direction (elevation) thus spanning a surface of  $20\text{mm} \times 10\text{mm}$ . The z-coordinate defining the shape of the interface was given as:

$$z = f(x, y) \tag{6.11}$$

where the function  $f(\cdot)$  was varied for different target configurations. Further, we also varied the distance between the second target and the transducer.

In the simulations, we calculated only the signal components for the reverberation between the two targets and did not analyze the reverberations of the targets against themselves, nor did we look at the first order echoes. We then calculated the estimate of the acoustic component by inverse filtering the electric component as described in section 6.2.

The transducer used for the simulations was the already mentioned 96 element phased array with an element pitch of  $190\mu\text{m}$  and an element size of  $0.18\text{mm} \times 10\text{mm}$ .

### 6.3.1 Plane and curved interfaces

In a first batch of simulations, we placed the interface in the near field at a distance of 10mm in front of the transducer. The shape of the interface varied as illustrated in figures 6.6 and 6.7 and we refer to these shapes in the following as target shapes I through V.

The point target in the far field was placed at a range of 90mm. Figures 6.8–6.12 show the simulation results. At the top of each figure the RF-signals of the acoustic and electric component,  $v_{ac}(t)$  and  $v_{el}(t)$  are plotted together with the estimated signal  $\hat{v}_{ac}(t) = w(t) * v_{el}(t)$  (where  $w(t)$  is the impulse response of the inverse filter defined in section 6.2). At the bottom of each figure, we show the total reverberation signal before reduction,  $v_{rev}(t) = v_{ac}(t) + v_{el}(t)$  and the reduced reverberation signal  $v_{rev,r}(t) = v_{ac}(t) - \hat{v}_{ac}(t)$ . The reduction gain is defined as

$$G = \frac{RMS(v_{rev}(t))}{RMS(v_{rev,r}(t))} \Big|_{dB} \quad (6.12)$$

We observe that the average reduction is about 9dB. The variance in the performance is explained with the more or less focusing or defocusing of the scattered wave in dependence of the curvature of the interface. The results will presumably vary with the range of the scatterers. We therefore performed corresponding simulations (meaning the shape of the interfaces were the same) for the following range combinations:

simulation code	range 1 <sup>st</sup> target [mm]	range 2 <sup>nd</sup> target [mm]
S-1.4	10	40
S-1.6	10	60
S-3.9	30	90
S-3.4	30	40

The reduction gains,  $G$ , for these cases are given in Table 6.2.

It is not surprising that simulation S-1.6 gives the best results. The transducer had its fixed focus in the elevation direction at 60mm, thus there is no difference in the beam pattern of the acoustic and electric component along elevation. The remaining error is due to the difference of the beam pattern in azimuth direction and an additional numerical error which is not quantified and may be dominating here.

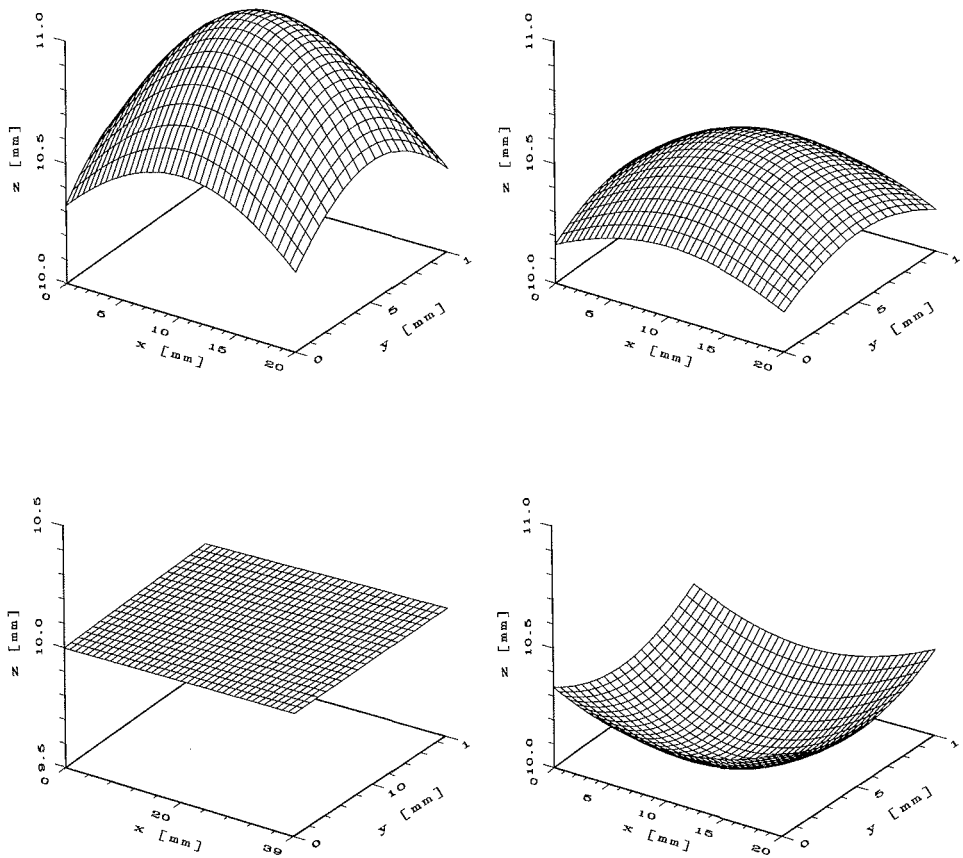


Figure 6.6: Different shapes of the simulated muscle/fat interface placed at a range of 10mm. Upper left: shape I, upper right: shape II, lower left: plane shape, lower right: shape III.

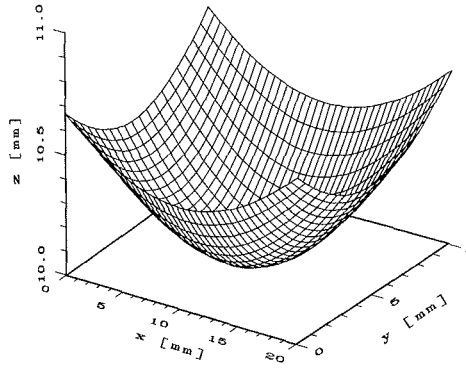


Figure 6.7: Shape IV of the simulated muscle/fat interface.

	curved I	curved II	plane	curved III	curved IV
G in dB for S-1.9	12.6	11.3	10.6	7.5	6.8
G in dB for S-1.4	12.4	12.1	5.5	3.9	2.6
G in dB for S-1.6	17.5	16.4	22.6	19.8	11.3
G in dB for S-3.9	5.5	7.7	11.3	14.1	9.0
G in dB for S-3.4	2.6	9.9	11.7	15.2	10.0

Table 6.2: Reduction gain,  $G$ , for the different interface shapes placed at different target ranges.

The average reduction gain for the values in the table is 10.8dB<sup>3</sup>. However, we see that when the second target is placed in the transition zone between the near and far field (i.e. at 40mm), the reduction gain can drop to mere 2.6dB.

### 6.3.2 Tilted interfaces

Next, we investigated the case when a plane interface is tilted by an azimuth (elevation) angle,  $\alpha_x$ , ( $\alpha_y$ ), around the  $y$ -axis ( $x$ -axis), (see figure 6.13). The calculated reduction gains for various angles and target ranges are given in Table 6.3.

We see that tilting the interface in the azimuth plane is not very critical. The reduction

<sup>3</sup>Though one might discuss the meaning of this value.

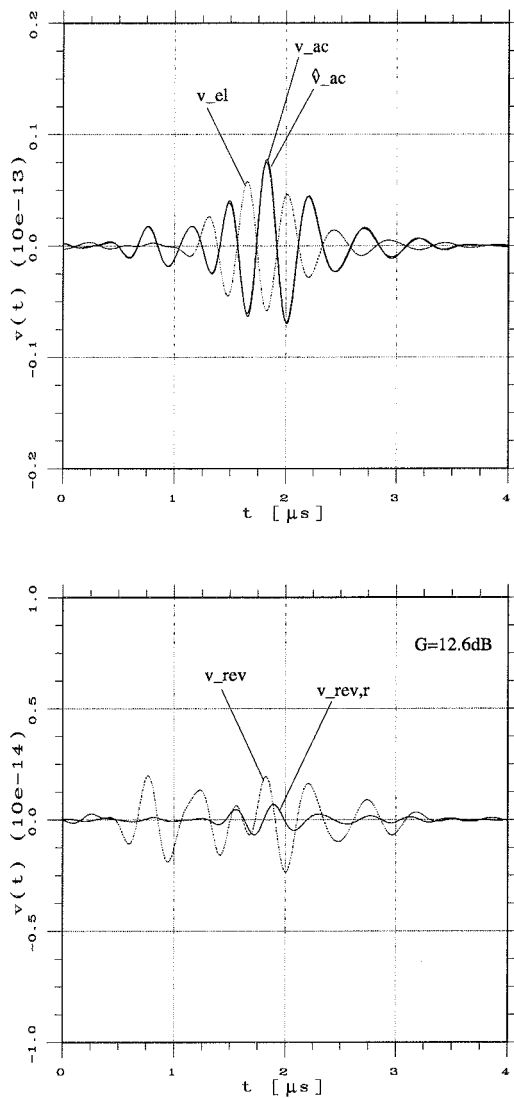


Figure 6.8: Reverberation signal components (electric/acoustic) and estimated acoustic component for the curved interface I at 10mm and a point target at 90mm (top). Total reverberation signal and reduced reverberation signal (bottom).

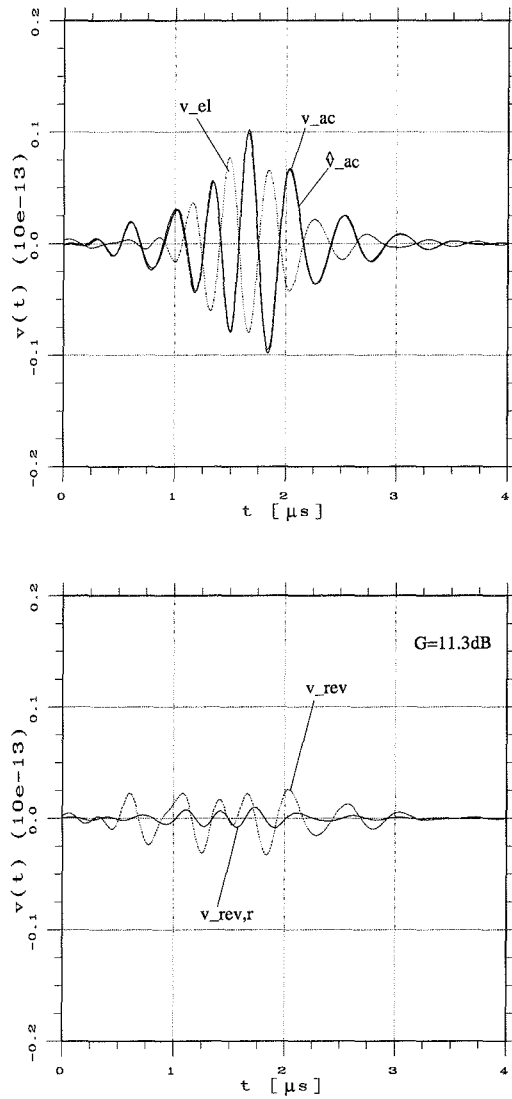


Figure 6.9: Reverberation signal components (electric/acoustic) and estimated acoustic component for the curved interface II at 10mm and a point target at 90mm (top). Total reverberation signal and reduced reverberation signal (bottom).

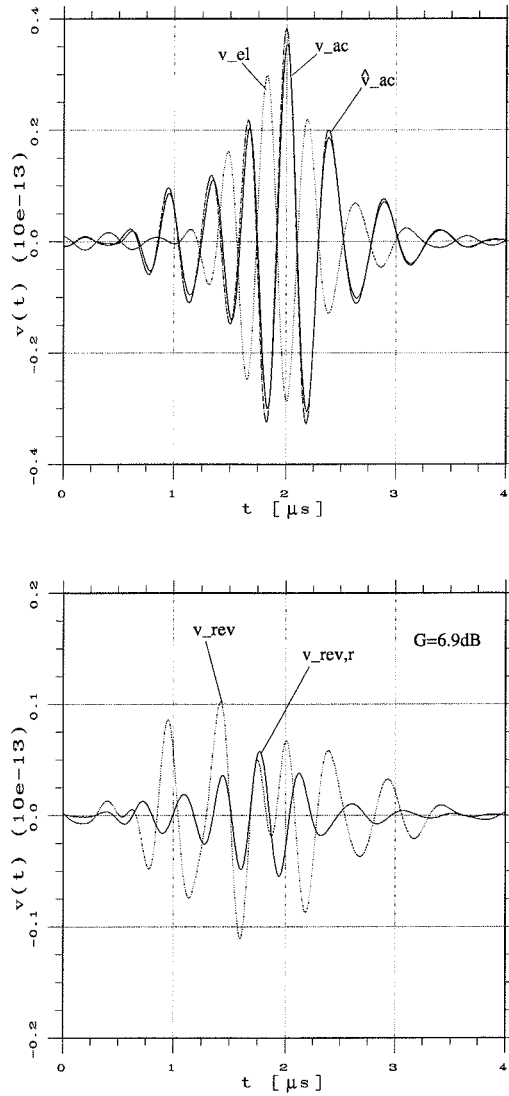


Figure 6.10: Reverberation signal components (electric/acoustic) and estimated acoustic component for a plane interface (shape III) at 10mm and a point target at 90mm (top). Total reverberation signal and reduced reverberation signal (bottom).

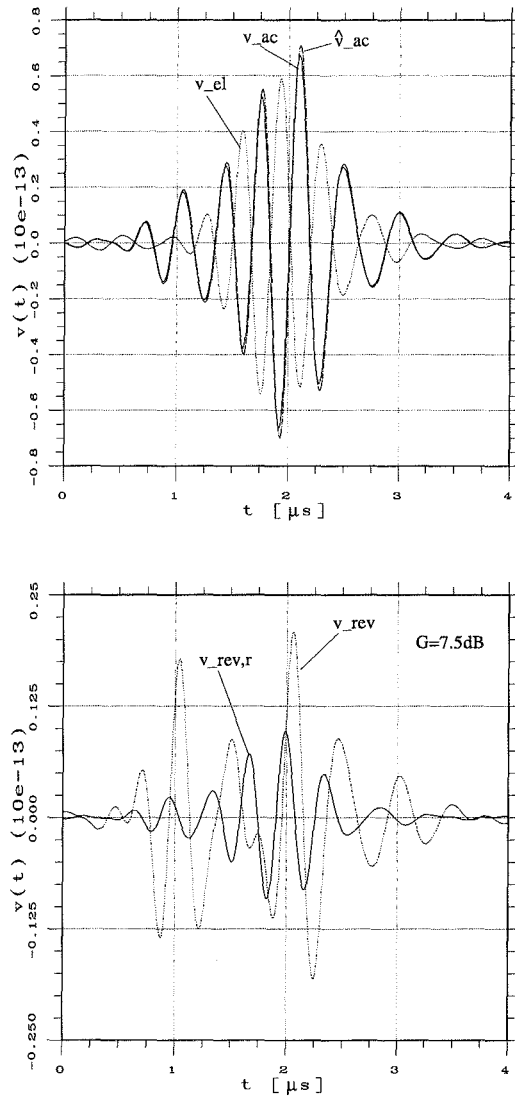


Figure 6.11: Reverberation signal components (electric/acoustic) and estimated acoustic component for the curved interface IV at 10mm and a point target at 90mm (top). Total reverberation signal and reduced reverberation signal (bottom).

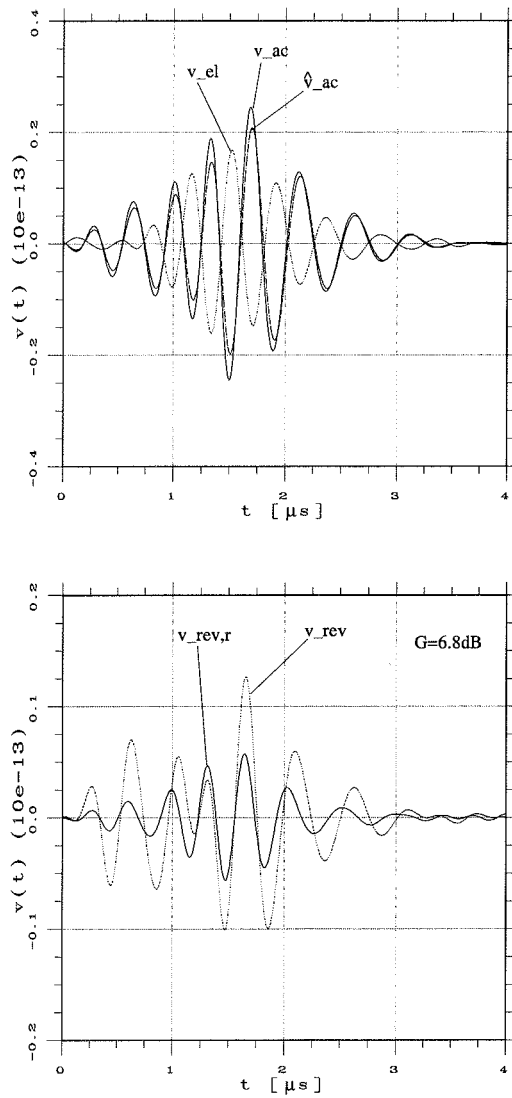


Figure 6.12: Reverberation signal components (electric/acoustic) and estimated acoustic component for the curved interface  $V$  at 10mm and a point target at 90mm (top). Total reverberation signal and reduced reverberation signal (bottom).

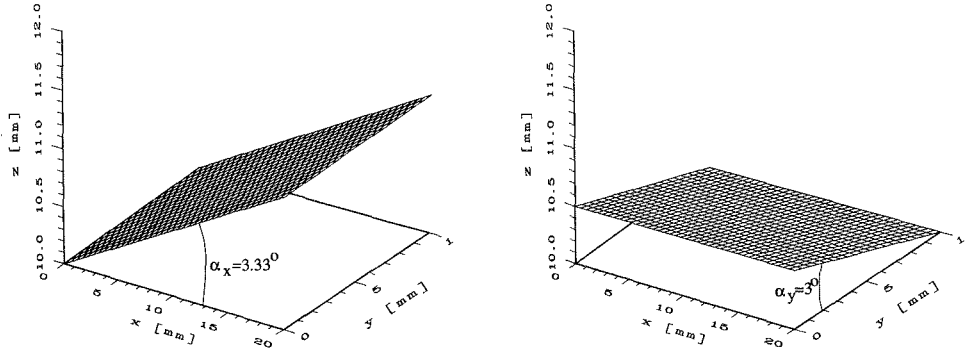


Figure 6.13: Examples of tilted plane interfaces. Tilt around the  $y$ -axis (left), around the  $x$ -axis (right).

	$\alpha_x, (\alpha_y = 0)$			$\alpha_x = 0$ $\alpha_y = 0$	$\alpha_y, (\alpha_x = 0)$			
	5	3.33	1.66		1	2	3	5
G in dB for St-1.9	14.2	10.9	11.8	10.6	7.3	3.8	2.7	1.3
G in dB for St-1.4	6.8	5.9	5.4	5.5	8.6	3.7	1.1	0.5
G in dB for St-1.6	5.4	5.2	9.9	22.6	21.2	22.1	21.4	19.5
G in dB for St-3.9	11.8	11.2	11.5	11.3	13.6	9.2	5.5	10.8
G in dB for St-3.4	9.5	13.3	11.2	11.7	15.6	2.9	0.8	0.2

Table 6.3: Reverberation reduction gain tilting a plane interface at an angle  $\alpha_x$  or  $\alpha_y$ .

gain remains approximately at the same level as for the case  $\alpha_x = 0, \alpha_y = 0$ , if we neglect the case St-1.6. The element size in the azimuth plane is small enough thus the acoustic and electric component behave equally. The error due to the element height is dominating. The result of simulation St-1.6 is, however, surprising. A decreased gain is expected but seems rather strong. We could not find a reason for this behavior and it might be due to a numerical problem.

A tilt in the elevation plane is far more critical, especially when the targets are close to the transducer. The reduction gain almost vanishes due to the effect of the different beam pattern.

### 6.3.3 Influence of interface roughness

Biological tissue is made up of cells; in the case of muscle tissue, cells have a typical diameter of  $30\mu\text{m}$ . Consequently, interfaces between different tissue types will not be smooth like mirrors but show a certain roughness which may have an influence on the obtainable reduction gain. We simulated such roughness by adding zero-mean Gaussian colored noise to the z-coordinate of the first target. See figure 6.14 for an illustration. The noise process is characterized by its variance and correlation length (the latter defined as the width of the correlation function at half its maximum) which were varied in the simulations. The target set-up was, apart from the noise modification, identical to simulation S-1.9.

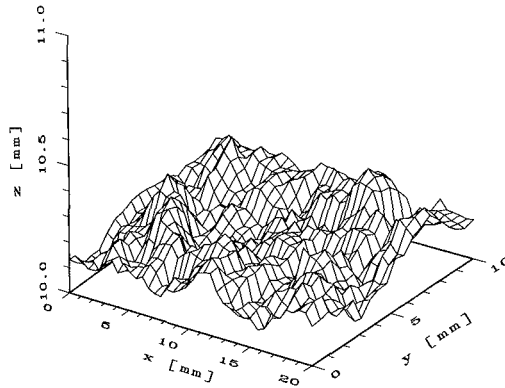


Figure 6.14: Simulation of an irregular tissue interface by adding a Gaussian non-white process to the z-coordinate.

In Table 6.4, we show the average reduction gain and its standard deviation in dB in dependence of the correlation length and the standard deviation of the z-coordinate disturbance. The statistics in the table are based on four realizations.

We see that the correlation length has no significant influence on the reduction. Increasing the roughness amplitude, however, leads to an increased variance in the reduction gain. But the average reduction stays approximately at the same level.

Recalling that the average gain for the undisturbed interfaces was  $\approx 10\text{dB}$ , we can conclude that interface roughness has no significant influence on the reduction gain.

correlation length of z-coordinate variation	z-coordinate std. characterizing interface roughness		
	10 $\mu$ m	25 $\mu$ m	50 $\mu$ m
0.5mm	10.8 $\pm$ 0.6	10.1 $\pm$ 1.4	9.7 $\pm$ 3.7
1mm	10.7 $\pm$ 0.2	9.4 $\pm$ 1.6	9.3 $\pm$ 3.6
2mm	10.5 $\pm$ 1.0	11.0 $\pm$ 1.4	8.0 $\pm$ 5.2

Table 6.4: Average reverberation reduction gain,  $G$ , in dB in dependence of the interface roughness and its standard deviation.

### 6.3.4 Element size

As argued for in section 6.2.2, the element height is the limiting factor in the presented reverberation reduction method. This was also observed in the simulations above. The best results were always obtained when we placed the second target in the elevation focus where the element height has no influence on the performance.

In order to get an estimate of how much can be gained by reducing the element height, we conducted simulations with a phased array transducer having 96 elements in azimuth and 3 or 4 elements in elevation direction (i.e. we modeled a 1.5D array). The element sizes were chosen thus the overall aperture size remained the same as above. The results are shown in Tables 6.5 and 6.6 for a height division in three elements and in Tables 6.7 and 6.8 for a height division in four elements. The target configurations corresponded to those used above.

	curved I	curved II	plane	curved III	curved IV
G in dB for S-1.9	18.0	14.5	8.6	17.3	12.5
G in dB for S-1.4	13.9	11.7	7.8	24.5	8.8
G in dB for S-1.6	22.1	16.4	26.2	19.8	19.7
G in dB for S-3.9	9.8	10.3	13.8	17.0	19.6
G in dB for S-3.4	6.8	11.3	12.6	16.9	18.3

Table 6.5: Reverberation reduction gain in dB when varying the shape of the interface in the near field as well as varying the target ranges. The transducer array has 3 equal-height elevation elements.

We see that the  $3 \times 96$  element array performs significantly better (on average  $\approx 5$ dB) than an array with just one elevation element. This is especially true if the interface in the near field is tilted in the elevation direction.

$\alpha_y$	0	1	2	3	5
G in dB for St-1.9	6.8	25.1	11.4	10.0	5.0
G in dB for St-1.4	7.8	15.7	8.6	10.7	4.0
G in dB for St-1.6	26.2	15.2	18.8	14.2	11.5
G in dB for St-3.9	13.8	13.9	12.3	10.3	8.9
G in dB for St-3.4	12.6	17.1	15.3	14.1	7.3

Table 6.6: Reverberation reduction gain in dB when varying the angle of a plane interface in the near field as well as varying the target ranges. The transducer array has 3 equal-height elevation elements.

Further, we observe that the  $4 \times 96$  element array outperforms the  $3 \times 96$  element array (on average by 3–5dB) as expected. The highest increase is again found for the tilted interface cases.

We can thus conclude that a division of the array elements in elevation direction significantly improves the reduction gain results.

	curved I	curved II	plane	curved III	curved IV
G in dB for S-1.9	17.3	11.3	18.8	22.5	15.5
G in dB for S-1.4	12.6	10.6	15.6	27.8	14.0
G in dB for S-1.6	22.1	16.4	26.2	19.8	19.7
G in dB for S-3.9	13.2	17.0	17.9	21.0	23.4
G in dB for S-3.4	11.1	22.3	16.8	21.7	23.4

Table 6.7: Reverberation reduction gain in dB when varying the shape of the interface in the near field as well as varying the target ranges. The transducer array has 4 equal-height elevation elements.

With respect to an implementation, it is important to note that the vertical division of the elements does not necessarily mean an increase in the number of channels (cables). It is only necessary to isolate the elements from each other electrically. The received signals of the three or four elevation elements may be added directly on the transducer.

A further question is whether it is optimal to divide the elements in equal size vertically or to reduce the height for the outer elements. This idea comes from the design of annular arrays where the outer elements are thinner than the inner ones. However, annular arrays are designed so that the area of the elements is the same. This would not be the case for the described phased array. It would thus be necessary to operate with different receive

$\alpha_y$	0	1	2	3	5
G in dB for St-1.9	18.8	19.5	13.9	18.3	13.8
G in dB for St-1.4	15.6	18.5	17.2	16.4	7.2
G in dB for St-1.6	26.2	21.2	25.9	21.1	19.5
G in dB for St-3.9	17.9	18.1	18.5	18.4	12.5
G in dB for St-3.4	16.8	18.7	18.8	16.0	8.7

Table 6.8: Reverberation reduction gain in dB when varying the angle of a plane interface in the near field as well as varying the target ranges. The transducer array has 4 equal-height elevation elements.

impedances since the inner impedance of a transducer element is inverse proportional to the area. This would be a slight disadvantage.

In order to find out if there is anything to gain by thinning the height of the outer elevation elements, we simulated a phased array with three elements in a vertical direction where the upper/lower elements had a height of 1.5mm and the middle one a height of 7mm. The effective height was thus again 10mm. The element heights are determined from the fact that the phase error over the elements should be equal for a spherical wave coming from a point source on the transducer axis.

The simulation results are shown in Table 6.9. We see that there is no clear improvement. For some target configurations the new array performed better than the one with equal element heights. For other configurations the opposite is true. Consequently, we can conclude that it does not seem worthwhile to adjust the element height in an 1.5D array in order to get equal phase errors over the elevation elements.

	curved I	curved II	plane	curved III	curved IV
G in dB for S-1.9	8.8	9.0	8.2	25.9	17.8
G in dB for S-1.4	7.2	5.8	8.9	23.5	15.0
G in dB for S-1.6	22.1	16.4	26.2	19.8	19.7
G in dB for S-3.9	15.6	11.2	12.4	20.0	23.4
G in dB for S-3.4	14.9	10.0	11.4	20.9	22.3

Table 6.9: Reverberation reduction gain in dB for a tissue interface varied in shape and range position. The transducer array has 3 elevation elements which differ in height.

### 6.3.5 Steering the ultrasound beam at an angle $\Theta$

Until now, we have only considered the situation where the beam is steered perpendicular to the transducer array. However, we do not expect the performance to change significantly when the beam is steered sideways because the elements in azimuth direction are so small. To confirm this, we performed simulations with the beam steered at an angle of  $\alpha = 10^\circ, 20^\circ, 30^\circ$ . The interface in the near field was of type III and placed at a range of 10mm. The second target was moved on a radius of 90mm over an arc of  $10^\circ (20^\circ, 30^\circ)$  and was thus located again on the beam axis.

The obtained reverberation reduction (see Table 6.10) out-performs the result obtained when steering the beam straight forward. From this we conclude that the scheme will work also when scanning the ultrasound beam over a sector. Additionally, it is important to note that the intensity of the reverberation signal decreases significantly, when the tissue interface remains parallel to the transducer surface.

Steering angle $\Theta$	0	10	20	30
G in dB for S-1.9	6.9	9.9	22.7	16.4
I in dB for S-1.9	0	-13	-18	-20

Table 6.10: Reduction gain, G, in dB and reverberation pulse intensity, I, in dB in dependence on the ultrasound beam direction. The second target is moved correspondingly on a radius thus it again lies on-axis.

## 6.4 Summary and remarks

In this chapter, we presented a method to reduce transducer reverberations by acquiring two RF-signals with different receive impedances. Through the following processing, it was possible to extract the electric reverberation component. An estimate of the acoustic component was then obtained by inverse filtering, to account for the different RF-pulse of the two reverberation components. The difference in the radiation pattern of the two components was, however, neglected.

The performance limit of the reduction method is essentially given by the height of the transducer elements. With a typical transducer having a center frequency of 3MHz, 96 elements of size  $180\mu\text{m} \times 10\text{mm}$  reverberation reduction varied between 0.5dB to 26dB with

an average around 10dB. The variance is due to varying ranges of the targets and changes in the shape of the tissue interface.

It should be pointed out that we never observed an increase in the reverberation noise after processing. This let us accept the fact that it is not always possible to reduce reverberations significantly, as long as the average noise reduction proves to be substantial.

It has been established that it is possible to improve the performance of the reduction scheme by some 5–8dB introducing a  $1.5D$  array with 3–4 elevation elements. In addition to increased gains in reduction, we also find less variability in the gain values in dependence on target range and target shape.

Furthermore, it turned out that interface roughness had no influence on the average reverberation reduction but increases the variance.

Steering the ultrasound beam at a specific angle, in order to perform sector scanning, had no limiting effect either on the reduction performance.

Finally, we think that the devised method has a potential for application in reverberation reduction in a scanner system. However, to prove this ultimately, in vitro and in vivo experiments must be conducted. Unfortunately, we had no appropriate experiment set-up at this time. Thus we continued to investigate yet another reduction method.

## Chapter 7

# Reverberation reduction by signal processing of first order echoes

In this chapter, we examine the question, of whether it is possible to reduce reverberations only by processing first order echo signals. Our idea is that:

*Having received the first order echoes from the scatterer distribution, we also know what is reflected at the transducer surface. It should thus be possible to extrapolate what the reverberation signal looks like.*

However, one problem may be that we are operating with a coherent imaging system. It is possible that we lose important information about the object properties through destructive interference. To answer these questions, we first formulate the processing scheme by reformulating the reverberation signal model developed in Chapter 3. The reverberation signal is decomposed into the convolution of two first order echo signals. For this, some approximations are necessary and their validity must be examined. Furthermore, this new method makes array transducers necessary and we have to examine which array type i.e. a 1D, 1.5D, 2D phased array is sufficient to obtain a good reverberation reduction. Devoid of an experiment set-up for phased array transducers, we resort again to simulations trying to answer the questions posed.

## 7.1 Development of the signal processing scheme

The reverberation signal was derived as (see equation 3.77):

$$v_{rev}(t) = u(t) * \delta'''(t) * \frac{1}{4c_a^6} \iint h_r(\vec{r}_3, t) \cdot \sigma(\vec{r}_3) * h_{rev}(\vec{r}_1, \vec{r}_3, t) * h_t(\vec{r}_1, t) \cdot \sigma(\vec{r}_1) dr_1^3 dr_3^3$$

where  $h_{rev}(\vec{r}_1, \vec{r}_3, t)$  was given by equation 3.76:

$$h_{rev}(\vec{r}_3, \vec{r}_1, t) = r_{ac}(t) * h_{rev,ac}(\vec{r}_1, \vec{r}_3, t) + r_{el}(t) * h_{rev,el}(\vec{r}_1, \vec{r}_3, t)$$

Compared to the first order signal, given by equation 3.41:

$$v_{1^{st}order}(t) = \hat{u}(t) * s(t) = u(t) * \frac{1}{2c_a^3} * \int h_r(\vec{r}_1, t) * h_t(\vec{r}_1, t) \sigma(\vec{r}_1) dr_1^3, \quad ,$$

we find only  $h_{rev}(\vec{r}_1, \vec{r}_3, t)$  as an additional component. This kernel can be decomposed into a convolution of the beam pattern of a spherical wave and a defocused first order beam pattern. We perform this step separately for the acoustic and electric components in the following.

### 7.1.1 Decomposition of the acoustic component

The acoustic component of reverberation kernel can be rewritten as:

$$\begin{aligned} h_{rev,ac}(\vec{r}_1, \vec{r}_3, t) &= \frac{\delta(t - \frac{r_3}{c})}{2\pi r_3} & (7.1) \\ &* \int_{\mathcal{A}_t} \vec{e}_{32} \vec{n}_A \frac{r_3}{|\vec{r}_2 - \vec{r}_3|} \delta\left(t - \frac{|\vec{r}_2 - \vec{r}_3| - r_3}{c}\right) * \frac{\delta\left(t - \frac{|\vec{r}_2 - \vec{r}_1|}{c}\right)}{2\pi |\vec{r}_2 - \vec{r}_1|} dr_2^2. \end{aligned}$$

As mentioned, we will resort to an array transducer to do the reverberation reduction. Therefore, we introduce array coordinates here (see figure 7.1 for the definition of the coordinate system). This leads to:

$$\begin{aligned} h_{rev,ac}(\vec{r}_1, \vec{r}_3, t) &= \frac{\delta(t - \frac{r_3}{c})}{2\pi r_3} * \sum_{n=1}^N \int_{\mathcal{A}_n} \vec{e}_{32} \vec{n}_A \frac{r_3}{|\vec{r}_{2n} + \vec{r}_{2e} - \vec{r}_3|} \cdot \delta\left(t - \frac{|\vec{r}_{2n} + \vec{r}_{2e} - \vec{r}_3| - r_3}{c}\right) \\ &\quad * \frac{\delta\left(t - \frac{|\vec{r}_{2n} + \vec{r}_{2e} - \vec{r}_1|}{c}\right)}{2\pi |\vec{r}_{2n} + \vec{r}_{2e} - \vec{r}_1|} dr_{2e}^2 \\ &= \frac{\delta(t - \frac{r_3}{c})}{2\pi r_3} * \sum_{n=1}^N a(\vec{r}_{2n}, \vec{r}_3) \delta(t - \tau(\vec{r}_{2n}, \vec{r}_3)) * \int_{\mathcal{A}_n} \vec{e}_{32} \vec{n}_A \frac{|\vec{r}_{2n} - \vec{r}_3|}{|\vec{r}_{2n} + \vec{r}_{2e} - \vec{r}_3|} \\ &\quad \cdot \delta\left(t - \frac{|\vec{r}_{2n} + \vec{r}_{2e} - \vec{r}_3|}{c} + \frac{|\vec{r}_{2n} - \vec{r}_3|}{c}\right) * \frac{\delta\left(t - \frac{|\vec{r}_{2n} + \vec{r}_{2e} - \vec{r}_1|}{c}\right)}{2\pi |\vec{r}_{2n} + \vec{r}_{2e} - \vec{r}_1|} dr_{2e}^2 \end{aligned}$$

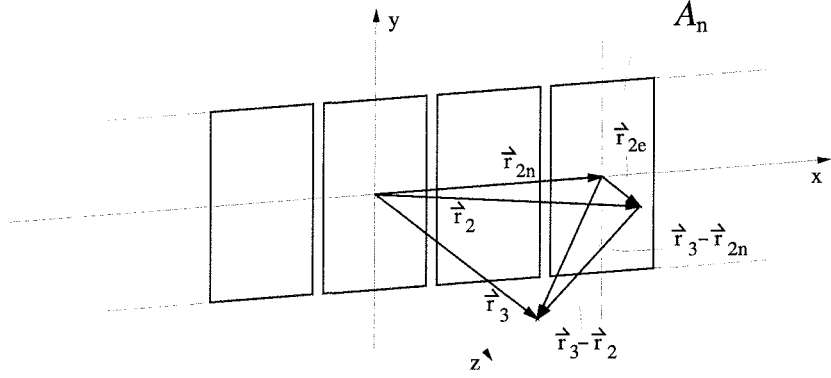


Figure 7.1: Coordinate definitions for a phased array transducer.

$$\begin{aligned}
 &= \frac{\delta(t - \frac{r_3}{c})}{2\pi r_3} * \\
 &\quad \sum_{n=1}^N a(\vec{r}_{2n}, \vec{r}_3) \cdot \delta(t - \tau_{rev,ac}(\vec{r}_{2n}, \vec{r}_3)) * h_{rev,ac,n}(\vec{r}_1, \vec{r}_3, t) \quad (7.2)
 \end{aligned}$$

where we have defined the apodization function:

$$a_{rev,ac}(\vec{r}_{2n}, \vec{r}_3) = \frac{r_3}{|\vec{r}_{2n} - \vec{r}_3|} \quad , \quad (7.3)$$

the delay function:

$$\tau_{rev,ac}(\vec{r}_{2n}, \vec{r}_3) = \frac{|\vec{r}_{2n} - \vec{r}_3| - r_3}{c} \quad , \quad (7.4)$$

and:

$$\begin{aligned}
 h_{rev,ac,n}(\vec{r}_1, \vec{r}_3, t) &= \int_{A_n} \vec{e}_{32} \vec{n}_A \frac{|\vec{r}_{2n} - \vec{r}_3|}{|\vec{r}_{2n} + \vec{r}_{2e} - \vec{r}_3|} \delta \left( t - \frac{|\vec{r}_{2n} + \vec{r}_{2e} - \vec{r}_3|}{c} + \frac{|\vec{r}_{2n} - \vec{r}_3|}{c} \right) \\
 &\quad * \frac{\delta(t - \frac{|\vec{r}_{2n} + \vec{r}_{2e} - \vec{r}_1|}{c})}{|\vec{r}_{2n} + \vec{r}_{2e} - \vec{r}_1|} dr_2^2 \quad . \quad (7.5)
 \end{aligned}$$

Inspecting the delay function, we note that it corresponds to focusing a plane transducer array at  $\vec{f} = -\vec{r}_3$  i.e. behind the transducer, which means that the beam is defocused. However, if the transducer is prefocused through surface shaping or by an acoustic lens, the focus will be at the adjunct focus of  $r_3$  given by:

$$f = \frac{F^2}{r_3} \quad (7.6)$$



$$\begin{aligned}
h_{rev,el}(\vec{r}_1, \vec{r}_3, t) &= \sum_{n=1}^N \frac{1}{A_n} h_{r,n}(\vec{r}_1, t) * h_{t,n}(\vec{r}_3, t) \\
&= \frac{\delta(t - \frac{r_3}{c})}{2\pi r_3} * \sum_{n=1}^N a(\vec{r}_{2n}, \vec{r}_3) \delta(t - \tau(\vec{r}_{2n}, \vec{r}_3)) \\
&\quad * \frac{1}{A_n} \int_{\mathcal{A}_n} \vec{e}_{32n} \vec{n}_A \frac{|\vec{r}_{2n} - \vec{r}_3|}{|\vec{r}_{2n} + \vec{r}_{2e} - \vec{r}_3|} \delta\left(t - \frac{|\vec{r}_{2n} + \vec{r}_{2e} - \vec{r}_3| - |\vec{r}_{2n} - \vec{r}_3|}{c}\right) dr_{2e}^2 \\
&\quad * \int_{\mathcal{A}_n} \frac{\delta(t - \frac{|\vec{r}_{2n} + \vec{r}_{2e} - \vec{r}_1|}{c})}{2\pi |\vec{r}_{2n} + \vec{r}_{2e} - \vec{r}_1|} dr_{2e}^2 \\
&= \frac{\delta(t - \frac{r_3}{c})}{2\pi r_3} * \sum_{n=1}^N a(\vec{r}_{2n}, \vec{r}_3) \delta(t - \tau(\vec{r}_{2n}, \vec{r}_3)) \\
&\quad * \int_{\mathcal{A}_n} \beta_{el}(\vec{r}_{2n}, \vec{r}_3, t) * \frac{\delta(t - \frac{|\vec{r}_{2n} + \vec{r}_{2e} - \vec{r}_1|}{c})}{2\pi |\vec{r}_{2n} + \vec{r}_{2e} - \vec{r}_1|} dr_{2e}^2 \quad (7.10)
\end{aligned}$$

where the apodization function,  $a(\vec{r}_{2n}, \vec{r}_3)$ , and delay function,  $\tau(\vec{r}_{2n}, \vec{r}_3)$ , are the same as for the acoustic component in the previous section and we have defined:

$$\beta_{el}(\vec{r}_{2n}, \vec{r}_3, t) = \frac{1}{A_n} \int_{\mathcal{A}_n} \vec{e}_{32n} \vec{n}_A \frac{|\vec{r}_{2n} - \vec{r}_3|}{|\vec{r}_{2n} + \vec{r}_{2e} - \vec{r}_3|} \delta\left(t - \frac{|\vec{r}_{2n} + \vec{r}_{2e} - \vec{r}_3| - |\vec{r}_{2n} - \vec{r}_3|}{c}\right) dr_{2e}^2 \quad (7.11)$$

With this we have rewritten the acoustic and electric component of the reverberation kernel in the same form differing only in the weighting functions,  $\beta(\vec{r}_{2n}, \vec{r}_3, t)$ . However, these defocused beam patterns can be realized only approximatively using phased arrays. We will study this approximation in the following section.

### 7.1.3 Realization of the defocused beam

In a practical situation, we will have a 1D phased array transducer and can steer and focus the beam flexibly in the azimuth direction. In the elevation direction the ultrasound beam is commonly focused at a fixed range with the help of an acoustic lens or by mechanical shaping and no additional (de)focusing is possible. We can thus realize only the following beam pattern as an approximation of the acoustic and electric defocused beam pattern derived above:

$$\hat{h}_{def}(\vec{r}_1, \vec{r}_3, t) = \sum_{n=1}^N a(\vec{r}_{2n}, \vec{r}_3) \delta(t - \tau(\vec{r}_{2n}, \vec{r}_3)) * \int_{\mathcal{A}_n} \frac{\delta(t - \frac{|\vec{r}_{2n} + \vec{r}_{2e} - \vec{r}_1|}{c})}{2\pi |\vec{r}_{2n} + \vec{r}_{2e} - \vec{r}_1|} dr_{2e}^2 \quad (7.12)$$

Consequently, the error of the approximation is given for an individual element as:

$$d_{ac/el} = \int_{\mathcal{A}_n} \left[ \beta_{ac/el}(\vec{r}_{2n}, \vec{r}_3, t) - \delta(t) \right] * \frac{\delta(t - \frac{|\vec{r}_{2n} + \vec{r}_{2e} - \vec{r}_1|}{c})}{2\pi|\vec{r}_{2n} + \vec{r}_{2e} - \vec{r}_1|} dr_{2e}^2 \quad (7.13)$$

where  $\beta_{ac/el}(\vec{r}_{2n}, \vec{r}_3, t)$  is either the acoustic or the electric weighting function.

This error is analyzed in Appendix D. For the moment, we neglect it (i.e.  $\beta_{ac}(\vec{r}_{2n}, \vec{r}_3, t) \approx \delta(t)$  and  $\beta_{el}(\vec{r}_{2n}, \vec{r}_3, t) \approx \delta(t)$ ) and we proceed with the reduction algorithm. We see that the acoustic and electric reverberation components now have the same beam pattern, thus we can write:

$$\begin{aligned} \hat{h}_{rev}(\vec{r}_1, \vec{r}_3, t) &= (r_{ac}(t) + r_{el}(t)) * \frac{\delta(t - \frac{r_3}{c})}{2\pi r_3} * \\ &\quad \sum_{n=1}^N a(\vec{r}_3, \vec{r}_2) \delta(t - \tau(\vec{r}_{2n}, \vec{r}_3)) * \int \frac{\delta(t - \frac{|\vec{r}_{2n} + \vec{r}_{2e} - \vec{r}_1|}{c})}{2\pi|\vec{r}_{2n} + \vec{r}_{2e} - \vec{r}_1|} dr_{2e}^2 \\ &= (r_{ac}(t) + r_{el}(t)) * h_{sph}(\vec{r}_3, t) * \hat{h}_{def}(\vec{r}_1, \vec{r}_3, t) \quad . \end{aligned} \quad (7.14)$$

The estimate of the total reverberation signal therefore becomes:

$$\begin{aligned} \hat{v}_{rev}(t) &= u(t) * \delta'''(t) * \frac{1}{4c_a^6} \iint h_r(\vec{r}_3, t) * \sigma(\vec{r}_3) * (r_{ac}(t) + r_{el}(t)) * h_{sph}(\vec{r}_3, t) \\ &\quad * \hat{h}_{def}(\vec{r}_1, \vec{r}_3, t) * \sigma(\vec{r}_1) * h_t(\vec{r}_1, t) dr_1^3 dr_3^3 \\ &= u(t) * \delta'''(t) * \frac{1}{4c_a^6} * (r_{ac}(t) + r_{el}(t)) * \\ &\quad \iint h_r(\vec{r}_3, t) * h_{sph}(\vec{r}_3, t) * \sigma(\vec{r}_3) * \hat{h}_{def}(\vec{r}_1, \vec{r}_3, t) * h_t(\vec{r}_1, t) * \sigma(\vec{r}_1) dr_1^3 dr_3^3 \quad . \end{aligned} \quad (7.15)$$

Next, we recall that  $h_r(\vec{r}_3, t)$  is the pattern of a dynamically focused beam and as this is narrow in the lateral dimensions whereas the defocused pattern  $\hat{h}_{def}(\vec{r}_1, \vec{r}_3, t)$  by its nature is wide in the lateral dimensions. An example illustrating this characteristic is given in figure 7.2. The convolution of  $h_r(\vec{r}_3, t)$  with  $\hat{h}_{def}(\vec{r}_1, \vec{r}_3, t)$  in time, means essentially a multiplication of the lateral beam profiles. Therefore, we can approximate  $\hat{h}_{def}(\vec{r}_1, \vec{r}_3, t)$  to be constant for  $|\vec{r}_3| = const$  i.e.:

$$\begin{aligned} \hat{v}_{rev}(t) &= u(t) * \delta'''(t) * \frac{1}{4c_a^6} * (r_{ac}(t) + r_{el}(t)) * \\ &\quad \iint h_r(\vec{r}_3, t) * h_{sph}(\vec{r}_3, t) * \sigma(\vec{r}_3) * \hat{h}_{def}(\vec{r}_1, r_3, t) * h_t(\vec{r}_1, t) * \sigma(\vec{r}_1) dr_1^3 dr_3^3 \quad . \end{aligned}$$

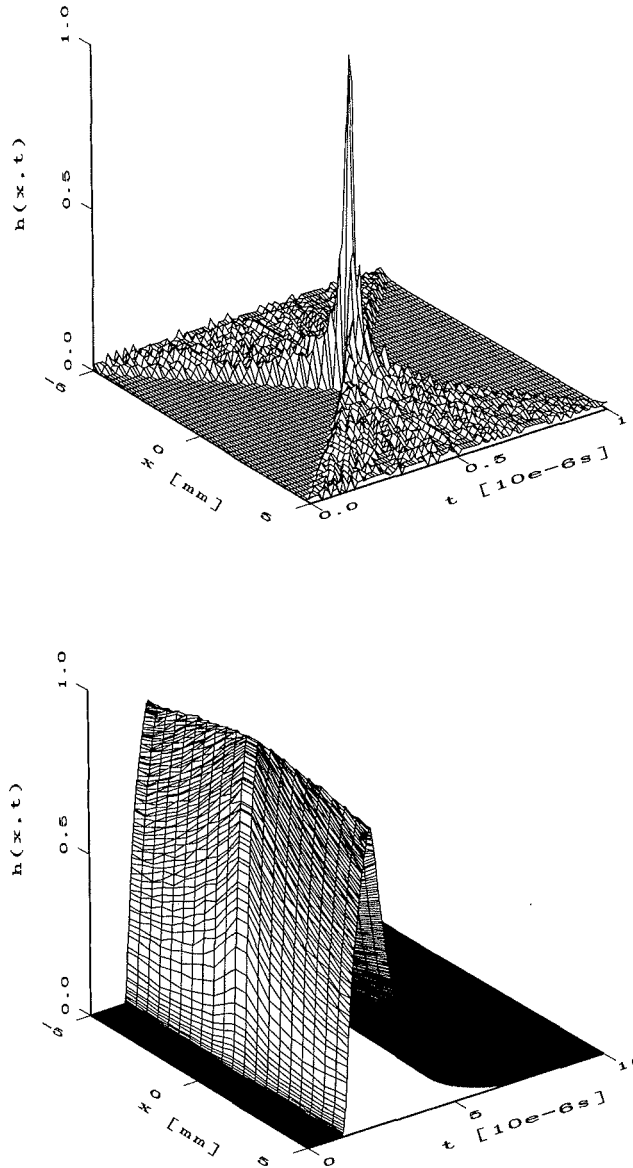


Figure 7.2: Top: Lateral beam pattern of a focused beam at the range  $r_3 = 60\text{mm}$ . The plot shows the pulse form versus the lateral offset  $x|_{r=60\text{mm}}$ . Bottom: Dependence of the pulse  $\int \hat{h}_{def}(\vec{r}_1, \vec{r}_3, t) \sigma(\vec{r}_1) d\vec{r}_1^3$  on the lateral offset  $x|_{r=60\text{mm}}$ . The target distribution  $\sigma(\vec{r}_1)$  was a plane interface at  $r_1 = 10\text{mm}$  in front of the transducer.

Furthermore, the dependence of  $\hat{h}_{def}(\vec{r}_1, r_3, t)$  on  $r_3$  is rather weak and we can define certain zones for  $r_3$ , where  $\hat{h}_{def}(\vec{r}_1, r_3, t)$  will be constant also for varying  $r_3$ . Within such a zone, we are then able to write:

$$\begin{aligned} \hat{v}_{rev}(t, r_{3zone}) = & u(t) * \delta'''(t) * \frac{1}{4c_a^6} * (r_{ac}(t) + r_{el}(t)) * \\ & \int h_r(\vec{r}_3, t) * h_{sph}(\vec{r}_3, t) \sigma(\vec{r}_3) dr_3^3 * \int \hat{h}_{def}(\vec{r}_1, r_{3zone}, t) * h_t(\vec{r}_1, t) \sigma(\vec{r}_1) dr_1^3. \end{aligned}$$

Recalling the form of a first order echo signal, we thus find the reverberation signal approximately given by the following convolution equation:

$$\hat{v}_{rev}(t, r_{3zone}) = w(t) * v_{1storder,a}(t, r_{3zone}) * v_{1storder,b}(t, r_1) \quad (7.16)$$

where  $w(t)$  is the impulse response of the inverse filter (or the corresponding Wiener filter if noise becomes a problem)<sup>1</sup>, which is necessary to transform the RF-pulse of the first order echoes into the RF-pulse of the reverberations:

$$W(f) = \frac{8\pi^3 f^3}{2c_a^3 U(f)} (R_{ac}(f) + R_{el}(f)) \quad (7.17)$$

Further, we have the defocused first order signal:

$$v_{1storder,a}(t, r_{3zone}) = u(t) * \frac{1}{2c_a^3} \int \hat{h}_{def}(\vec{r}_1, r_{3zone}, t) * h_t(\vec{r}_1, t) \sigma(\vec{r}_1) dr_1^3 \quad , \quad (7.18)$$

and the focused first order signal:

$$v_{1storder,b}(t, r_1) = u(t) * \frac{1}{2c_a^3} \int h_r(\vec{r}_3, t) * h_{sph}(\vec{r}_3, t) \sigma(\vec{r}_3) dr_3^3 \quad . \quad (7.19)$$

The dependence of  $v_{1storder,b}$  on  $r_1$  needs a comment since it seems to appear from nothing. When the reverberation echo is received, as much time has passed after sending the ultrasound pulse as if the echo had come from the range  $r_1 + r_3$ . Consequently, the receive focus is set at this point. Thus,  $r_1$  enters through the delay function  $\tau(r_1, r_3)$ , which was neglected in our notation so far for the sake of more readable expressions.

The fact that  $v_{1storder,b}$  depends on  $r_1$  has some undesired implications for our reduction scheme. It actually means that we have to acquire a focused beam signal for each  $r_1$ .

<sup>1</sup>The performance of the inverse filter is not examined here because the operation corresponds to the one presented in chapter 6.

Therefore, it is important to examine the question of whether we can neglect this dependency and use only an ordinary focused beam signal.

Similarly, we have to acquire several defocused images accounting for the different defocusing zones. If possible, it would be also here desirable to have just one zone, or to find a mapping that enables to calculate the signal for all defocusing zone from the signal from just one zone.

Assuming that the mentioned approximations are appropriate, we can formulate a simple scheme to reduce reverberations:

- Send an ultrasound pulse and receive two different first order echo signals either in sequence assuming stationary targets or in parallel by multiple line acquisition (MLA). The first of these signals is the ordinary beam signal that is used for imaging. The second signal is the defocused echo signal.
- Convolve the two acquired signals.
- Compensate for different RF-pulses by inverse filtering.
- Subtract the calculated reverberation estimate from the beam signal with ordinary focus settings.

## 7.2 Evaluation through simulations

The devised scheme and the approximations made in its derivation had to be tested by simulations. The true reverberation signal was calculated by the program described in section 3.4.4 whereas the estimate was obtained from the respective first order signals as detailed above.

The target configurations correspond to those of Chapter 6: a first reflector with an extension of  $20\text{mm} \times 10\text{mm}$  and varying shape in the  $z$ -coordinate, coded by I-V (see figures 6.6 and 6.7), was placed in the near field of the transducer array at the range  $r_1$ . The second target was a point scatterer placed on the transducer axis at range  $r_3$ . The coding identifying a simulation is the same as in Chapter 6 e.g. S-3.6 is a simulation where the first target is placed at  $r_1 = 30\text{mm}$  and the second target at  $r_3 = 60\text{mm}$  in front of the transducer. As in the previous chapter, we looked only at the reverberation signal between the two targets and the transducer, and neglected first order echoes and reverberations of

the targets against themselves. The simulation transducer was again the 96 element, 3MHz phased array with an elevation focus at 60mm. The transmit focus in the azimuth direction was set to 80mm.

### 7.2.1 Receive focus at $f_{r,b} = r_1 + r_3$

In the first batch of simulations, we examined the performance of the reduction scheme setting the receive focus of  $v_{1^{st}order,b}$  to the theoretical optimum  $f_{r,b} = r_1 + r_3$ . The spherical beam pattern was realized by setting the transmit focus at the range of the second target,  $f_{t,b} = r_3$ . The transmit focus of the beam signal,  $v_{1^{st}order,a}$ , was set to  $f_{t,a} = 80\text{mm}$  (It corresponds to the transmit focus used for the true reverberation signal). Receive defocusing was done according to the range of the second target i.e.:  $f_{r,a} = -r_3$ . The simulations tested thus the limitations of the reduction scheme performance using a 1D phased array i.e. having elements with a relative great height, while all other settings were optimal.

	curved I	curved II	plane	curved III	curved IV	acoustic delay
G in dB for S-1.4	8.6	7.6	8.6	9.1	10.8	-1
G in dB for S-2.4	7.9	9.0	7.3	11.2	11.9	-1
G in dB for S-3.4	2.6	7.5	8.1	15.6	12.5	-1
G in dB for S-1.5	18.5	18.3	12.1	7.2	6.2	-1
G in dB for S-2.5	11.6	12.1	10.8	9.2	11.4	-1
G in dB for S-3.5	7.6	17.1	22.3	10.4	8.4	-1
G in dB for S-1.6	19.6	18.1	23.3	20.2	13.5	0
G in dB for S-2.6	23.2	23.7	23.4	25.3	21.1	0
G in dB for S-3.6	24.7	26.1	26.5	28.7	28.2	0
G in dB for S-1.75	8.0	21.9	15.5	6.9	8.0	1
G in dB for S-2.75	15.1	19.9	17.2	7.5	7.0	1
G in dB for S-3.75	7.3	12.1	19.8	10.0	7.5	1
G in dB for S-1.9	13.3	12.4	8.3	7.2	6.4	1
G in dB for S-2.9	11.8	12.2	9.7	9.2	7.4	1
G in dB for S-3.9	5.2	8.1	11.7	14.4	8.8	1

Table 7.1: Simulated reverberation reduction gain for varying target ranges and varying near field target shapes with optimal focus settings. The average and standard deviation is  $\bar{G} = 13.0\text{dB}$ ,  $G_{std} = 6.5\text{dB}$ . The last column indicates the offset in samples by which the acoustic component had to be delayed to yield optimum reduction values.

The compiled reduction gains,  $G^2$ , are given in Table 7.1. It turned out that the approximation of the acoustic and electric reverberation components were quite satisfying in the pulse form and amplitude. However, we observed a delay of  $\pm 1$  sample at a sampling rate of 100MHz between the estimate and the exact signal of the acoustic component. This delay was dependent on the position of the second target and vanished when the second target was placed at the fix elevation focus of the array. Hence, we suspect that this effect is due to the relative large height of the transducer elements, though it might also result from numerical inaccuracy.

However, the delay appears to be predictable depending on the range of the second target and it will thus be possible to compensate for it. This compensation was already effectuated for the reduction gain values shown in the table. The values of the necessary delays are given in the last column of the table. Note that a delay compensation in dependence of the target shape will not be possible in a real situation, nor was it applied here.

The average reduction gain is  $\bar{G} = 13\text{dB}$  with a standard deviation of  $G_{std} = 6.5\text{dB}$ . This is better than the performance of the scheme presented in the previous chapter and promising enough to go on with further examinations.

### 7.2.2 Convenient focus settings for $v_{1^{st}order,b}$

As mentioned, it is highly desirable to dynamically focus the first order beam signal  $v_{1^{st}order,b}$  at  $f_{r,b} = r_3$  and not  $f_{r,b} = r_1 + r_3$  when receiving the echoes. Further, under transmit the ultrasound pulse can be focused only at a fixed range. This was chosen to be  $f_{t,b} = 80\text{mm}$  in the simulations. Such focus settings are likely to decrease the obtainable reduction gain and we have to study whether the decrease is tolerable.

The calculated reduction values from respective simulations are shown in Table 7.2. We observe that reduction gain values are 2–14dB lower than before (the average is  $\bar{G} = 11.2\text{dB}$  and the standard deviation  $G_{std} = 5.8\text{dB}$ ). The reason for this is that the reverberation pulse estimates no longer matched so well in amplitude. This applies especially for simulations where the second target is placed in the transition zone ( $r_3 = 40\text{mm}$ ). Here, the difference between optimal and convenient focus settings is most distinct. Further, this time it was also necessary to amend the delay between the true and the estimated electric reverberation component to get optimum reduction gains (see the last column in the table). Additionally, the delay values seemed more arbitrary.

---

<sup>2</sup>For a definition of  $G$  see equation 6.12

	curved I	curved II	plane	curved III	curved IV	ac. comp. delay	el. comp. delay
G in dB for S-1.4	3.3	3.1	2.5	3.6	3.2	-1	1
G in dB for S-2.4	6.1	5.7	4.8	3.9	5.7	-1	1
G in dB for S-3.4	4.2	10.3	11.1	7.3	4.9	-1	1
G in dB for S-1.5	5.8	6.0	7.2	9.3	9.4	-2	-1
G in dB for S-2.5	11.2	9.4	10.7	8.3	10.9	-1	0
G in dB for S-3.5	6.4	12.2	21.2	11.4	8.7	0	1
G in dB for S-1.6	18.0	16.8	18.7	17.9	11.0	-1	-1
G in dB for S-2.6	23.2	23.7	23.4	25.3	21.1	0	0
G in dB for S-3.6	16.9	17.8	16.5	14.5	16.2	1	1
G in dB for S-1.75	18.0	21.5	15.6	5.8	7.3	2	1
G in dB for S-2.75	13.6	17.6	14.4	5.6	5.8	3	2
G in dB for S-3.75	9.0	15.6	19.4	8.0	6.9	3	2
G in dB for S-1.9	13.5	12.5	8.3	6.9	6.5	2	1
G in dB for S-2.9	12.6	13.6	10.2	7.8	6.6	3	2
G in dB for S-3.9	6.0	9.3	11.9	13.1	9.7	3	2

Table 7.2: Simulated reverberation reduction gain for varying target ranges and varying near field target shapes.  $v_{1^{st}order,b}$  is focused at 80mm under transmit; ordinary dynamic focusing is applied under receive. The average and standard deviation is  $\bar{G} = 11.2\text{dB}$ ,  $G_{std} = 5.8\text{dB}$ . The last two columns indicate the offset in samples by which the acoustic and electric components had to be delayed to yield optimum reduction.

Yet, we see that as long as the second target is located in the far field, the effect of the changed focus settings is modest and we can still get some 6–15dB in reverberation noise reduction.

Thus, despite the problem with the delay between the true pulse and its estimate, we continued examining the noise reduction performance depending on a change in the focus settings of  $v_{1^{st}order,a}$ .

### 7.2.3 Defocusing settings

We investigated the question of whether it is possible to operate with just one defocusing zone. This would be simplest to implement.

An intuitive choice for the fixed 'defocus' was  $f_{r,a} = -60\text{mm}$  i.e. the negative value of the fixed focus in an elevation direction. Hence, we used  $v_{1^{st}order,a}(t, r_{zone})|_{r_{zone}=-60\text{mm}}$  for the generation of all reverberation pulse estimates. (The transmit focus was  $f_{t,a} = 80\text{mm}$ .)

The calculated reduction gain values are given in Table 7.3. The values for S-1.6, S-2.6 and S-3.6 do not change, of course, and are hence not repeated.

	curved I	curved II	plane	curved III	curved IV	ac. comp. delay	el. comp. delay
G in dB for S-1.4	1.9	3.4	5.1	3.9	-1.9	1	1
G in dB for S-2.4	4.0	3.6	5.3	3.6	5.2	4	3
G in dB for S-3.4	2.8	6.1	11.4	6.2	3.3	2	2
G in dB for S-1.5	3.3	4.2	5.5	10.8	7.7	- 1	- 1
G in dB for S-2.5	10.9	9.4	10.7	8.3	10.9	- 1	0
G in dB for S-3.5	7.2	15.6	15.8	8.6	6.8	- 1	0
G in dB for S-1.75	11.3	5.2	15.2	10.0	10.2	0	- 1
G in dB for S-2.75	12.8	7.7	12.1	8.6	10.7	1	0
G in dB for S-3.75	9.1	14.1	16.3	14.5	7.3	3	2
G in dB for S-1.9	7.0	1.4	10.6	9.7	6.5	- 1	- 1
G in dB for S-2.9	12.0	5.8	11.8	8.8	7.4	3	1
G in dB for S-3.9	6.5	6.4	14.4	14.2	11.3	3	1

Table 7.3: Simulated reverberation reduction gain for varying target ranges and varying near field target shapes. The focus of the second target is set at  $r_3$ . The average and standard deviation is  $\bar{G} = 10.4\text{dB}$ ,  $G_{std} = 5.8\text{dB}$ . The last column indicates the necessary offset in samples by which the acoustic component had to be delayed to the highest possible reduction.

We observed a modest further decrease in the reverberation attenuation ( $\approx 1\text{dB}$ ). This decrease is mainly due to lower amplitude in the estimate. In any case, with an average reduction gain of  $\bar{G} = 10.4\text{dB}$ , we can conclude that it appears to be possible to operate with just one defocusing zone.

### 7.3 Further steps

A number of questions remain to be investigated before we can design an implementable algorithm from the idea presented here. For example, we should study the performance using a 1.5D array instead of a 1D array, even though the latter one seems to produce satisfactory results.

But if the scheme is eventually going to work, we must solve the problem with the delay of the reverberation component estimates. We think, however, that before investing more time in simulations, we should verify the findings so far with experiments in order to find

out whether the encountered delay problem also exists in reality or if it is a problem due to numerical variance. Therefore, we decided to take a break in the further study of this reverberation reduction approach until we get access to an experiment system that can provide us with suitable RF-data from a phased array.

## 7.4 Conclusion

The approach presented in this chapter aimed to reduce reverberations by mere signal processing. Succeeding in this would be very interesting with respect to an implementation since no extra hardware would need to be developed.

However, simulations showed that the scheme suffered from some variance in the delay of the estimated reverberation pulses, when amending the focus settings from the theoretical optimum to those that can be realized with a conventional ultrasound system.

We conclude that further simulations are necessary to find out more about the dependencies and behavior of the reverberation pulse estimate. But first experiments should be performed to confirm the results of the simulations in this chapter.

## Chapter 8

# Conclusions

In this thesis, we addressed the problem of reverberation noise in medical ultrasound imaging and investigated different methods to reduce its effect.

### 8.1 Contributions of this thesis

The main results and contributions of the work presented in the previous chapters can be summarized as follows:

- A model and simulation program was developed describing the complete signal chain from pulse generation at the transducer to the reception of the returning first and second order echoes at the electric port of the transducer. The accuracy of the model was demonstrated in several phantom experiments.
- A model was derived describing the reflection factor of the transducer in three dimensions and pointing out the special role of the transducer electrodes. It turned out that the reflection factor decomposed into two components which are accompanied by different pulse radiation patterns.
- A method to reduce stationary reverberations in the case of cardiac imaging was developed. It consists of a highpass filter which operates on a frame to frame basis and has few coefficients in order to suit for a real-time implementation.
- A method was devised to reduce transducer reverberations by processing two RF-beam signals where the transducer was translated by  $\approx \lambda/4$ . The reduction gain was about 11dB. This method is suitable for mechanically scanned transducer probes but

a new probe design is necessary. Nevertheless it may be worth implementing for high frequency imaging in obstetrics.

- Another method to reduce transducer reverberations was developed; it discriminated reverberations by changing the receive impedance at the electrical transducer port. Simulations showed that there is a potential to reduce reverberations by 10dB–15dB if a 1.5D phased array is used.
- Finally, a reverberation reduction approach was examined that was based merely on processing received first order echo signals with special focus settings. It produced approximately 10dB in reduction gain and had the potential also to work on moving targets if MLA is applied.

We can conclude that there is a potential to successfully apply new concepts such as multiple line acquisition, direct processing of the RF-signals and the flexibility that phased arrays give to improve ultrasound image quality by reverberation reduction. However, it seems clear that advanced signal processing schemes become necessary in order attain this goal. These schemes will be demanding in high-speed signal processing hardware, which will influence the price of an ultrasound scanner. However, over a long period with steadily improving electronic devices and micro-processors at steadily decreasing prices, advanced processing schemes like the examples presented in this thesis will find their way to an implementation in a scanner.

## 8.2 Suggestions for possible future research

There are numerous possibilities for future work in the field of noise reduction in ultrasound imaging in general and reverberation reduction specifically.

First of all, one can focus on the short comings of this thesis. The highpass filter approach should be tested thoroughly with a phased array transducer and a digital scanner. Other than linear time-invariant filters may be considered, too.

In the case of the transducer displacement method, a development of a prototype would be desirable for evaluating the method with in vivo experiments.

The two reduction methods presented last need more evaluation at other transducer center frequencies. Furthermore, it is surely necessary to pursue phantom experiments to confirm the possible reduction gains calculated from the simulations.

In general, the impact of other reverberation types as such as internal reverberations and reverberations against the ribs and the skin/air interface should be the object of further studies. These types should be included into the simulation model in order to complete it. The simulation model could also be further improved by including absorption. Last but not least one should try to compare the impact of phase aberrations with the impact of reverberations quantitatively. Experiments reveal that both acoustic noise types can dominate in certain situations; however, a thorough study on this topic is still missing.

## Appendix A

# Appendix to Chapter 3

### A.1 Derivation of equation 3.39 from equation 3.36

To come from:

$$s(t) = \frac{1}{2c_a} \int h_r(\vec{r}_1, t) * \frac{\partial}{\partial t} \left( \frac{\beta(\vec{r}_1)}{c_a^2} \frac{\partial^2}{\partial t^2} + \nabla \ln(\rho(\vec{r}_1)) \nabla \right) h_t(\vec{r}_1, t) dr_1^3$$

to:

$$s(t) = \frac{1}{2c_a^3} \frac{\partial^3}{\partial t^3} \int h_r(\vec{r}_1, t) * h_t(\vec{r}_1, t) [\ln(\rho(\vec{r}_1)) + \beta(\vec{r}_1)] + \vec{h}_r(\vec{r}_1, t) * \vec{h}_t(\vec{r}_1, t) \ln(\rho(\vec{r}_1)) dr_1^3 ,$$

we start with the Green's first formula for two scalar functions  $f$  and  $g$ :

$$\int_{\partial V} \nabla f g dV = \int_V \nabla f \nabla g + g \nabla^2 f dV \quad . \quad (\text{A.1})$$

In our case, we integrate over the total space and apply the Sommerfeld radiation condition saying that the field vanishes as  $r \rightarrow \infty$ . Thus, the left side of the Green's first formula becomes zero. Hence, we have:

$$\int_V \nabla f \nabla g dV = - \int_V g \nabla^2 f dV \quad . \quad (\text{A.2})$$

We get thus:

$$s(t) = \frac{1}{2c_a} \int h_r(\vec{r}_1, t) * \frac{\partial}{\partial t} \left( \frac{\beta(\vec{r}_1)}{c_a^2} \frac{\partial^2}{\partial t^2} + \nabla \ln(\rho(\vec{r}_1)) \nabla \right) h_t(\vec{r}_1, t) dr_1^3 \quad (\text{A.3})$$

$$\begin{aligned}
&= \frac{1}{2c_a} \frac{\partial}{\partial t} \left( \int h_r(\vec{r}_1, t) * \frac{\beta(\vec{r}_1)}{c_a^2} \frac{\partial^2}{\partial t^2} h_t(\vec{r}_1, t) \, dr_1^3 \right. \\
&\quad \left. + \int \nabla \ln(\rho(\vec{r}_1)) h_r(\vec{r}_1, t) * \nabla h_t(\vec{r}_1, t) \, dr_1^3 \right) \\
&= \frac{1}{2c_a} \frac{\partial}{\partial t} \left( \frac{1}{c_a^2} \frac{\partial^2}{\partial t^2} \int h_r(\vec{r}_1, t) * h_t(\vec{r}_1, t) \beta(\vec{r}_1) \, dr_1^3 \right. \\
&\quad \left. - \int \ln(\rho(\vec{r}_1)) \nabla [h_r(\vec{r}_1, t) * \nabla h_t(\vec{r}_1, t)] \, dr_1^3 \right) \\
&= \frac{1}{2c_a} \frac{\partial}{\partial t} \left( \frac{1}{c_a^2} \frac{\partial^2}{\partial t^2} \int h_r(\vec{r}_1, t) * h_t(\vec{r}_1, t) \beta(\vec{r}_1) \, dr_1^3 \right. \\
&\quad \left. - \int \ln(\rho(\vec{r}_1)) (\nabla h_r(\vec{r}_1, t) * \nabla h_t(\vec{r}_1, t) + h_r(\vec{r}_1, t) * \nabla^2 h_t(\vec{r}_1, t)) \, dr_1^3 \right).
\end{aligned}$$

Next, we have to calculate  $\nabla h_r(\vec{r}_1, t)$ ,  $\nabla h_t(\vec{r}_1, t)$  and  $\nabla^2 h_t(\vec{r}_1, t)$ . Recalling that:

$$h_t(\vec{r}_1, t) = \int (\vec{e}_{10} \vec{n}_A) a(\vec{r}_0) \frac{\delta(t - \frac{|\vec{r}_1 - \vec{r}_0|}{c} - \tau(\vec{r}_0))}{2\pi |\vec{r}_1 - \vec{r}_0|} \, dr_0^2,$$

we find:

$$\begin{aligned}
\nabla h_t(\vec{r}_1, t) &= \int \nabla_{r_1} (\vec{e}_{10} \vec{n}_A) a(\vec{r}_0) \frac{\delta(t - \frac{|\vec{r}_1 - \vec{r}_0|}{c} - \tau(\vec{r}_0))}{2\pi |\vec{r}_1 - \vec{r}_0|} \, dr_0^2 \quad (\text{A.4}) \\
&= \int (\vec{e}_{10} \vec{n}_A) a(\vec{r}_0) \left( -\frac{\delta'(t - \frac{|\vec{r}_1 - \vec{r}_0|}{c} - \tau(\vec{r}_0))}{2\pi |\vec{r}_1 - \vec{r}_0|} \cdot \frac{\nabla_{r_1} |\vec{r}_1 - \vec{r}_0|}{c} \right. \\
&\quad \left. - \frac{\delta(t - \frac{|\vec{r}_1 - \vec{r}_0|}{c} - \tau(\vec{r}_0))}{2\pi |\vec{r}_1 - \vec{r}_0|} \cdot \frac{\nabla_{r_1} |\vec{r}_1 - \vec{r}_0|}{|\vec{r}_1 - \vec{r}_0|} \right) \, dr_0^2 \\
&= -\int (\vec{e}_{10} \vec{n}_A) a(\vec{r}_0) \left( \frac{\delta'(t - \frac{|\vec{r}_1 - \vec{r}_0|}{c} - \tau(\vec{r}_0))}{2\pi c |\vec{r}_1 - \vec{r}_0|} \vec{e}_{10} + \frac{\delta(t - \frac{|\vec{r}_1 - \vec{r}_0|}{c} - \tau(\vec{r}_0))}{2\pi |\vec{r}_1 - \vec{r}_0|^2} \vec{e}_{10} \right) \, dr_0^2.
\end{aligned}$$

The second term in the integral can again be neglected (compare equation 3.21), thus we have:

$$\nabla h_t(\vec{r}_1, t) = -\int \vec{e}_{10} (\vec{e}_{10} \vec{n}_A) a(\vec{r}_0) \frac{\delta'(t - \frac{|\vec{r}_1 - \vec{r}_0|}{c} - \tau(\vec{r}_0))}{2\pi c |\vec{r}_1 - \vec{r}_0|} \, dr_0^2 = -\vec{h}_t(\vec{r}_1, t) \quad (\text{A.5})$$

Similarly, we find:

$$\nabla h_r(\vec{r}_1, t) = -\int \vec{e}_{10} a(\vec{r}_0) \frac{\delta'(t - \frac{|\vec{r}_1 - \vec{r}_0|}{c} - \tau(\vec{r}_0))}{2\pi c |\vec{r}_1 - \vec{r}_0|} \, dr_0^2 = -\vec{h}_r(\vec{r}_1, t) \quad (\text{A.6})$$

Further, we get:

$$\begin{aligned}
\nabla^2 h_t(\vec{r}_1, t) &= -\nabla_{r_1} \int \vec{e}_{10}(\vec{e}_{10}\vec{n}_A)a(\vec{r}_0) \left( \frac{\delta'(t - \frac{|\vec{r}_1 - \vec{r}_0|}{c} - \tau(\vec{r}_0))}{2\pi c|\vec{r}_1 - \vec{r}_0|} \right. \\
&\quad \left. + \frac{\delta(t - \frac{|\vec{r}_1 - \vec{r}_0|}{c} - \tau(\vec{r}_0))}{2\pi|\vec{r}_1 - \vec{r}_0|^2} \right) dr_0^2 \\
&= -\int \nabla_{r_1} \vec{e}_{10}(\vec{e}_{10}\vec{n}_A)a(\vec{r}_0) \left( \frac{\delta'(t - \frac{|\vec{r}_1 - \vec{r}_0|}{c} - \tau(\vec{r}_0))}{2\pi c|\vec{r}_1 - \vec{r}_0|} \right. \\
&\quad \left. + \frac{\delta(t - \frac{|\vec{r}_1 - \vec{r}_0|}{c} - \tau(\vec{r}_0))}{2\pi|\vec{r}_1 - \vec{r}_0|^2} \right) dr_0^2 \\
&\quad - \int \vec{e}_{10} \nabla_{r_1}(\vec{e}_{10}\vec{n}_A) a(\vec{r}_0) \left( \frac{\delta'(t - \frac{|\vec{r}_1 - \vec{r}_0|}{c} - \tau(\vec{r}_0))}{2\pi c|\vec{r}_1 - \vec{r}_0|} \right. \\
&\quad \left. + \frac{\delta(t - \frac{|\vec{r}_1 - \vec{r}_0|}{c} - \tau(\vec{r}_0))}{2\pi|\vec{r}_1 - \vec{r}_0|^2} \right) dr_0^2 \\
&\quad + \int \vec{e}_{10} \vec{e}_{10}(\vec{e}_{10}\vec{n}_A)a(\vec{r}_0) \left( \frac{\delta''(t - \frac{|\vec{r}_1 - \vec{r}_0|}{c} - \tau(\vec{r}_0))}{2\pi c^2|\vec{r}_1 - \vec{r}_0|} + 2\frac{\delta'(t - \frac{|\vec{r}_1 - \vec{r}_0|}{c} - \tau(\vec{r}_0))}{2\pi c|\vec{r}_1 - \vec{r}_0|^2} \right. \\
&\quad \left. + \frac{\delta(t - \frac{|\vec{r}_1 - \vec{r}_0|}{c} - \tau(\vec{r}_0))}{\pi|\vec{r}_1 - \vec{r}_0|^3} \right) dr_0^2 .
\end{aligned}$$

Note that:

$$\begin{aligned}
\nabla \vec{e}_{10} &= \nabla \frac{\vec{r}_1 - \vec{r}_0}{|\vec{r}_1 - \vec{r}_0|} \\
&= -\frac{\vec{r}_1 - \vec{r}_0}{|\vec{r}_1 - \vec{r}_0|^2} \nabla |\vec{r}_1 - \vec{r}_0| + \frac{1}{|\vec{r}_1 - \vec{r}_0|} \nabla(\vec{r}_1 - \vec{r}_0) \\
&= -\frac{\vec{r}_1 - \vec{r}_0}{|\vec{r}_1 - \vec{r}_0|^2} \vec{e}_{10} + \frac{3}{|\vec{r}_1 - \vec{r}_0|} \\
&= \frac{2}{|\vec{r}_1 - \vec{r}_0|}
\end{aligned} \tag{A.7}$$

and:

$$\begin{aligned}
\nabla(\vec{e}_{10}\vec{n}_A) &= \nabla \frac{1}{|\vec{r}_1 - \vec{r}_0|} [(\vec{r}_1 - \vec{r}_0)\vec{n}_A] + \frac{1}{|\vec{r}_1 - \vec{r}_0|} \nabla [(\vec{r}_1 - \vec{r}_0)\vec{n}_A] \\
&= -\frac{\vec{e}_{10}}{|\vec{r}_1 - \vec{r}_0|^2} [(\vec{r}_1 - \vec{r}_0)\vec{n}_A] + \frac{\vec{n}_A}{|\vec{r}_1 - \vec{r}_0|} \\
&= \frac{1}{|\vec{r}_1 - \vec{r}_0|} \left( \vec{n}_A - \vec{e}_{10}(\vec{e}_{10}\vec{n}_A) \right) .
\end{aligned} \tag{A.8}$$

Having this, we again neglect all second or third order terms of  $\frac{1}{|\vec{r}_1 - \vec{r}_0|}$  and get the simple

result:

$$\nabla^2 h_t(\vec{r}_1, t) = \int (\vec{e}_{10} \vec{n}_A) a(\vec{r}_0) \frac{\delta''(t - \frac{|\vec{r}_1 - \vec{r}_0|}{c} - \tau(\vec{r}_0))}{2\pi c^2 |\vec{r}_1 - \vec{r}_0|} d\vec{r}_0^2 \quad . \quad (\text{A.9})$$

Finally, inserting the results of equations A.5, A.6 and A.9 into equation A.3, we get equation 3.39.

## A.2 Further first order off-axis plots

The plots of the lateral first order echo beam profiles for the target ranges of 40mm and 90mm are given below.

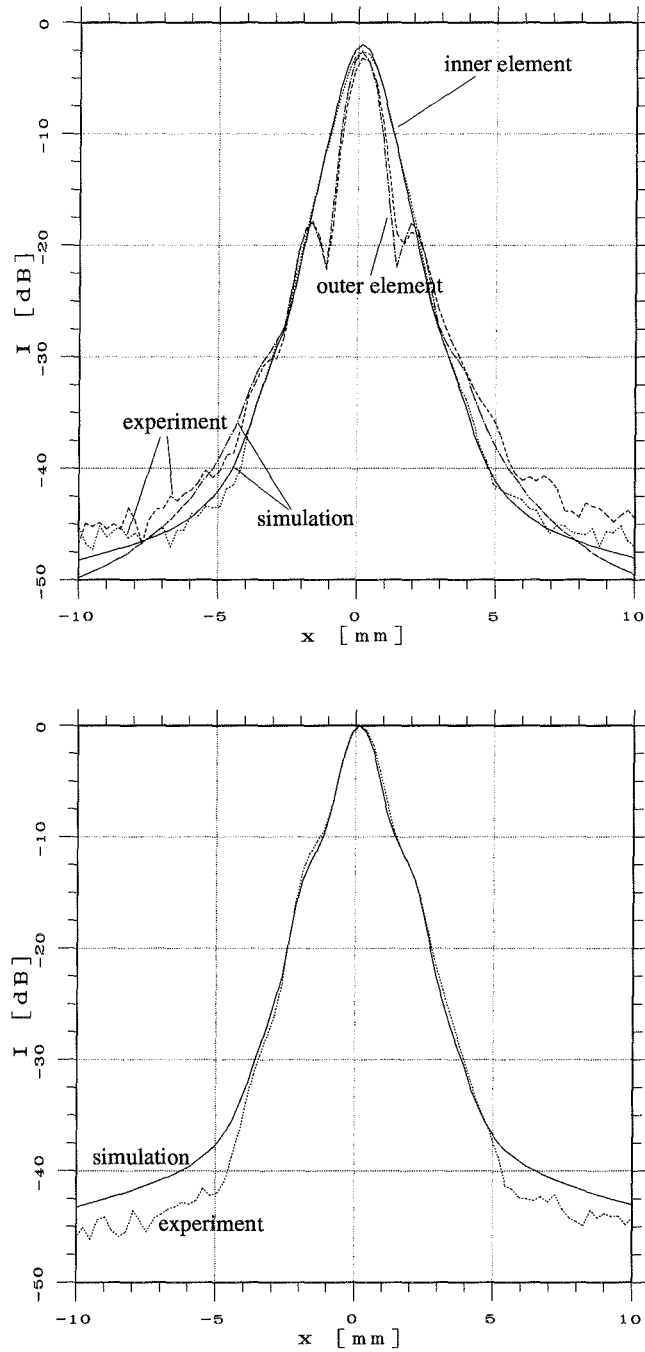


Figure A.1: Lateral beam profile (two ways) at a target range of 40mm. Individual element profiles for the inner and outer element (top) and profile for the summed signal (bottom). Comparison between experiment and simulation.

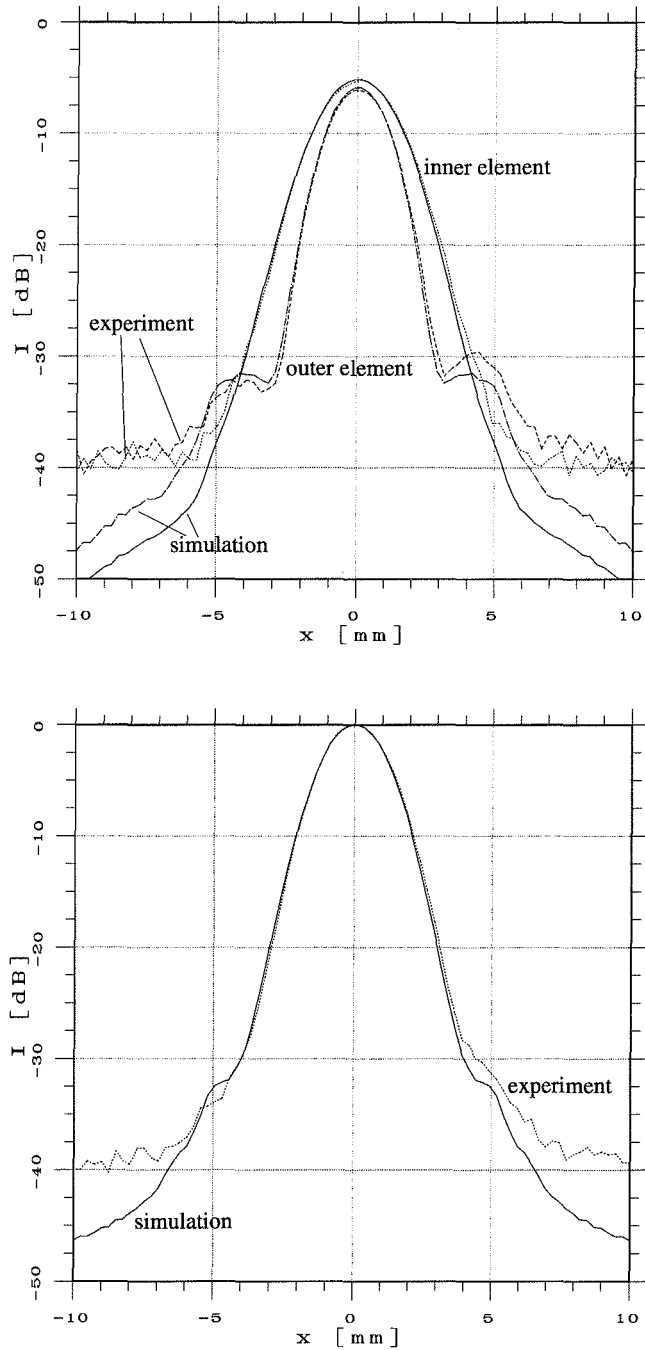


Figure A.2: Lateral beam profile (two ways) at a target range of 90mm. Individual element profiles for the inner and outer element (top) and profile for the summed signal (bottom). Comparison between experiment and simulation.

## Appendix B

# Appendix to Chapter 4

### B.1 FIR filter design

The FIR filters used in Chapter 4 were designed with the matlab<sup>TM</sup> function `firfs()`. This function calculates the coefficients of an  $N$ th order filter by minimizing the mean square error of the filter frequency spectrum in the pass and stop bands i.e.:

$$w \cdot \int_0^{f_1} |H(f)|^2 df + \int_{f_2}^{0.5} |H(f) - 1|^2 df \rightarrow \min \quad (\text{B.1})$$

where the interval between  $f_1$  and  $f_2$  is a *don't care* region and  $w$  is a weighting factor to accentuate the error of the stop band. The weighting factor was set to 10 in the case it differed from 1. This is indicated with a 'w' appended to the filter name. The filter coefficients of the second, third and fourth order FIR filters are:

FIR2	FIR2w
-0.17420073058909	-0.31087175996266
0.80568773159132	0.65297147615620
-0.17420073058909	-0.31087175996266

FIR3	FIR3w
-0.12648943433323	-0.03824087666933
-0.60475174275216	-0.57319562707949
0.60475174275216	0.57319562707949
0.12648943433323	0.03824087666933

FIR4	FIR4w
-0.13857251302781	-0.15475438629500
-0.20055496803904	-0.22535786527460
0.77517229807149	0.74703766489686
-0.20055496803904	-0.22535786527460
-0.13857251302781	-0.15475438629500

## B.2 IIR filter design

The IIR filter coefficients were calculated with the matlab™ function `butter()`. For a cut-off frequency of  $f_c = 0.1$ , we got the following first and second order filter coefficients:

IIR1	1	$z^{-1}$
numerator	0.75476272474721	-0.75476272474721
denominator	1	-0.50952544949443

IIR2	1	$z^{-1}$	$z^{-2}$
numerator	0.63894552515902	-1.27789105031804	0.63894552515902
denominator	1	-1.14298050253990	0.41280159809619

### B.3 Filtering results

The filtering result for the *combination signal* was given in Chapter 4. Here, we show the results of filtering the other typical signals.

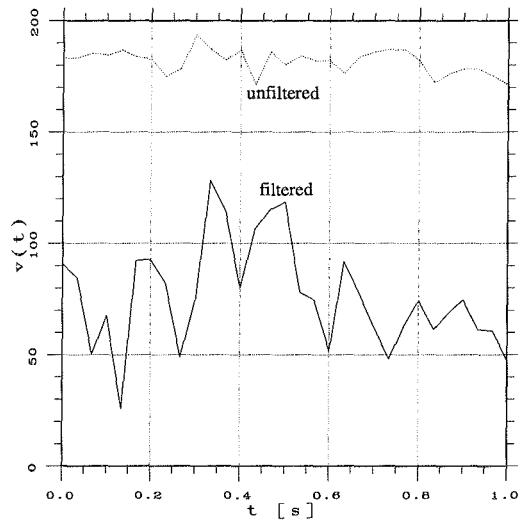


Figure B.1: Stationary reverberation signal before and after filtering with the weighted second order FIR filter. The compressed magnitude of the analytical signal is plotted versus time.

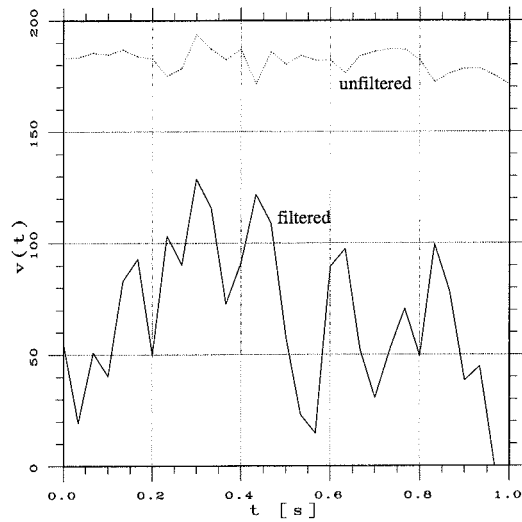


Figure B.2: Stationary reverberation signal before and after filtering with the weighted fourth order FIR filter. The compressed magnitude of the analytical signal is plotted versus time.

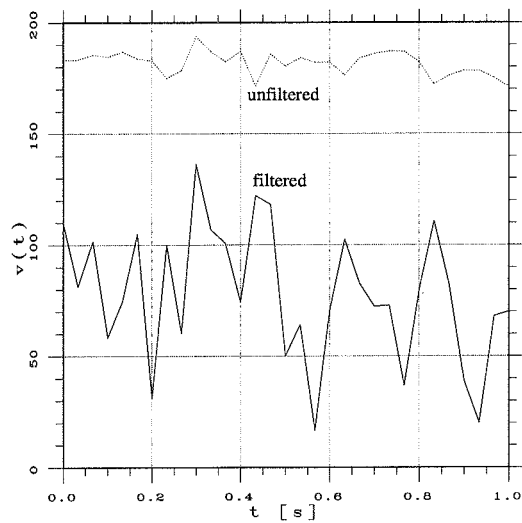


Figure B.3: Stationary reverberation signal before and after filtering with the first order IIR filter. The compressed magnitude of the analytical signal is plotted versus time.

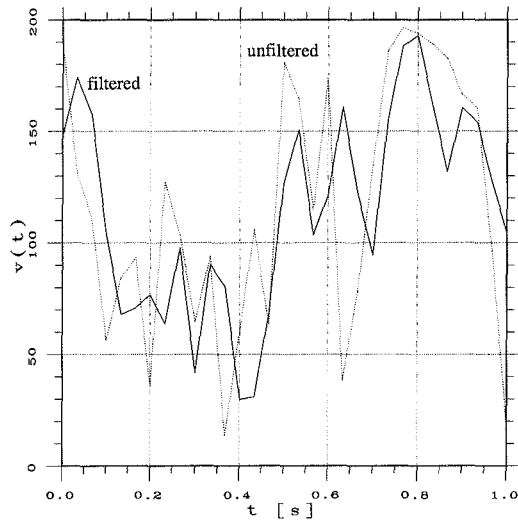


Figure B.4: Moving wall signal before and after filtering with the weighted second order FIR filter. The compressed magnitude of the analytical signal is plotted versus time.

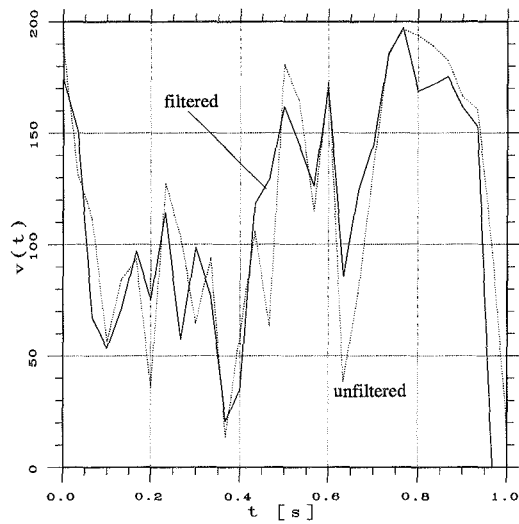


Figure B.5: Moving wall signal before and after filtering with the weighted fourth order FIR filter. The compressed magnitude of the analytical signal is plotted versus time.

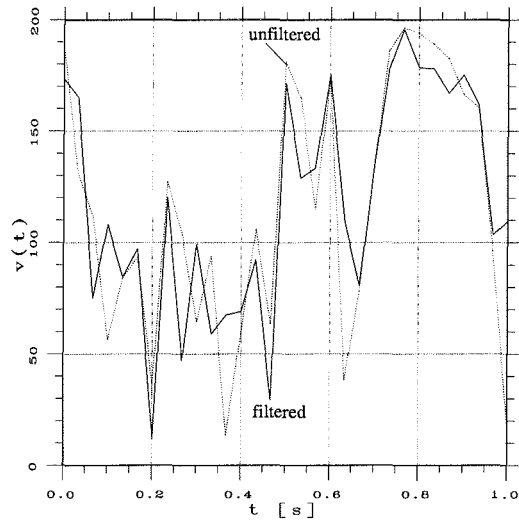


Figure B.6: Moving wall signal before and after filtering with the weighted first order IIR filter. The compressed magnitude of the analytical signal is plotted versus time.

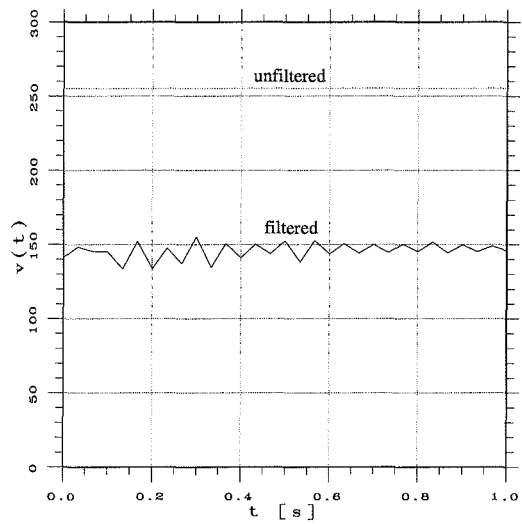


Figure B.7: Stationary fatty tissue signal before and after filtering with the weighted second order FIR filter. The compressed magnitude of the analytical signal is plotted versus time. Note the different scale at the ordinate.

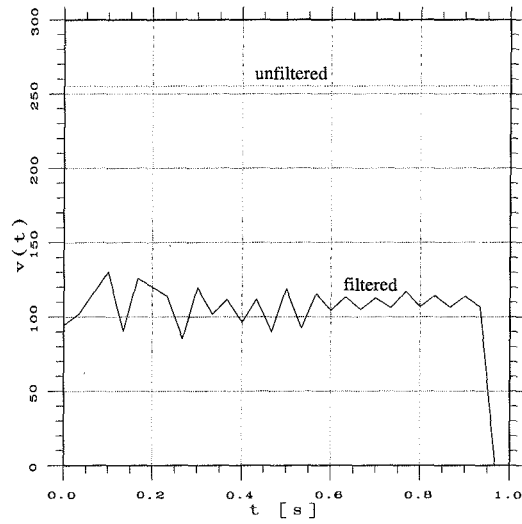


Figure B.8: Stationary fatty tissue signal before and after filtering with the weighted fourth order FIR filter. The compressed magnitude of the analytical signal is plotted versus time.

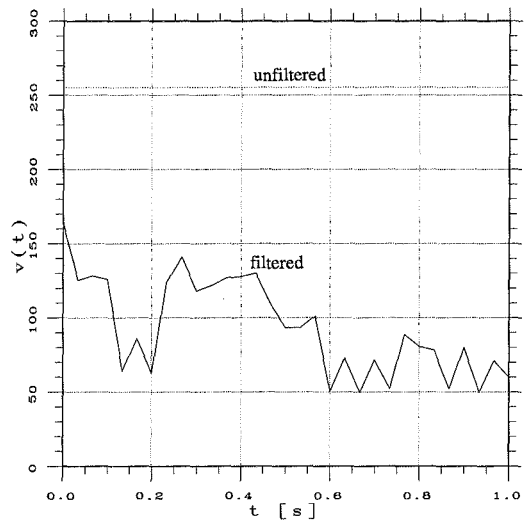


Figure B.9: Stationary fatty tissue signal before and after filtering with the weighted first order IIR filter. The compressed magnitude of the analytical signal is plotted versus time.

## Appendix C

### Appendix to Chapter 6

In Chapter 6, we used a point target as the second target in the simulations in order to reduce computational overhead, arguing that the dynamically focused receive beam is very thin in the lateral direction thus there will only be a slight difference to a real situation where the second target is an interface rather than a point. To verify the validity of this assumption, we exchanged the single point target with a target consisting of 19 points assembled in the form of a disc (see figure C.1) and performed simulations for the target configuration S-1.9. The calculated reduction gains are given in Table C.1. We see that there are variations in the reduction gain values depending on the shape of the first target. However, the average reduction gain is approximately the same independent whether the second target is a point target or a disc.

1 <sup>st</sup> target shape	curved I	curved II	plane	curved III	curved IV
G in dB for S-1.9 extended target	8.9	10.2	9.5	12.3	7.5
G in dB for S-1.9 point target	12.6	11.3	10.6	7.5	6.8

Table C.1: Comparison of reduction gains for the case when the second target has a certain extension and is approximated by a point target.

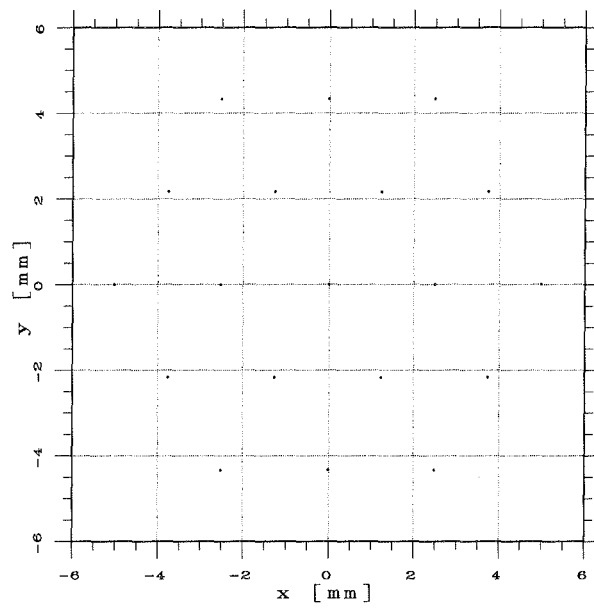


Figure C.1: Assembling of 19 point targets forming a disc of radius 5mm used as an extended second target instead of a single point target.

## Appendix D

### Appendix to Chapter 7

In this section, we examine the error:

$$d_{ac/el} = \int_{\mathcal{A}_n} \left[ \beta_{ac/el}(\vec{r}_{2n}, \vec{r}_3, t) - \delta(t) \right] * \frac{\delta\left(t - \frac{|\vec{r}_{2n} + \vec{r}_{2e} - \vec{r}_1|}{c}\right)}{2\pi|\vec{r}_{2n} + \vec{r}_{2e} - \vec{r}_1|} dr_{2e}^2 \quad ,$$

which was defined in equation 7.13 with  $\beta_{ac/el}(\vec{r}_{2n}, \vec{r}_3, t)$  found in equation 7.9 and 7.11, respectively. We see that it is proportional to the difference:

$$d_{\beta}(\vec{r}_{2n}, \vec{r}_3, t) = \left[ \beta_{ac/el}(\vec{r}_{2n}, \vec{r}_3, t) - \delta(t) \right] \quad . \quad (\text{D.1})$$

Analyzing this expression in the frequency domain, we find:

$$\begin{aligned} D_{\beta,ac} &= \mathcal{F}\{\beta_{ac}(\vec{r}_{2n}, \vec{r}_{2e}, \vec{r}_3, t) - \delta(t)\} \\ &= \vec{e}_{32n} \vec{n}_A \frac{|\vec{r}_{2n} - \vec{r}_3|}{|\vec{r}_{2n} + \vec{r}_{2e} - \vec{r}_3|} e^{-jk(|\vec{r}_{2n} + \vec{r}_{2e} - \vec{r}_3| - |\vec{r}_{2n} - \vec{r}_3|)} - 1 \end{aligned} \quad (\text{D.2})$$

and

$$\begin{aligned} D_{\beta,el} &= \mathcal{F}\{\beta_{el}(\vec{r}_{2n}, \vec{r}_3, t) - \delta(t)\} \\ &= \frac{1}{A_n} \int_{\mathcal{A}_n} \vec{e}_{32n} \vec{n}_A \frac{|\vec{r}_{2n} - \vec{r}_3|}{|\vec{r}_{2n} + \vec{r}_{2e} - \vec{r}_3|} e^{-jk(|\vec{r}_{2n} + \vec{r}_{2e} - \vec{r}_3| - |\vec{r}_{2n} - \vec{r}_3|)} dr_{2e}^2 - 1 \end{aligned} \quad (\text{D.3})$$

For sufficient large  $r_3$  and near to the beam axis, we have far field conditions. We thus can neglect the variation in the amplitude factor  $\vec{e}_{32n} \vec{n}_A \frac{|\vec{r}_{2n} - \vec{r}_3|}{|\vec{r}_{2n} + \vec{r}_{2e} - \vec{r}_3|}$  and introduce the Fraunhofer approximation in the phase term. This leads to:

$$D_{\beta,ac} \approx e^{-jk(|\vec{r}_{2n} - \vec{r}_3| + \frac{\vec{r}_{2n} - \vec{r}_3}{|\vec{r}_{2n} - \vec{r}_3|} \vec{r}_{2e} - |\vec{r}_{2n} - \vec{r}_3|)} - 1 = e^{-jk \frac{\vec{r}_{2n} - \vec{r}_3}{|\vec{r}_{2n} - \vec{r}_3|} \vec{r}_{2e}} - 1 \quad (\text{D.4})$$

and

$$\begin{aligned} D_{\beta,el} &\approx \frac{1}{A_n} \int_{\mathcal{A}_n} e^{-jk(|\vec{r}_{2n}-\vec{r}_3|+\frac{\vec{r}_{2n}-\vec{r}_3}{|\vec{r}_{2n}-\vec{r}_3|}\vec{r}_{2e}-|\vec{r}_{2n}-\vec{r}_3|)} dr_{2e}^2 - 1 \\ &= \frac{1}{A_n} \int_{\mathcal{A}_n} e^{-jk\frac{\vec{r}_{2n}-\vec{r}_3}{|\vec{r}_{2n}-\vec{r}_3|}\vec{r}_{2e}} dr_{2e}^2 - 1 \end{aligned} \quad (D.5)$$

Assuming a plane transducer element with the dimensions  $a \times b$ , we get further (see figure 7.1 for the coordinate system):

$$D_{\beta,ac} \approx e^{-jk\frac{(x_{2n}-x_3)x_{2e}}{|\vec{r}_{2n}-\vec{r}_3|}} e^{-jk\frac{(y_{2n}-y_3)y_{2e}}{|\vec{r}_{2n}-\vec{r}_3|}} - 1 \quad (D.6)$$

and

$$\begin{aligned} D_{\beta,el} &\approx \frac{1}{ab} \int_{-a/2}^{a/2} \int_{-b/2}^{b/2} e^{-jk\frac{(x_{2n}-x_3)x_{2e}}{|\vec{r}_{2n}-\vec{r}_3|}} e^{-jk\frac{(y_{2n}-y_3)y_{2e}}{|\vec{r}_{2n}-\vec{r}_3|}} dx_{2e} dy_{2e} - 1 \\ &= \frac{1}{ab} \frac{1}{-jk\frac{(x_{2n}-x_3)}{|\vec{r}_{2n}-\vec{r}_3|}} e^{-jk\frac{(x_{2n}-x_3)x_{2e}}{|\vec{r}_{2n}-\vec{r}_3|}} \Bigg|_{-a/2}^{a/2} \\ &\quad \cdot \frac{1}{-jk\frac{(y_{2n}-y_3)}{|\vec{r}_{2n}-\vec{r}_3|}} e^{-jk\frac{(y_{2n}-y_3)y_{2e}}{|\vec{r}_{2n}-\vec{r}_3|}} \Bigg|_{-b/2}^{b/2} - 1 \\ &= si\left(k\frac{(x_{2n}-x_3)a}{2|\vec{r}_{2n}-\vec{r}_3|}\right) si\left(k\frac{(y_{2n}-y_3)b}{2|\vec{r}_{2n}-\vec{r}_3|}\right) - 1 \end{aligned} \quad (D.7)$$

In order to get an idea of typical error values, we calculate  $|D_{\beta,ac}|$  and  $|D_{\beta,el}|$  for a plane array transducer element with the dimensions of  $0.18 \times 10\text{mm}^2$ . We assume a wave length of  $\lambda = 0.5\text{mm}$  and set  $\vec{r}_{2n} - \vec{r}_3 = (10\text{mm}, 1.5\text{mm}, 50\text{mm})$ . We find:

$$|D_{\beta,ac}| \leq |e^{-j\frac{2\pi}{0.5} \frac{10 \cdot 0.18}{\sqrt{10^2+1.5^2+50^2}}} - j\frac{2\pi}{0.5} \frac{1.5 \cdot 5}{\sqrt{10^2+1.5^2+50^2}} - 1| = 1.08$$

and

$$|D_{\beta,el}| = 0.143$$

Consequently, the error for the electric component seems low enough to be tolerated. The error in the acoustic component, however, can become considerably high. But, we must remember that we have calculated an upper boundary and that the error will be averaged out by a certain degree when integrating across the element surface.

Conclusively, we expect that approximating equation 7.10 by equation 7.12 will be better than approximating equation 7.8 by equation 7.12. But due to the complex form of the error expressions, we must ultimately resort to simulations in order to assess whether the approximations are acceptable.

# Bibliography

- [1] J. R. T. C. Roelandt, G. R. S. an S Iliceto, and D. T. Linker, eds., *Cardiac Ultrasound*. London: Churchill Livingstone, 1993.
- [2] I. Hardouin, E. Lieback, J. C. Marois, and R. Hetzer, "The use of echocardiographic image processing in detecting rejection after cardiac transplantation," in *Proceedings of the IEEE Ultrasonics Symposium*, 1994.
- [3] H. G. Torp, *Signal processing in real-time, two dimensional Doppler color flow mapping*. PhD thesis, Norwegian University of Science and Technology, Aug. 1990.
- [4] N. C. Nanda, *Textbook of color Doppler echocardiography*. Philadelphia: Lea & Febiger, 1989.
- [5] L. Y. L. Mo and R. S. C. Cobbold, "A unified approach to modeling the backscattered Doppler ultrasound from blood," *IEEE Trans. Biomedical Engineering*, vol. 39, pp. 450–461, 1992.
- [6] P. M. Shankar, J. M. Reid, H. Ortega, C. W. Piccoli, and B. B. Goldberg, "Use of non-Rayleigh statistics for the identification of tumors in ultrasonic B-scans of the breast," *IEEE Trans. Medical Imaging*, vol. 687, pp. 687–692, Dec. 1993.
- [7] V. Feleppa, A. Kalisz, J. B. Sokil-Melgar, F. L. Lizzi, T. Liu, A. L. Rosado, M. C. Shao, W. R. Fair, Y. Wang, M. S. Cookson, V. E. Reuter, and W. D. W. Heston, "Typing of prostate tissue by ultrasonic spectrum analysis," *IEEE Trans. Ultra., Ferro., Freq. Control*, vol. 43, pp. 609–619, July 1996.
- [8] B. K. Hoffmeister, E. D. Verdonk, S. A. Wickline, and J. G. Miller, "Effect of collagen on the anisotropy of quasi-longitudinal mode ultrasonic velocity in fibrous soft tissues:

- A comparison of fixed tendon and fixed myocardium," *Journal of the Acoustical Society of America*, vol. 4, pp. 1957–1964, Oct. 1994.
- [9] K. A. Wear, R. F. Wagner, and B. S. Garra, "A comparison of autoregressive spectral estimation algorithms and order determination methods in ultrasonic tissue characterization," *IEEE Trans. Ultra., Ferro., Freq. Control*, vol. 42, pp. 709–716, July 1995.
- [10] Å. Grønningsæter, G. Unsgård, and S. Ommedal, "Ultrasound-guided neuro surgery: A feasibility study in the 3-30 MHz frequency range," *Journal of Neurosurgery*, vol. 10, no. 2, pp. 161–168, 1996.
- [11] N. Pandian, "3D echocardiography: current status and future directions," in *Proceedings of the IEEE Ultrasonics Symposium*, Nov. 1996.
- [12] T. Lie, J. Lundbom, S. Hatlinghus, Å. Grønningsæter, S. Ommedal, P. Aadahl, O. Sæther, and H. O. Myhre, "The application of ultrasound imaging during endovascular treatment of aortic aneurysms," *European Journal of Vascular and Endovascular Surgery*, 1996.
- [13] F. Kremkau and K. Taylor, "Artifacts in ultrasound imaging," *Journal of Ultrasound in Medicine*, vol. 5, pp. 227–237, Apr. 1986.
- [14] L. Busse, D. Dietz, and W. Glenn, "A nonlinear algorithm for speckle reduction," in *Proceedings of the IEEE Ultrasonics Symposium*, 1991.
- [15] S. W. Smith and O. T. von Ramm, "The maltese cross processor: Speckle reduction for circular transducers," *Ultrasonic Imaging*, vol. 10, pp. 153–170, 1988.
- [16] C. Kotropoulos and I. Pitas, "Optimum nonlinear signal detection and estimation in the presence of speckle," *Ultrasonic Imaging*, vol. 14, pp. 249–275, 1992.
- [17] L. Ødegaard, *Phase aberration correction in medical ultrasound imaging*. PhD thesis, Norwegian University of Science and Technology, Oct. 1995.
- [18] T. Kling, K. Shung, and G. A. Thieme, "Reverberation reduction in ultrasonic B-mode images via dual frequency image subtraction," *IEEE Trans. Medical Imaging*, vol. 12, pp. 792–802, Dec. 1993.

- [19] B. A. Angelsen, *Waves, Signals and Signal Processing in Medical Ultrasonics*. 1996. To be published.
- [20] R. E. Davidsen and S. W. Smith, "Sparse geometries for two dimensional array transducers in volumetric imaging," in *Proceedings of the IEEE Ultrasonics Symposium*, pp. 1091–1094, Nov. 1993.
- [21] R. Krimholtz, D. A. Leedom, and G. L. Matthaei, "New equivalent circuits for elementary piezoelectric transducers," *Electronic Letters*, vol. 6, no. 13, pp. 398–399, 1970.
- [22] E. L. Madsen, H. J. Sathoff, and J. A. Zagzebski, "Ultrasonic shear wave properties of soft tissues and tissuelike materials," *Journal of the Acoustical Society of America*, vol. 74, pp. 1346–1355, Nov. 1983.
- [23] A. D. Pierce, *Acoustics – An introduction to its physical principles and applications*. Woodbury, New York: Acoustical Society of America, 1989.
- [24] G. R. Harris, "Review of transient field theory for a baffled planar piston," *Journal of the Acoustical Society of America*, vol. 70, pp. 10–20, 1981.
- [25] G. S. Kino, *Acoustic Waves*. New Jersey: Prentice-Hall, 1987.
- [26] J. A. Jensen, *Medical Ultrasound Imaging - An estimation based approach*. PhD thesis, Technical University of Denmark, Sept. 1988.
- [27] P. M. Morse and K. U. Ingard, *Theoretical Acoustics*. New York: McGraw-Hill Book Company, 1968.
- [28] J. A. Jensen and N. B. Svendsen, "Calculation of pressure fields from arbitrarily shaped, apodized, and excited ultrasound transducers," *IEEE Trans. Ultra., Ferro., Freq. Control*, vol. 39, pp. 262–267, Mar. 1992.
- [29] L. Ødegaard, S. Holm, F. Teigen, and T. Kleveland, "Acoustic field simulation for arbitrarily shaped transducers in a stratified medium," in *Proceedings of the IEEE International Ultrasonics Symposium*, Nov. 1994.
- [30] A. P. Berkhoff, P. M. van den Berg, and J. M. Thijssen, "Iterative calculations of reflected and transmitted acoustic waves at a rough interface," *IEEE Trans. Ultra., Ferro., Freq. Control*, vol. 42, pp. 663–671, July 1995.

- [31] T. Xue, W. Lord, and S. Udpa, "Numerical analysis of the radiated fields of circular pistons and time-delay spherically focused arrays," *IEEE Trans. Ultra., Ferro., Freq. Control*, vol. 43, no. 1, pp. 78–87, 1996.
- [32] A. Lhémery, "Impulse response method to predict echo-responses from targets of complex geometry. Part1: Theory," *Journal of the Acoustical Society of America*, vol. 90, pp. 2799–2807, Nov. 1991.
- [33] H. Oung and F. Forsberg, "Geometric and algebraic errors in calculating a transducer's spatial impulse response," *IEEE Trans. Ultra., Ferro., Freq. Control*, vol. 43, no. 2, pp. 337–340, 1996.
- [34] N. Lamberti and M. Pappalardo, "Spurious echo generation in pulse piezoelectric transducer for acoustical imaging and its reduction," *Acoustical Imaging Proceedings*, vol. 19, pp. 219–223, 1992.
- [35] D. Royer and O. Casula, "Quantitative imaging of transient acoustic fields by optical heterodyne interferometry," in *Proceedings of the IEEE Ultrasonics Symposium*, Nov. 1994.
- [36] J. Lim and A. Oppenheim, *Advanced Topics in Signal Processing*. Englewood Cliffs, New Jersey: Prentice Hall, 1988.
- [37] Å. Grønningsæter and M. Nickel, "Stationary reverberation filter, implementation on the 2df processor in system 5," tech. rep., Departement of Physiology and Biomedical Engineering, Norwegian University of Science and Technology, Trondheim, Norway, 1993.
- [38] A. K. Nandi, "On the subsample time delay estimation of narrow-band ultrasonic echoes," *IEEE Trans. Ultra., Ferro., Freq. Control*, vol. 42, no. 6, pp. 993–1001, 1995.
- [39] I. Céspedes, Y. Huang, J. Ophir, and S. Spratt, "Methods for estimation of subsample time delays of digitized echo signals," *Ultrasonic Imaging*, vol. 17, pp. 142–171, Apr. 1995.
- [40] A. H. Quazi, "An overview on the time delay estimate in active and passive systems for target localization," *IEEE Trans. Acoust., Speech, Signal Processing*, vol. 29, pp. 527–533, June 1981.

- [41] M. Nickel, H. Torp, and B. Angelsen, "Reduction of transducer reverberations by transducer movement - determination of the optimal transducer displacement," in *Proceedings of the IEEE International Ultrasonics Symposium*, Nov. 1994.
- [42] T. I. Laakso, V. Välimäki, M. Karjalainen, and U. Laine, "Splitting the unit delay," *IEEE Signal Processing Magazine*, vol. 13, no. 1, pp. 30-60, 1996.
- [43] B. Angelsen and M. Nickel, "Method and apparatus for ultrasound imaging," *US Patent*, no. US5465723, 1995.